This Ph. D. Thesis is the result of a three-year work carried out at Department of Electrical Engineering of University of Bologna. The causes of reliability reduction of motor winding insulation supplied by voltage waveforms generated by adjustable speed drives (ASD) are here thoroughly investigated. An innovative technique based on life tests, space charge and partial discharge measurements is proposed and validated experimentally aimed at understanding insulating material behaviour under such voltage waveforms. The provided experimental framework enables to compare different insulating materials candidate to be used in motor windings supplied by ASD through electrical property characterisation and electrical endurance evaluation.

Davide Fabiani, born in Forlì on 1972, received the M.Sc., with honour, and Ph.D. in Electrical Engineering in 1997 and 2002, respectively. To date he is a post-doctorate research fellow at University of Bologna. His current research interests deal with ageing and diagnostics of insulating systems and particularly with the effect of harmonic distortion on electrical equipments. He is author of more than 30 scientific papers. He is an IEEE member and co-founder of TechImp Srl, spin-off of University of Bologna.

ISBN 88-88120-31-9
9 788888 120317

€ 10,00

Accelerated degradation of AC-Motor winding insulation

Davide Fabiani

Gedit

ALMA MATER STUDIORUM
UNIVERSITÀ DEGLI STUDI DI BOLOGNA

ACCELERATED DEGRADATION OF AC-MOTOR WINDING INSULATION DUE TO VOLTAGE WAVEFORMS GENERATED BY ADJUSTABLE SPEED DRIVERS

DAVIDE FABIANI

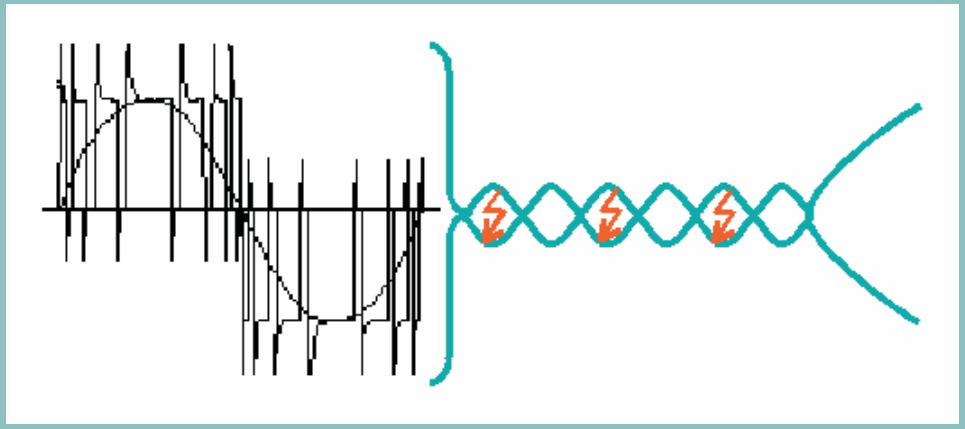

Gedit
edizioni

Accelerated Degradation of AC-Motor Winding Insulation

University of Bologna

ACCELERATED DEGRADATION OF AC-MOTOR WINDING INSULATION DUE TO VOLTAGE WAVEFORMS GENERATED BY ADJUSTABLE SPEED DRIVES

Ph.D. Thesis

by

DAVIDE FABIANI

Dr. Eng.

***Tutor**: Prof. Eng. Gian Carlo Montanari*

***Coordinator**: Prof. Eng. Francesco Negrini*

Gedit
edizioni

prima edizione: maggio 2003

Gedit Edizioni
Via Ercole Nani 2/A
40132 Bologna
tel 051 6415580, fax 051 6415315

stampa: *LegoPrint*, Lavis, Trento

ISBN: 88-88120-31-9

Preface

This Ph. D. Thesis comes after a three-year work on ac motor winding insulation. The problem of reliability reduction of winding insulation of motors supplied by voltage waveforms generated by adjustable speed drives (ASD) is here illustrated, investigating thoroughly the causes.
A new innovative technique based on life tests, space charge and partial discharge measurements is proposed and validated experimentally to understand insulating material behaviour under such voltage waveforms. This technique enables to provide an experimental procedure to compare different insulating materials candidate to be used in motor windings supplied by ASD, characterising the properties and evaluating the electrical endurance of different insulating materials.

I would like to thank Dr. F. Razza of "Ansaldo Sistemi Industriali" who provided the specimens for the experimental tests and all the people working at LIMAT (Material Engineering & High Voltage Laboratory) who contributed with their help to the development of the research object of this thesis: in particular, Dr. F. Palmieri, Dr. G. De Robertis, Dr. M. Melloni, Dr. M. Conti and Dr. F. Puletti for their precious contributions on space charge measurements, life tests and partial discharge measurements. A particular thank is addressed to Prof. Andrea Cavallini and Prof. Giovanni Mazzanti of Bologna University as well as to Prof. Alfredo Contin of Trieste University for their useful discussions and suggestions.
Finally, last but not least, I would like to thank my tutor, Prof. Gian Carlo Montanari, who stimulated me continuously during the last three years. I am indebted to him for having conveyed me his devotion to experimental science.

Bologna, 2002 Davide Fabiani

Contents

Chapter 1

Introduction

Electrical motors absorb large part of the energy that is produced world-wide. They are diffused everywhere, with different sizes (from fractions of kW to GW) and supply voltages (low, medium and high voltage, both AC and DC).

Focusing on low-voltage types, DC-motors were widely used in the past for applications that needed a continuous speed control. DC-motor speed can be controlled very simply, in fact, by varying supply voltage amplitude. On the contrary, where a fixed work speed was required, AC-induction-motors were used prevailingly. AC-induction motors are the most largely employed motors, to date, in low-voltage applications, e.g. in fans or pumps, thanks to their low cost, high efficiency and reliability with respect to DC motors, since no brushes or collector, the weakest point of DC motors, are needed. The output power control for fans and pumps, i.e. the fluid flow, has been obtained usually through closing or opening valves, which, introducing power losses, decrease the power transferred to the fluid. However, this is not the most efficient way to control the fluid flow. A more efficient way can be obtained by varying the rotations per minute of the motor: if less flow is needed the motor speed could be reduced, giving rise to a considerable energy saving.

Unfortunately, AC-motor speed may be controlled efficiently (with continuity) only through DC/AC or AC/AC converters, which allow amplitude and frequency of the supply voltage to be varied. However, the high cost prevented a large diffusion of such power converters for a long time.

For a few year, however, the cost of solid-state components is decreasing significantly, so that power converters are now more and more often employed in the so-called Adjustable Speed Drives (ASD).

It is well known that the wide use of electronic power converters (AC/DC, DC/AC, AC/AC) is one of the main causes of current and voltage distortion in the power networks [1-8]. These converters do not only generate harmonic components propagating towards the supply network side, but they provide also non-sinusoidal voltage on electric motor supply side.

An example of a simple electrical plant is sketched in Fig. 1.1: a common ASD, the polluting load, is composed by an AC/DC converter, a DC-bus with filtering functions and then a DC/AC inverter, which supplies, through the output cable, the motor to be controlled (Z_S and Z_l are the equivalent ML/LV transformer impedance and the supply line equivalent impedance, respectively; Z_C is the equivalent impedance of the cable connecting the inverter to the motor). Capacitor banks for reactive power compensation, C_K, and non-distorting loads are also connected to the network busbar.

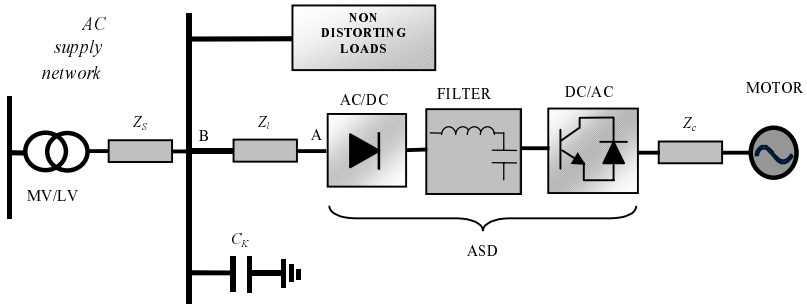

Fig. 1.1: Example of power plant including an ASD (distorting load), non distorting loads and power factor compensation bank.

As mentioned above, DC/AC converters can be considered, at the supply-bus side, as generators of harmonic currents, injected from the point A towards the network. These harmonic currents cause harmonic voltage drops along the line impedance, Z_S and Z_l, distorting bus voltage at point B, at AC/DC converter supply terminals and, thus, the supply voltage of every load connected to B. This can affect noticeably power quality of distorting and non distorting loads connected to a common bus.

The extent of distortion is related to the ratio between the distorting load power and the short-circuit power of the equivalent network seen

by B, so that even small distorting loads can affect significantly the bus voltage if the line short-circuit power is low [1, 6-8].

Supply-bus voltage distortion can be further on magnified by the parallel resonances, which are quite common in electrical power networks with capacitors for power-factor compensation. Figure 1.2 shows an example of a distorted voltage waveform recorded in an electrical network. A parallel resonance close to the 5th (i.e. 250 Hz) harmonic occurred between capacitive and inductive equivalent impedances, so that harmonic components close to the resonance frequency are significantly enhanced, becoming comparable with the fundamental one. It is noteworthy that parallel resonances can commonly occur in frequency ranges typical of those of the harmonic currents of noticeable amplitude generated by converters, i.e. between the 5th and 21st harmonic order.

Figure 1.2 shows also that voltage waveforms affected by harmonic distortion, having the same rms of a 50 Hz sinusoid, could exhibit increased peak value and/or waveform slope, depending on phase shifts of harmonic components. This can affect significantly degradation acceleration of insulation systems connected to the power network, e.g. self-healing capacitors, cables, transformers, etc [9-22].

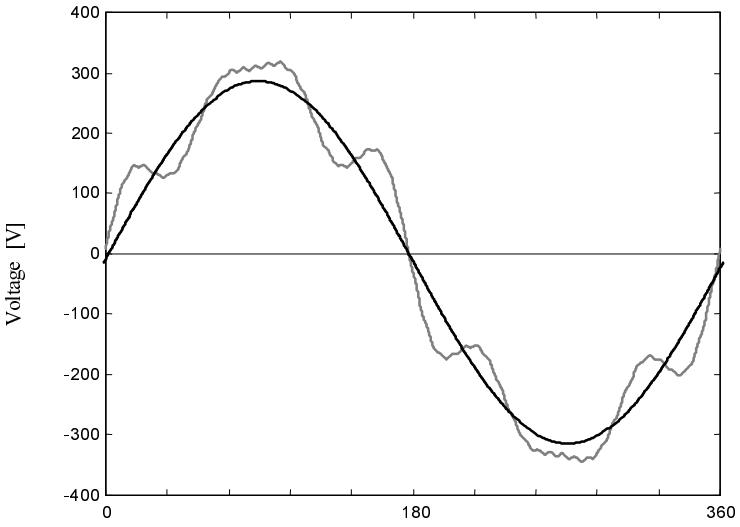

Fig. 1.2: Example of recorded waveform affected largely by 5th harmonic (in dark grey) with respect to a 50 Hz sinusoid having the same rms (in black).

In addition to the AC-supply side harmonics, the DC/AC converter does not generate a perfect AC-sinusoid, but a series of impulsive

voltage waves, whose characteristics depend on the switching technique, the motor design, the length of the cable connecting the ASD with the motor [23 - 27].

Since 1950 the British Rails observed, in some circumstances, an increase of failure rate of power cables which was explained by voltage harmonic distortion generated by power converter employed to supply train motors [28].

However, the research in this field has not been developed significantly until the '80s, because the interest on this topic was very poor due to the small number of power converters connected in electrical networks. More recently, the significant step forward made by power electronics has allowed to produce power converters at much lower costs, that has caused a large diffusion of these devices on the market.

It has been observed that the ASD employment has worsened, in several cases, the reliability of electric motors. Electrical motors fed by the first generation of power converters, i.e. realised by SCR technology, exhibit failures sometimes in the turn-to-turn insulation to be used for 50 Hz sinusoidal supply. Therefore, NEMA standard fixed some limit values for the supply voltage characteristics, e.g. 0.5 kV/μs for the rate of voltage rise, and suggested to design the turn insulation in a reinforced way, thus, withstanding to the impulsive waveforms generated by SCR matrix [29].

In the last ten years, the continuous technological development in power electronics led to the replacement of the SCRs with the new bipolar junction transistors (BJT), exploiting the pulsed width modulation (PWM) technique and producing square waves with rise front of about 2-3 kV/μs with a pulse repetition frequency up to some tens of kHz. The above mentioned NEMA standard, thus, became out of date and new limits had to be specified for inverter-fed-drives at 1.6 kV/μs [30]. These standards were further dated five or six years ago, when, thanks to the use of IGBTs, in spite of BJTs, rise fronts of some tens of kV/μs could have been reached with a pulse repetition frequency up to 20 kHz [31].

These improvements in converter technology gave some advantages in terms of switching loss reduction and improved stability of the motor torque. On the contrary, the problem of reliability of electric motors fed by power converters was reproposed dramatically. Motors, in fact, showed failures even after a few hours of service and after being repaired, they happened to fail again in a short time.

The causes of such failures may be of different types. First of all the high switching frequency of solid state components can accelerate the

intrinsic ageing due to electro-mechanical fatigue. In addition to this, the increase of dielectric and ohmic losses in the insulated wire cause localised overheating, accelerating insulation degradation. In particular, the kind of voltage waveform generated by power converters, which stresses the insulating material, plays a primary role in insulation degradation. Although modern PWM converters have reduced outstandingly the harmonic distortion at low frequencies, the high frequency harmonic content is remarkably increased, affecting voltage waveform with ringings and overvoltages having amplitude which depends on the supply-motor connection. Moreover, voltage drop is not uniform along the whole motor winding, being concentrated on the first turns of the winding.

In order to prevent the effects of steep fronted waveform on reliability of winding insulation filters can be employed, but their cost would be not acceptable, especially for low-voltage low-power motors. Wires with improved enamel insulation for motor windings are available now on the market, designed specifically for motors supplied by ASD.

Even if literature on this topics is quite wide to date, research is going on actively, since exhaustive explanations of the degradation mechanisms are still lacking and new materials are being investigated to improve insulation system endurance under distorted supply waveforms. Deeper knowledge of degradation mechanisms would allow to define test procedure able to characterise the electrical behaviour of insulating materials used in converter-fed motors.

After having analysed the voltage waveforms affecting winding insulation and discussed some results on this topic presented by some researchers, which will introduce the problem, the degradation mechanisms will be deeply investigated in this thesis through life tests, partial discharge and space charge measurements.

Chapter 2

On the voltage waveforms affecting winding insulation

2.1 Premise

Adjustable speed drives (ASD) can implement different techniques to generate the voltage waveforms requested for motor supply. Among these, Pulse Width Modulation (PWM) is one of the most commonly used switching technique. This kind of drive is becoming quite successful owing to an electronic device known as IGBT (insulated gate bipolar transistor) [31]. This device can reach very high switching frequencies with very low power losses, due to short rise times which decrease switching losses. These features, together with the control technique, can provide motor supply voltage free of low-order harmonics, responsible of torque and speed oscillations. The cancellation of low-order harmonics is achieved, however, at the cost of generation of high-order harmonics. The presence of high-frequency harmonics associated with high-frequency carrying, as well as the very steep rate of voltage rise (slew rate), causes an uneven voltage distribution along motor windings, which may considerably enhance the stress on turn-to-turn and phase-to-ground insulation, thus increasing ageing rate [21, 32-39].

The first step moving the researchers interested to a deeper investigation of the accelerated breakdown of motor insulation was, indeed, the analysis of the change of electric stress distribution from 50 (or 60) Hz supply to ASD supply provided by ASD voltage waveforms. The behaviour of phase-to-phase, phase-to-ground and turn-to-turn voltage is, thus, analysed in the following.

2.2 Phase-to-phase voltage

Figure 2.1 shows a drawing of the phase-to-phase voltage waveforms at the inverter output (A) and at the motor terminals (B).

It can be clearly observed from Fig. 2.1A that the waveform generated by a PWM AC/AC converter is not sinusoidal, but consists of a sequence of unipolar pulses of the same amplitude with very high rise fronts (up to 50 kV/μs), width modulated according to a sinusoidal law. The pulse repetition rate is linked to the high-frequency carrying (up to 50 kHz) of the AC/AC converter, while the (low) frequency pulse polarity reversal (low-frequency modulating) is related to the desired motor speed.

The amplitude of each pulse is constant and given by the level of the DC bus, i.e. the rectified input voltage. The width of the pulses is related to the desired output voltage, the wider the pulse, the larger the average output voltage.

When a motor is connected to the inverter output, overvoltages (followed by ringings) are observable at the motor clamps, as can be seen in Fig. 2.1B. These voltage spikes are caused by impedance mismatch between motor, connecting cable and inverter. In fact, when steep fronted signals are transmitted along a non-adapted line, i.e. a line not closed on its characteristic impedance, reflections may occur, giving rise to oscillations and voltage peak amplification. The theory of transmission line, in fact, says that when the surge input impedance of the motor is considerably larger than the cable characteristic impedance, the amplitude of a voltage pulse can even double. The amplitude of these peaks depends, in fact, on cable length and waveform rise time [25, 27, 40].

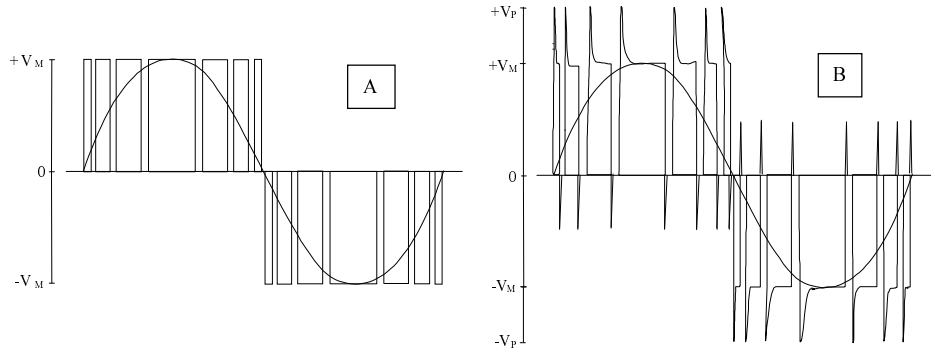

Fig. 2.1: Example of voltage waveforms (phase-to-phase) recorded in an ASD at the inverter output (A) and at the motor input (B).

Mathematical models and equivalent circuits can be used to determine the overvoltage on the leading edge of the voltage pulse at the motor terminals. The results obtained applying one of these models are plotted in the Fig. 2.2, which shows the overvoltage factor as a function of the cable length, l_c, for four different rise times, t_r, of the pulse voltage. The overvoltage factor is given by the amplitude of the voltage peak, V_P, at the motor clamps in relative value of the voltage amplitude at the inverter output, V_M. A critical cable length, l_{CC}, depending on the rise time, can be defined as the length above which 2 per unit (pu) overvoltage is reached.

As can be seen in Fig. 2.2, the shorter the rise time, the larger the amplitude of the overvoltage for a given cable length. Increasing cable length, large overvoltage factor values occur even with longer voltage rise times. For example, if t_r = 50 ns the overvoltage amplitude may became two times the maximum voltage of the DC bus for a cable length of about 5 m or more, while if t_r = 1 μs, the same overvoltage is reached if the cable is longer than 100 m.

This figure indicates that significant voltage amplification can occur very rarely with first generation inverters, e.g. those employing SCR or GTO whose rise times range from 2 to 4μs, thus long connecting cables (>100 m) are needed. This is one of the reasons why this kind of power converters did not affect largely the insulation reliability, apart from unlucky situations.

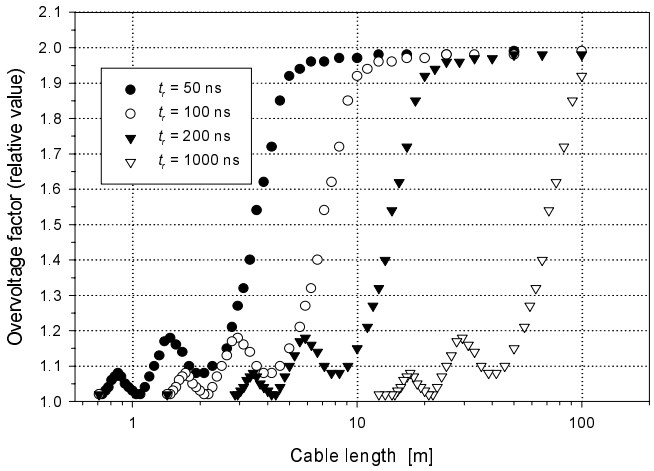

Fig. 2.2: Overvoltage at motor clamps in relative value of the voltage amplitude at the inverter output.

The second inverter generation, on the contrary, which is realised by BJT presenting rise times varying in the range 0.4 - 1μs, can show significant overvoltages with shorter cables, e.g. voltage doubling can occur with cables longer than 30m. Considering, moreover, that the rise times of the new inverter generation, IGBT based, can range from 50 to 200 ns, it can be argued that voltage doubling can be expected with very short connecting cables (5-10m). In the near future, moreover, even MOS-FET, which provide the shortest rise times (<50ns), will be used in power matrix converters. It can be understood, therefore, how technological development in electronic components could affect more and more reliability of electric motor insulation, considering that rise time decrease causes failures in motors (even with short connecting cables), which were performing well with the former-generation converters.

As a practical rule, the maximum overvoltage occurring at motor clamps can be summarised as follows [40]:

$$\begin{aligned} &\text{if } t_r/l_C > 12.5\ ns/m, \quad \text{then } V_P < 2V_M \\ &\text{if } t_r/l_C \le 12.5\ ns/m, \quad \text{then } V_P \approx 2V_M \end{aligned} \tag{2.1}$$

The ringing frequency, in MHz, depends only on cable length, according to the following relation [40]:

$$f = v/(4l_c) = 40/l_c \tag{2.2}$$

where v is the propagation speed of the waveform. As cable length increases, ringing frequency decreases.

Some authors [25, 26], moreover, suggest that for cable lengths > l_C overvoltage amplitude even > 2 times up to 3 times the inverter output voltage can occur, depending on repetition frequency of PWM pulses, as can be seen in Fig. 2.3A. This fact can be explained through the phenomenon of space charge accumulation on the connecting cable: increasing switching frequency, the zero-voltage-space between two unipolar pulses becomes so narrow that injected space charge cannot decay significantly before the arrival of the next pulse, and this may affect the magnitude of the voltage spike. For long cable length (above the critical length) overvoltages even up to 3 pu can be measured. In fact, with long cable the ringing frequency can be smaller according to eq. (2.2) so that, if another surge from the converter is triggered before the transient from the previous pulse has been extinguished, the overvoltage peak can be significantly amplified. As can be seen in the

Fig. 2.3B if the *dwell time* t_d (the time when the line-to-line voltage is zero) is shorter than 3τ (τ is the time constant related to the natural cable oscillation frequency), two consecutive transients exert mutual influence, magnifying the first peak of the ringing.

The damping effect of cable, i.e. cable resistance, influenced by skin and proximity effects, plays against peak voltage amplification, lowering voltage transient at each commutation.

The large overvoltages that can be caused by the combination of rate of voltage rise and impedance mismatches can contribute to the magnification of electrical stress affecting winding insulation. In some conditions, voltage amplitude can be so high to exceed partial discharge inception voltage (PDIV), so that insulation degradation may be largely accelerated due to partial discharge (PD) activity which would be absent under 50 Hz sinusoidal supply. However, considering the high frequency of the surges, these spikes may occur even thousands of times per second, thus contributing to degradation acceleration of insulating materials even in the absence of PD. They constitute, in fact, an additional stress accelerating intrinsic ageing, e.g. producing and/or enlarging micro-cavities in the material due to local electromechanical energy storage and electrical fatigue in the winding strand insulation, composed by a thin imide-amide enamel insulation.

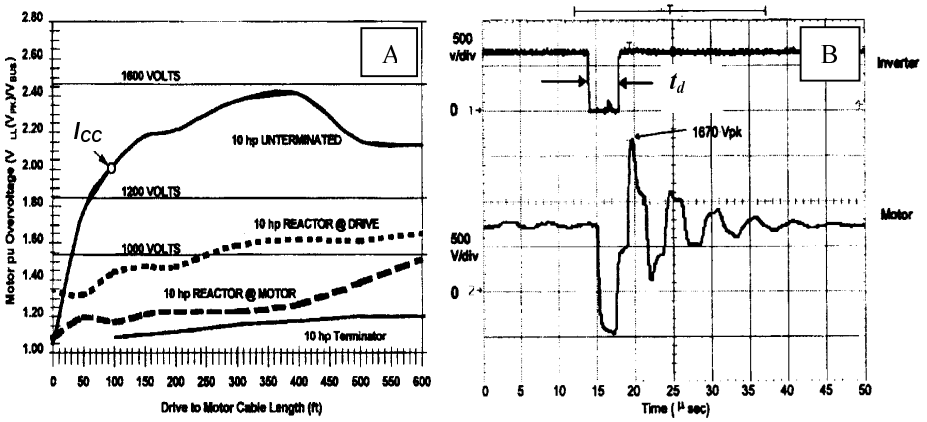

Fig. 2.3: Overvoltage at the motor input, for different motor configurations, as a function of cable length. The critical cable length l_{CC} is also indicated (A). Dwell time, t_d, affects ringing amplitude (B) more and more as pulse repetition rate increases [after 25, 26].

2.3 Phase-to-ground voltage

Ground-wall insulation is designed on the basis of service voltage and has the purpose to avoid phase-to-ground short-circuit between stator windings and motor frame, which is connected with the ground according to safety standards. The insulation, obtained through multi-layer mica-paper tapes impregnated with polyester and epoxy resin, can be affected significantly by ASD voltage waveforms.

Figure 2.4A shows the phase-to-ground voltage waveform, constituted of a sequence of high-frequency bipolar pulses width modulated as it occurs for phase-to-phase voltage [32, 33]. Even the phase-to-ground voltage is affected by spikes and ringings caused by impedance mismatches between cable and motor, as for phase-to-phase voltage. This is emphasised in Fig. 2.4B, reporting the phase-to-ground voltage in a reduced time scale. These spikes repeated at each pulse commutation, at a rate determined by the switching frequency of the electronic drive, are able to accelerate significantly the degradation of phase-to-ground insulation, especially if PDIV is exceeded.

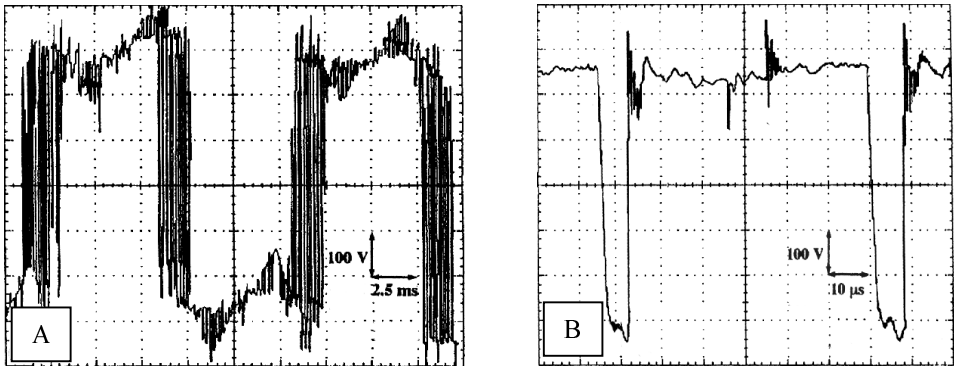

Fig. 2.4: (A) Example of turn-to-ground voltage waveform recorded in a PWM supplied motor; (B) the same waveform with a reduced time scale (after [33]).

2.4 Turn-to-turn voltage

What is really peculiar of ASD waveform effect on insulation is the amplitude and the shape of the turn-to-turn stress. The potential distribution across a winding is uniform under 50 Hz sinusoidal voltage, being the voltage drop across a turn generally ≤ 25V. On the contrary, when a steep fronted waveform is applied to a winding, the voltage distribution, turn by turn, can be extremely uneven. In this case, in fact,

most of the voltage drops along the first turns of a winding, since motor windings can be represented roughly as a derivative circuit at the high switching frequencies of the converter supply voltage (the parasitic capacitances between each turn and ground become, indeed, prevailing). Travelling across the winding, the voltage shape changes turn by turn, decreasing its rise front and smoothing the overvoltages, i.e. losing part of its high-frequency harmonic content which is stopped by the motor inductance and drained to ground by parasitic capacitances.

The difference between the turn-to-ground voltage of two adjacent turns belonging to a coil of the winding is, indeed, the electrical stress affecting the interturn insulation. Referring to Fig. 2.5, V_1 is the phase-to-ground voltage waveform of the first turn of the input coil, while V_2 is that relevant to an adjacent turn. It can be seen that the turn-to-turn voltage stress, given by V_1-V_2, is a bipolar pulse-like waveform [32, 33], which increases its amplitude with the voltage slew rate, i.e. decreasing the rise time and/or increasing the surge peak of the voltage waveform. The peak amplitude may reach, in the worst cases, about 100% of the total voltage amplitude, including also the commutation overvoltages due to the cable-motor impedance mismatch. This can happen because motor windings are composed by several coils connected in series, whose turns are often random wound, especially in low power low voltage motors, so that the first turn of the coil can lie adjacent to the last. This may explain why most of insulation failures occurs in the first turns of motor windings: partial discharge activity, in fact, can be triggered especially in the first coils, while partial discharges are normally absent at 50 Hz, because a small interturn stress is present (however, for the reasons explained above, accelerated ageing and failure can occur also in the absence of PD).

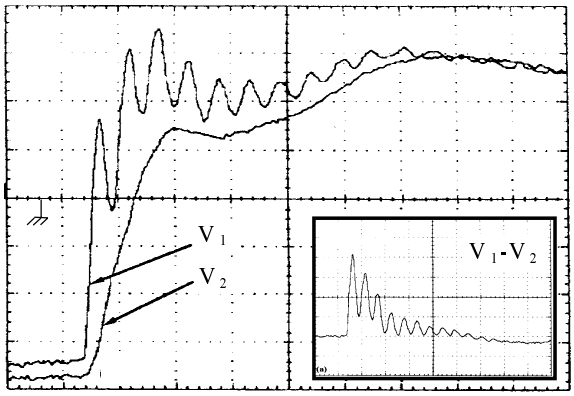

Fig. 2.5 : Phase-to-ground voltage of two adjacent turns (V_1) and (V_2) and turn-to-turn voltage V_1-V_2, (after [33]).

2.5 How converter design affects interturn stress

An high frequency model of the inverter-cable-motor system can be useful for the purpose of analyzing the kind of voltage waveform, generated by power converter, affecting winding insulation. While inverter-motor connecting cable can be simply schematised, at high frequency, by a L-C-R circuit, the electric motor can be described only very roughly by L-C bipole where C is the capacitance to ground relevant to stator turns and L is the self and mutual inductance of turns. Accurate high-frequency motor models require complex equivalent circuits, due to the complex winding configuration [41]. Turns can be, in fact, interconnected and influence each other, causing the voltage waveform to have shape along the winding not easily reproducible.

However, if the purpose is to investigate the effect of different commutation rules on voltage shape which affect turn insulation, very simple models, obtained using MATLAB - SIMULINK environment, can be used. Even if this quite rough model is not able to replicate the exact voltage waveform in each turn, it can provide, in fact, qualitative-quantitative information about the amplitude of the interturn stress under waveforms generated by different kind of converters.

Figure 2.6 shows one of the models used to simulate the effect of inverter-cable-motor impedance mismatch and the filtering effect of the first winding turns under supply voltage waveform coming from a PWM inverter. The two transfer functions provide roughly the system behaviour at the motor input (TF_1) and after the first turns (TF_2) and are built up empirically using second order models. The difference V_1-V_2 provides the interturn stress. The results reported in Figs. 2.7 and 2.8 were obtained from this model.

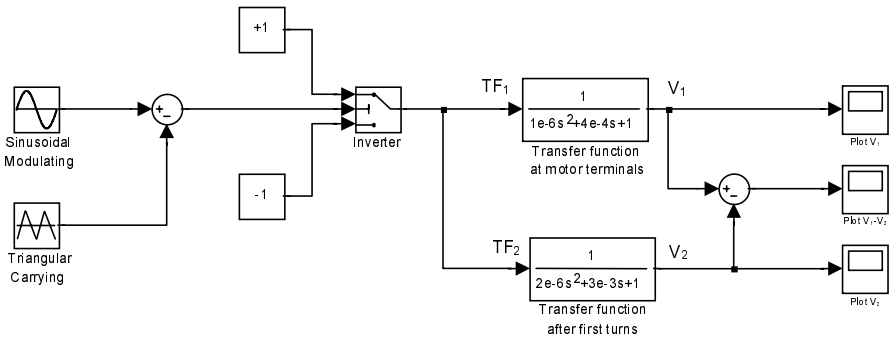

Fig. 2.6: SIMULINK model of inverter-cable-motor system under PWM supply.

Figure 2.7 shows the results of the simulation through the SIMULINK model reported in Fig. 2.6 for a PWM waveform applied to the cable-motor system in the worst condition, i.e. cable length ≥ l_{CC}, short rise times (<100 ns), random wound winding with first turn adjacent to the last. The black line is the phase-to-ground voltage at the motor terminals and applied to the first turn, V_1, the dashed one is the phase-to-ground voltage in the last turn of the coil, V_2, while the pulse-like interturn stress (V_1-V_2) is given by the grey line. Comparing these waveforms with those measured of Fig. 2.5, one can see that the information provided by the model are quite close to experimental results (at least qualitatively).

The voltage waveforms reported in Figs. 2.1-2.5 are relevant to a 2-level PWM power converter, which is a low-cost design and simple solution to control frequency and rms of the ac-output voltage. More sophisticated multi-level power converters (e.g., 3-levels, 5-levels, etc.) are sometimes employed in application which need lower high-frequency harmonic content of the output waveform (generally, at high voltage). These power converters are able to generate multi-step pulsed waveform, sometimes also width-modulated, which can approximate better a sinusoid than the traditional 2-level waveform.

Figures 2.8A-2.10A show phase-to-ground voltage waveforms at motor terminals provided by a 2-level PWM as well as 3-level and 5-level power converters, respectively. Figures 2.8B-2.10B report the interturn stress simulated by the above cable-motor SIMULINK model.

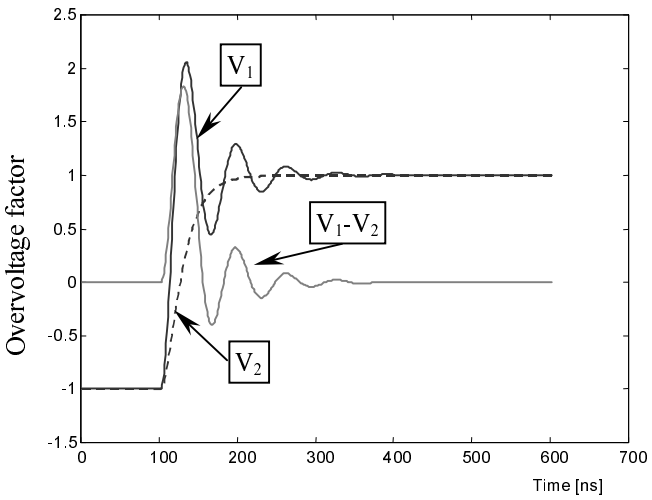

Fig. 2.7: Example of phase-to-ground voltage waveforms (V_1, V_2) relevant to adjacent turn and interturn stress (V_1-V_2) obtained by a mathematical model in SIMULINK environment.

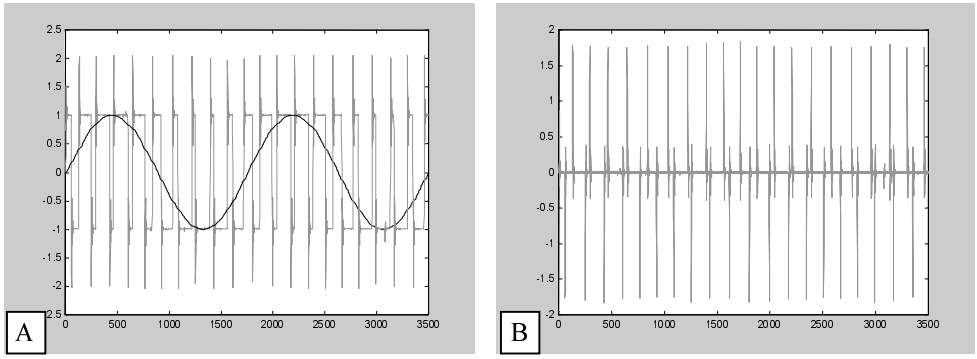

Fig. 2.8: (A) 2-level-PWM-converter phase to ground voltage (in dark grey) and the fundamental modulating (in black). (B) Interturn stress in pu

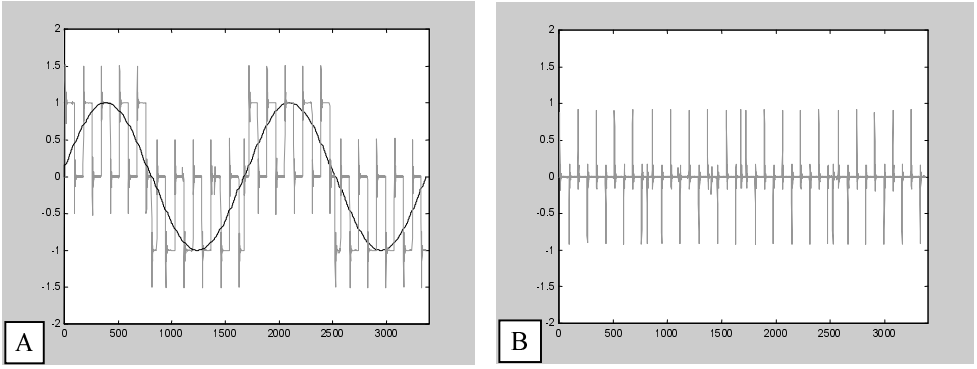

Fig. 2.9: (A) 3-level-converter phase to ground voltage (in dark grey) and the fundamental modulating (in black).
(B) Interturn stress in pu

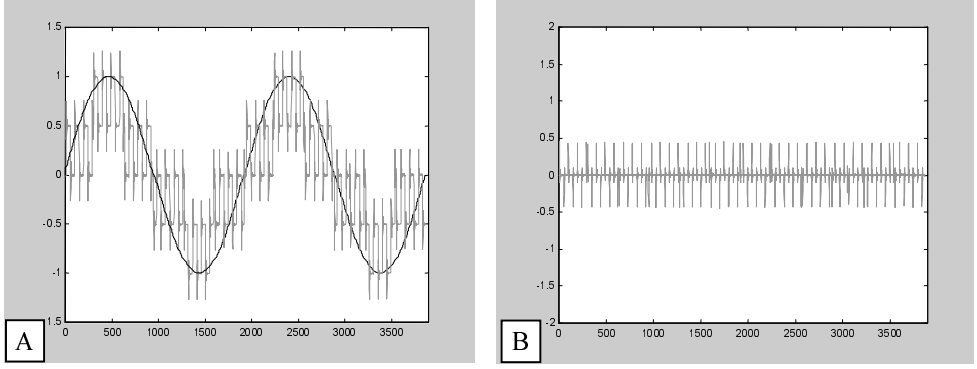

Fig. 2.10: (A) 5-level-converter phase to ground voltage (in dark grey) and the fundamental modulating (in black).
(B) Interturn stress in pu

It is confirmed again from Fig. 2.8B that the 2-level PWM power converter provides an amplitude of the maximum interturn stress (i.e. that relevant to the first turns) in the worst case of almost 2 times the amplitude of the converter output voltage (or 2 pu). If the power converter is a 3-level type (Fig. 2.9B), on the contrary, the interturn stress amplitude is almost halved (max 0.9 pu) and it becomes even lower for a 5-level converter (Fig. 2.10B), i.e. about 0.45 pu max. We can argue that increasing the number of voltage levels, which means complicating the power converter design, the interturn stress would become less and less significant, because the relative amplitude of each voltage pulse decreases. Incrementing indefinitely the number of levels, hence, the waveform generated would approximate perfectly a sinusoidal waveform, exhibiting a negligible voltage drop per turn.

Chapter 3

On the factors which affect motors fed by ASD: literature survey

3.1 Premise

As it has been mentioned in the first chapter, the literature on the effect of ASD on ageing acceleration of electrical machines is quite wide, but the results showed by different authors are often contrasting. In this chapter a brief summary of the state of the art on topics related to insulation reliability under distorted voltage, which will be developed in the following of this thesis, is provided.

Some factors, mainly relevant to the voltage waveform, have been singled out to be responsible for the degradation of insulation systems used in ASD. Divljakovic et al. [42] considered pulse amplitude, pulse repetition rate, duty cycle (i.e. pulse width) and temperature, among which the most significant factor affecting insulation reliability was identified to be pulse amplitude, while duty cycle did not show noticeable effect.

Other authors focused on the shape (unipolar or bipolar) and rise time (or rise front) of the voltage waveform [43-49]. However, beside these factors, partial discharge (PD) inception was considered generally the main degrading factor accelerating insulation degradation[18, 21, 31, 34-40, 43-59].

3.2 Effect of voltage amplitude and PD erosion

Among the authors who investigated the effect of ASD voltage waveform on winding insulation degradation, Kaufhold analysed quite deeply the relation between voltage amplitude, partial discharge probability and breakdown time. He observed, in fact, that the probability that a PD is triggered at each voltage pulse depends on how much the pulse height exceeds the inception voltage, and this affects failure time [39, 43, 45].

Figure 3.1 shows the results of life tests performed applying unipolar and bipolar voltage pulses with variable amplitude (while the other parameters are fixed: rise time = 100 ns, pulse width = 5 μs, repetition rate = 5 kHz). Failure times t_{b63}, or number of pulses to failure, n_{b63}, at a given failure probability (e.g., 63.2%), obtained applying the Weibull probability distribution, are plotted in the figure as a function of peak voltage amplitude. On the right side, PD probability is reported, expressed by the coefficient p_{PD}, which is given by the ratio of the number of voltage pulses, causing PD to the total amount of applied pulses. Three different voltage ranges can be recognised in Fig. 3.1, each one characterised by a different probability of PD occurrence. At the highest voltages (voltage range 1) each pulse is able to trigger at least one PD and the life behaviour is given by an Inverse Power Law (IPM) according to the following equation [43, 45]:

$$U_{b1} = k_b n_{b1}^{-1/m} \tag{3.1}$$

where U_{b1} is the amplitude of the pulse in range 1; n_{b1} is the number of pulses till breakdown; $-1/m$ is the slope of the life line of the IPM model; k_b, a model constant, depends on the type of applied pulses and is equal to 18 kV and 32 kV for the bipolar and unipolar pulses, respectively.

The coefficient m, also known as the voltage endurance coefficient, can constitute the measure of the capability of an insulating material to withstand electrical stress and will be explained in the next chapter.

In the second interval (voltage range 2) the number of pulses needed to reach breakdown is larger than that obtained from eq. (3.1). This is due to lower probability of PD inception in this voltage range, which increases the number of pulses needed to bring insulation to breakdown. This latter can be calculated by the following equation:

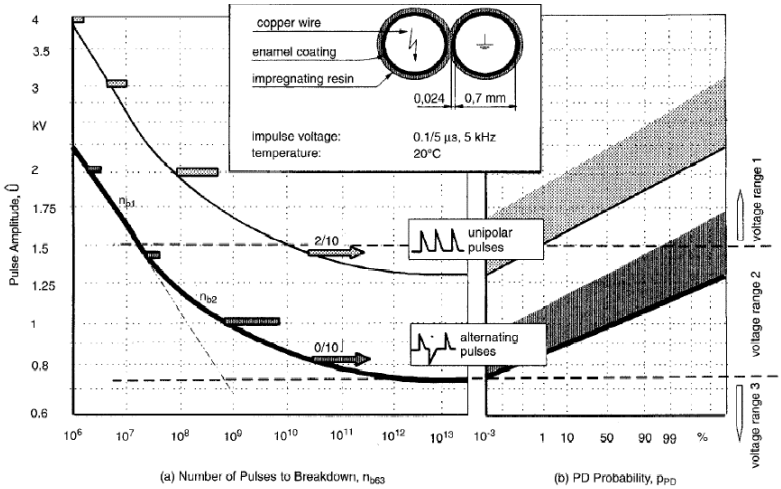

Fig. 3.1: Life behaviour of twisted enamelled wires subjected to unipolar and bipolar pulses as a function of pulse amplitude. On the right side of the plot the PD probability for each voltage level is shown (After [45]).

$$n_b = \frac{n_{b1}(U)}{p_{PD}(U)} \tag{3.2}$$

where n_b is the number of pulses occurring to breakdown, $p_{PD}(U)$ is the probability of PD inception at the voltage U, $n_{b1}(U)$ is the number of pulses needed for breakdown in voltage range 1.

It can be observed from eq. (3.2) that if PD inception probability shows a decrease of 10%, the number of the pulses to failure is 10 times larger than that derived from equation (3.1). Let us note that even in this voltage range a degradation process occurs, but the reduced number of PD provides slower ageing.

In the third voltage range, finally, it is not possible to observe any ageing phenomenon, because the probability of PD inception is so small that PD cannot affect the insulation degradation. Actually, according to what will be discussed in the next chapters, we observed insulation degradation also in the absence of PD but, of course, failure occurs at much longer times [22].

3.3 Effect of voltage shape: polarity and rise time

3.3.1 Voltage Polarity

The effect of voltage shape can be observed again from Fig. 3.1, where it seems that bipolar square waveforms could be more stressing than unipolar waves having the same amplitude. Anyway, if the results of Fig. 3.1 were plotted as a function of peak-to-peak voltage, no dependence of failure times on the kind of waveform should come out.

On the contrary, Yin observed that failure times are slightly reduced in the presence of bipolar waveforms, with respect to unipolar ones, even at the same peak-to-peak voltage and explained this phenomenon on the basis of a theory relevant to PD mechanisms [34, 48, 56]. Partial discharges, in fact, are generated in the correspondence of the air gap between two twisted enamelled wires. The relevant ionization can produce accumulation of heteropolar charge on the enamel surface generating an electric field opposite to the applied electric field. If the charge diffusion rate is slower than the polarity reversal speed of the applied field, there are periods during which the charge-induced electric field has the same direction of the applied field, reinforcing it and, hence, reducing failure time.

The experimental support to this interpretation is shown in Fig. 3.2, where failure times are reported under different square voltage types: bipolar, unipolar positive and negative. Surprisingly, failure times relevant to bipolar pulses are only slightly shorter than that relevant to positive pulses, while are almost overlapped to those relevant to negative pulses. The slightly longer failure times obtained under positive pulses with respect to those under negative pulses is explained through space charge accumulation which occurs under positive pulses, limiting the resultant electric field. Unfortunately evidence of space charge accumulation are not given, and, thus, all these explanations have to be experimentally proved. In addition, failure times under different voltage types (Fig. 3.2) do not seem to differ each other significantly, being affected by the experimental uncertainty which provides quite large confidence intervals.

For Lebey et al. [32, 47, 50, 58, 60], on the contrary, unipolar waves seem to be slightly more stressing than bipolar ones as it can be seen in Fig. 3.3 [60] at the lowest voltage amplitude, while at the highest ones no difference can be found out about the ageing effect of unipolar or

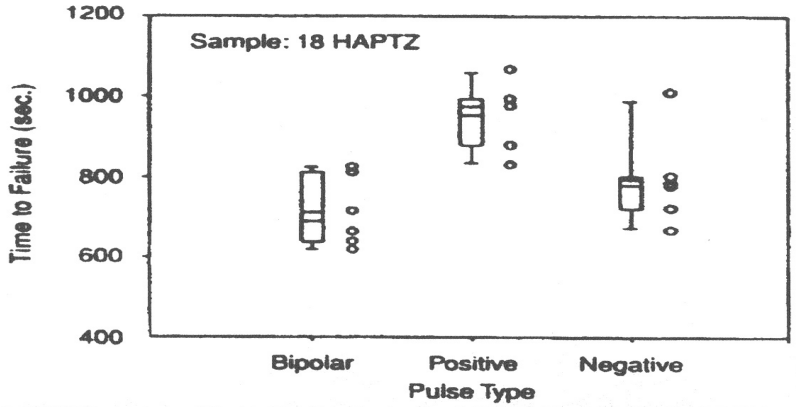

Fig. 3.2: Breakdown times (life) as a function of voltage waveform (bipolar square and unipolar, positive and negative) , having the same amplitude for peak-to-peak voltage V_{pp}=2kV, frequency f=20 kHz, temperature T=90°C, duty cycle D=50%, rise time t_r=0,03 μs (after [34]).

bipolar pulses. Actually, two different ageing phenomena were hypothesised in [61], at high and low stresses, which were associated to partial discharges and to internal degradation. In the latter case a clear tendency to threshold, i.e. to much longer failure times than those expected from the linear relationship, was detected at the lowest-test stresses.

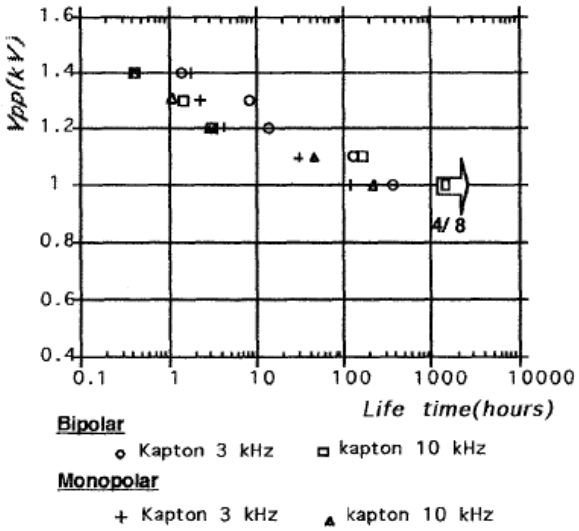

Fig. 3.3: Results obtained from the life tests with square pulsed waveform (unipolar-bipolar) waveform, varying peak voltage and frequency (rise front=1.6 kV/μs; fall front =7 kV/μs, 4/8 means 4 failure over 8 specimens, i.e. singly censored life tests) (after [60]).

3.3.2 Slew rate (rise time)

The previous chapter showed how high slew rate, i.e. short rise times, could affect winding insulation causing spikes, overvoltages and uneven potential distribution across winding turns, especially if cable connecting inverter to motor is long enough. Reducing cable length, a considerable decrease on the extent of overvoltages present at motor terminals can be achieved. However, it is not possible to cancel the negative effect of very high slew rates on failure times, e.g. local dielectric heating increase and space charge formation.

Researchers seem to not agree entirely on the effect of rise time of square waveform generated by ASD on ageing. Yin, for example, observed a change in failure times varying the rise front of the square wave [34, 48, 56]. Figure 3.4 shows the results of tests performed with bipolar square waves (amplitude: 4 kV peak-to-peak, repetition frequency: 20 kHz, duty cycle: 50 %). Considering that the ageing mechanism could be the same, both at very short rise times, below 50 ns, (i.e. very high slew rate) and for longer rise times (up to 150 ns), the life decrease with short rise times can be addressed to dielectric heating due to capacitive current peak, which is very large depending on the time derivative of applied voltage (dV/dt, that is, the slew rate).

On the contrary, other authors found a strong dependence of failure times on medium-range rise times, from 1 to 10 μs, while, unexpectedly, they did not observe any effect for larger or shorter rise times; the results are relevant to tests performed on PET films [44].

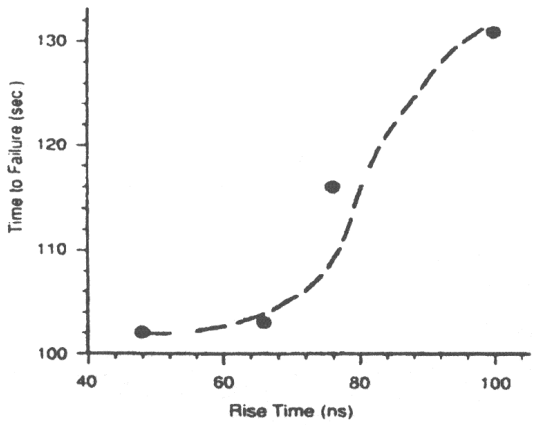

Fig. 3.4: Effect of rise time on ageing acceleration (after [34])

On the contrary, Lebey et al. did not find any significant dependence of ageing on waveform rise time [46, 60, 61].

Kaufhold et al. did not find a significant evidence of wave shape (triangular, square, sinusoidal) influence on insulation ageing acceleration, [39], concluding that ageing could be related mainly to voltage amplitude and wave repetition frequency which can promote partial discharge activity, rather than to shape. Nevertheless, Kaufhold argued that the rise time of the voltage pulse, together with the rate of heteropolar charge accumulation on the enamel surface, can affect PD inception voltage and, thus, breakdown time [45]. Looking at Fig. 3.5A, if the rise time of the voltage pulse is longer than the time constant of the surface-charge build up, τ_σ, the maximum electric field in air can be reduced up to 15% due to heteropolar charge (σ_0) reducing field, while shorter rise-time pulse-voltage cannot be influenced by the benefic effect of the surface charge, so that the electric field in the air gap increases, thus reducing the PD inception voltage and breakdown times (Fig. 3.5B). The fall time of the square waveform shows an opposite behaviour, i.e. the longer fall time, the smaller PDIV and the shorter life.

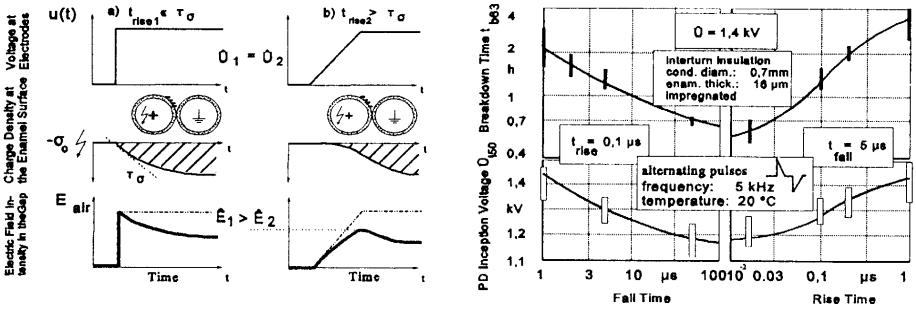

A B

Fig. 3.5: Effect of rise time on PD inception voltage (after [45])

3.4 Effect of pulse repetition frequency

According to Kaufhold [43, 45] and other authors (Foulon, et al. [36]), the number of pulses to breakdown, n_b (at probability 63.2%) is independent of their repetition rate, see Fig. 3.6, because PD number and, thus, degradation is not affected by the rest time between pulses, but depends only on pulse number, if each pulse triggers one PD. Life is, thus, inversely proportional to pulse frequency, so that a motor fed by

an ASD with ten times larger switching frequency will exhibit, if probability of PD occurrence at each pulse is high, ten times shorter life.

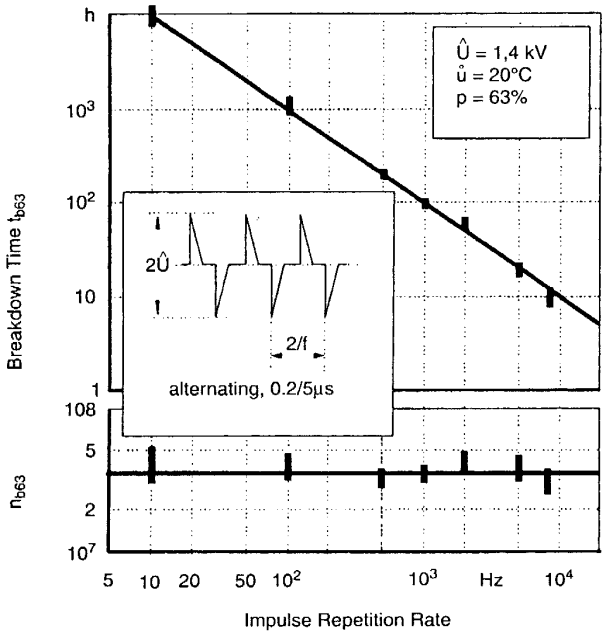

Fig. 3.6: Dependence of number of pulse to failure and breakdown time (at probability 63.2%) on impulse repetition frequency (peak voltage 1.4 kV, temperature 20°C). The relation between life and repetition frequency is linear (after [45]).

Yin [56] observed that, with square waves, the number of pulses until breakdown is almost constant with repetition frequency up to 5 kHz, while at higher frequencies it decreases significantly. In fact, Fig. 3.7 shows that the failure time characteristic provides two different slopes, as function of frequency. Hence, when the frequency is below the transition point (5 kHz), life is inversely proportional to repetition frequency, according to the following equation:

$$L = \frac{B}{f} \tag{3.4}$$

where B is a model constant, while above the transition point (5 kHz, the rate of insulation degradation increases, with respect to linear relation (3.4), that is:

$$L = \frac{C}{f^2} \tag{3.5}$$

(C is a constant).

The reason of these discrepancies could be related to the different test supply waveform used, i.e. pulse waves and bipolar square waves, for Kaufhold and Yin, respectively. With short-pulse waveforms only one PD at maximum is triggered at each applied pulse, while with bipolar square waves increasing the frequency the PD number or energy per period can arise, depending on charge accumulation features of the enamel surface, and this can decrease the number of pulses-to-failure.

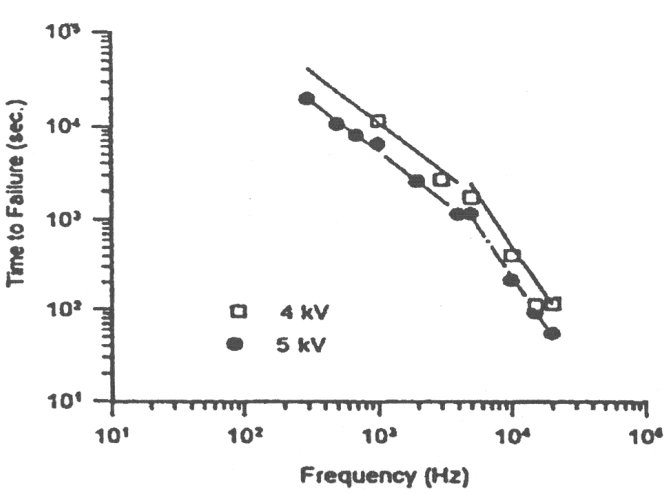

Fig. 3.7: Effect of pulse repetition frequency on insulation failure times. Two mechanisms can be observed, according to [56].

3.5 Effect of duty cycle

Duty cycle (D) corresponds to the duration of the positive pulse, t_P (in seconds), in per cent of the whole period, T (in seconds):

$$D = \frac{t_P}{T} \cdot 100 \qquad (3.6)$$

The results of life tests performed on double layer wires for heavy-duty waveforms are shown in Fig. 3.8 [62]. Increasing duty cycle, breakdown time (life) becomes shorter and this can be explained observing that, if the waveform amplitude is fixed, duty cycle is proportional to rms voltage. Larger rms voltage, in fact, can produce a stronger effect on ageing, both in the absence and in the presence of partial discharges.

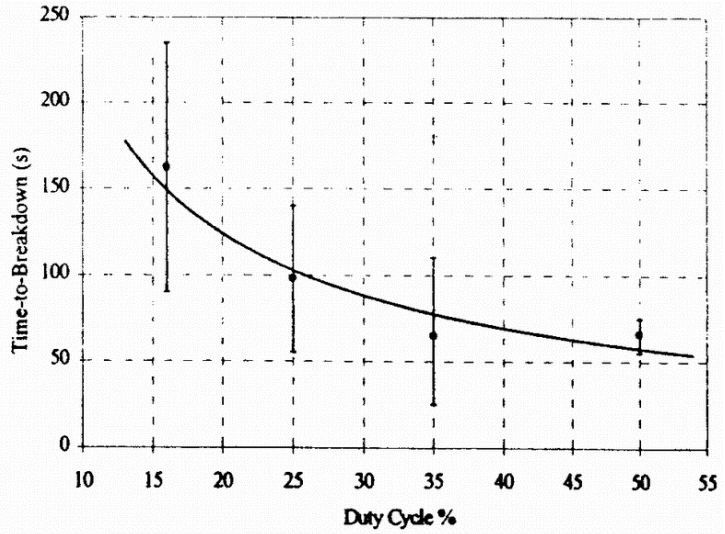

Fig. 3.8: Effect of duty cycle on insulation failure time, (after [62]).

3.6 Effect of dielectric loss increase

It has been mentioned above that the pulsed voltage waveforms generated by ASD are affected by high order harmonic components, from some kHz to MHz, depending on the switching frequency of power converters. Moreover, we saw that impedance mismatch between cable and motor can be the cause of very-high frequency ringings, ranging from a few MHz to some hundreds MHz. The capacitive current, which is proportional to the product $\varepsilon\omega$ (ε is the dielectric constant of insulation at the angular frequency ω) can reach, thus, significantly high values. Since the heating dissipation towards the ambient around can be absolutely insufficient, due to the high repetition frequency of these surges, a considerable increase of insulation temperature, e.g. of 50-60 °C, can occur with oscillating waves at high frequency (e.g. 100 MHz) even for very short time periods [34]. This can accelerate insulation ageing through thermal degradation, but it can also promote PD activity, activating the process of thermoionization.

3.7 Effect of thermal and mechanical stress

If subjected to very high temperatures, magnet wires can be significantly stretched and coils can become loose during service. Moreover, alternate voltage can produce electrodynamic strains inducing coil vibration. Therefore, enamel wire insulation can be affected by surface scratches between conductors and against metallic stator caves, with the possibility that the insulation may become thinner and, thus, weaker.

Figure 3.9, [45], shows the effect of temperature both on PD inception voltage and on specimen capacitance. It is noteworthy that the higher the temperature, the larger the capacitance (hence, the dielectric constant) of the insulating material; this leads to a sort of avalanche effect (positive feedback), because larger dielectric constant means larger impulsive current and, thus, increased heating of wire insulation.

The bottom part of Fig. 3.9 shows a decrease of PD inception voltage as temperature increases, due not only to lower air density (and, thus, decreased breakdown strength), but also to a larger availability of prime electrons for ionization: gas thermal agitation (increased with temperature) decreases energetic band gap between valence and conduction band. A similar result was observed by other authors, e.g. Busch, [40]

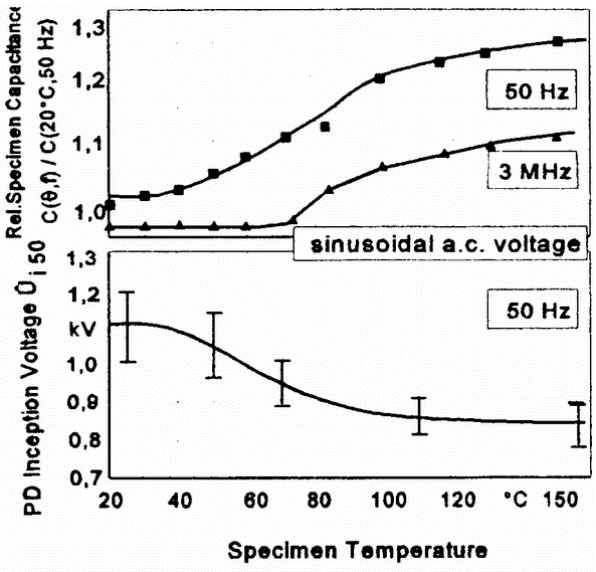

Fig. 3.9: Effect of temperature on capacitance increase and PD inception voltage decrease (after [45]).

3.8 On the PD inception voltage

As it has been shown in the previous paragraphs, PD activity is the main ageing effect which leads to insulation failure. Therefore PD inception voltage (PDIV) is a very important parameter to evaluate. We saw that it depends on temperature and rise time of the waveform and, of course, on insulation system structure.

In literature, PDIV is almost always considered as the ageing threshold, under which no degradation occurs. Therefore it seems that materials with lower PDIV has to be considered as worse insulation. Anyway, Houdon et al. reported that one material, let say #1, may be more able to withstand PD activity than another, let say #2, even if PDIV of #1 is lower than PDIV of #2. Nevertheless, insulation performance depends on the voltage magnitude to which it is subjected. If the applied voltage is larger than PDIV of #1 and #2, life is order of magnitude larger for #1 than for #2. Below PDIV of #2 and above PDIV of #1, on the contrary, degradation occurs only for #1, thus, failure times relevant to #1 are order of magnitude larger than those relevant to #2. Finally, below PDIV of both materials life behaviour is almost the same and no degradation was observed for both of them [54].

These observations show the importance of PDIV measurements for insulating material evaluation: the ability of materials to withstand PD is a fundamental condition, but is not the only one (if its PDIV is low).

In this thesis several PDIV measurements under different voltage waveforms were performed in order to understand better the material electrical behaviour.

Chapter 4

Experimental set-up, test procedures and data processing

4.1 Premise

As it has been highlighted in previous chapters, several factors have been envisaged to be responsible for reliability loss of motor winding insulation. Degradation mechanisms have been hypothesised which are based on partial discharges, space charge accumulation, localised overheating due to peak voltage transient commutations, but ageing mechanisms and prevailing factors of influence are still under investigation.

Several experimental tests were performed during this work, with the purpose of achieving evidences on the effect of space charge accumulation and partial discharge ageing mechanisms of insulation employed in ASD motors

Three testing programs were mainly developed, which consisted of:

1) Life tests
2) Space charge measurements
3) Partial discharge measurements

Life tests, which are quite common to characterise performance of insulating materials, can provide the basis for the comparison of enamelled wires. Space charge measurements on enamelled wires are here shown for the first time, although the effect of space charge is often recalled to explain ageing process. Partial discharge measurements, carried out under pulsed waveforms, constitute a fundamental tool for

insulation evaluation, since they play the most prevailing role on ageing.

Providing information on performance of a given insulating material can be very useful for enamelled wire manufacturers, helping in the design of new materials more able to withstand stress enhancements caused by ASD, as well as for motor manufacturers, in order to test the reliability of their products.

One of the purposes of this thesis is, in fact, to propose a methodology for electrical property evaluation of materials candidate to be used in electrical machine windings.

4.2 Materials under testing

Tests were performed on enamelled wires taken from the market. In particular, four different kinds of enamelled wire were investigated deeply. One is traditional, labelled in the following as #A, and the others belonging to the family of the so-called corona resistant materials, labelled as #B, #C, #D.

#A insulation is based on polyamide-imide, and is commonly used for ac-electrical machine windings designed for 50-60 Hz sinusoidal supply. This kind of material shows, unfortunately, significant reliability loss under ASD voltage waveforms. Being organic, in fact, its degradation proceeds very fast in the presence of partial discharges, which are often the main factor worsening reliability of machine insulation system, eroding the insulation surface, unlike other inorganic materials, e.g. mica-based, frequently used in electrical motor insulation. Moreover, PD generate a huge amount of ozone which is very unstable and an aggressive oxidant (having a bi-radical structure). Ozone contribution to enamel surface oxidation will further on accelerate degradation.

Motor manufacturers are investing in research to increase reliability of motor insulation, focusing on the development of new insulating enamels, filled with inorganic oxides, more able to withstand PD erosion and oxidation amplification when motors are subjected to ASD voltage waveforms than conventional insulation. Materials #B, #C and #D are corona-resistant enamelled wires built by different manufacturers. They are made by polyamide-imide insulation containing inorganic additives, typically metallic oxides (e.g. TiO_2, CrO_2, etc.).

Pictures of the surface of the four enamels under tests, obtained by a scanning electron microscope (SEM), are provided in Fig. 4.1. It can be

noted clearly that #A shows several tracks, micron-order wide, parallel to the extrusion direction (indicated by thick white arrows). Two of the corona resistant materials, #B and #C, show microcavities and swellings, likely due to the presence of metallic oxides on the polyamide-imide matrix, while material #D is affected by tracks 8-10 μm wide, oblique to the extrusion direction.

These observations can be related to the surface endurance to electric stress: very rough surface may cause local electric field enhancement and charge density concentration on the surface physical defects.

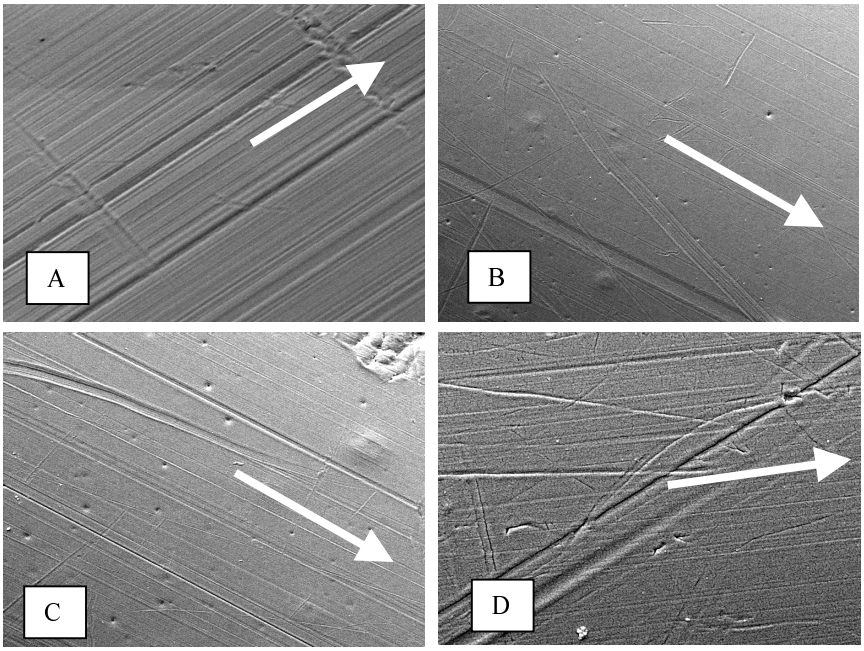

Fig. 4.1: Pictures of the insulation enamel surface observed by an electronic microscope, for material #A (a), #B (b), #C (c) and #D (d) -1250 enlargements.

The choice of test objects to be used for electrical insulation characterisation, is still widely debated. Performing these tests directly on motors or reduced-scale models would be preferable, since insulation would be stressed by voltage waveforms similar to those found in service and discussed in the second chapter. However, in the case of life tests, and, in general, of destructive tests, a statistical analysis of the results is needed. Hence, each life test should be performed on samples of at least 5 specimens. Moreover, life lines can be obtained only through tests at different levels of voltage, larger than the operating

voltage (in order to accelerate test duration) which may not be available easily with motors or scaled models. Likewise, the possibility of varying the rate of voltage rise in a broad range, duty cycle, frequency (i.e. parameters which have been associated with accelerated degradation) may be not achievable if the object under test absorbs large power. On the whole, investigation of the degradation mechanisms under pulsed waveforms may be difficult or, even, too expensive if motors are used. Hencefrom cheaper and simpler models, e.g. the twisted pair, may be preferable in order to investigate motor winding behaviour. A twisted pair is composed by two enamelled wires wound as a plait. The necessary mechanical strength is given, during the winding stage, by applying a given tensile strain. The number of plait turns, the pitch, the whole length, as well as the tensile strain, are suggested by the current standard ASTM D-2307 [63], where these values are given as a function of wire size. An example of twisted pair, with its main geometrical characteristics, is sketched in Fig. 4.2.

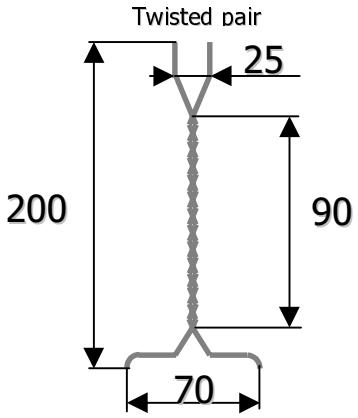

Fig. 4.2: Example of twisted pair (dimensions in mm).

During life tests, one wire is connected with high voltage supply, the other with ground. When voltage is applied to a specimen, some micro-discharges, localised where the electric field is higher, can be triggered in the air gap between the two wires. The specimen typology, thus, can reproduce the critical situation of narrow contact between the first and the last turns of the input coils of an ASD-fed motor, which is characterised by large potential differences between wires and by the presence of small partial discharges.

The main problem related to the choice of such simple test objects is the kind of voltage waveform to be used. This problem is addressed in a very recent IEC standard, i.e. IEC 62068 [59], where test methodologies, suggested waveforms and criteria for performance comparison of specimens made by different insulations, are reported.

Another fundamental aspect of designing life tests is that quite high test voltage levels must be chosen in order to accelerate at maximum degradation (to shorten test times), but degradation mechanisms must not change with respect to those expected in service: for example if the insulation system in service works in the absence of PD, also the maximum test voltage must not incept PD in the test arrangement. This establishes an upper limit to test voltages, that is, a lower limit to life test duration.

Referring to this work, life tests and partial discharge measurements were performed on twisted pairs. Space charge measurements were performed, on the contrary, on enamelled wire segments (coaxial geometry), since twisted pairs geometrical features would have not allowed to realise a proper test cell.

4.3 Life tests

As discussed in the previous chapters NEMA standard recommendations [29, 30], which fixed a limit on the slew rate of 0.5 kV/μs for general purpose motors and of 1.6 kV/μs for inverter-fed motors, need to be updated for the new generations of power converters already on the market or on the way to come. Improvements on insulating material performance would be preferable than fixing limits on slew rate, in order to take profit of all the potentiality of new power electronic components. Indications on the procedures for life tests having the purpose of comparing different materials candidate for applications in ASD motors are provided, as mentioned above, by IEC 62068 [63].

4.3.1 Voltage waveforms

When ageing tests are performed on twisted pairs, and not on motors, the first problem to face is the kind of waveform to be used in order to reproduce the electric stress inside a motor winding affecting, e.g. interturn, phase-to-ground or phase-to-phase insulation.

In the second chapter the kinds of voltage waveforms which may

affect motor winding insulation have been highlighted. The characteristics of these waveforms (slew rate, frequency spectrum, amplitude, shape, etc.) depend largely on the type of motor-cable-inverter arrangement, so that an infinite collection of kinds of waveforms can affect the insulation of a motor. Hence the waveform to be chosen for twisted pairs cannot, and does not have, to replicate the voltage waveforms which affect motor insulation, but must have the capability to reproduce the most significant ageing factors for winding insulation discussed in the previous chapter, e.g. peak value of applied voltage, pulse repetition frequency, rise time and shape (unipolar, bipolar, etc.) [63].

The voltage waveforms used in this work are, therefore:

- 50 Hz sinusoid, in order to evaluate the insulation behaviour at supply frequency as a reference for the other tests.
- 10 kHz sinusoid, to be compared with the results at 50 Hz in order to investigate the effect of repetition frequency on ageing.
- Bipolar square waveform, in order to reproduce the electric stress relevant to phase-to-ground voltage (bipolar, with variable pulse width) and turn-to-turn voltage. The frequency chosen was 10 kHz, which is at the upper limit of the switching frequency used commonly in power converters.
- Unipolar square waveform, which would reproduce the effect of each pulse train characterising the phase-to-phase voltage. The pulse polarity chosen was positive, with a repetition frequency of 10 kHz.

4.3.2 Experimental set-up

The life test experimental set-up is constituted by three different systems, depending on the voltage waveform that has to be generated. For sinusoidal waveforms, a system based on HV transformer was used (par. 4.3.2.1), while for unipolar and bipolar square waveforms two generators employing solid-state components were built (they are described in paragraphs 4.3.2.2 and 4.3.2.3, respectively).

4.3.2.1 Sinusoidal waveform test apparatus

A block scheme of the experimental set-up for life tests with sinusoidal waveform, both at 50 Hz and at 10 kHz, is shown in Fig. 4.3.

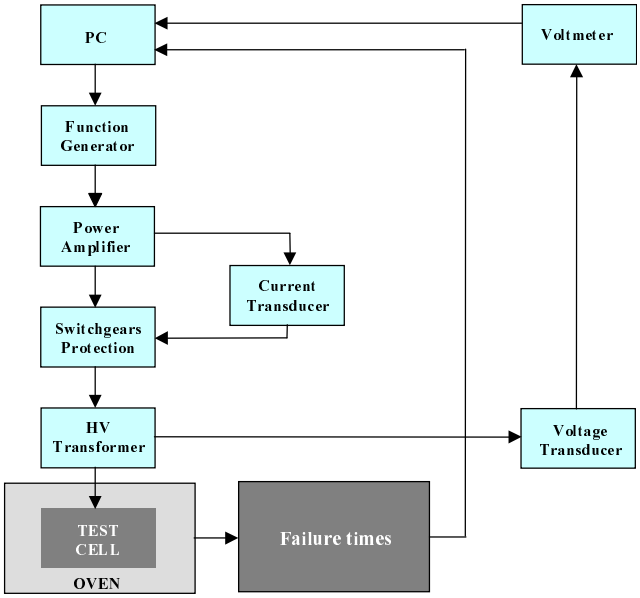

Fig. 4.3: Set-up for sinusoidal life tests.

A function generator provides the low-voltage sinusoidal waveform (±10 V peak-to-peak) at the desired frequency, then the signal is amplified in voltage and current by a linear power amplifier (bandwidth 0.015 - 10 kHz). An elevator transformer, providing a maximum voltage of 15 kV rms, is, thus, connected to increase further the voltage amplitude, needed to perform accelerated life tests. The specimen (twisted pair) is then inserted between high voltage electrode and ground. The parameters of the voltage waveform provided by the function generator and, thus, those applied to the specimen (e.g., amplitude and frequency) can be controlled through personal computer (PC). Moreover, the PC is able to record voltage level and the failure times, that is, the time elapsed from test beginning until specimen breakdown. The breakdown is detected by a current transducer, in series to the primary winding of the HV transformer, which transmits the command of circuit opening when the current exceeds a fixed threshold, meaning that a specimen failed.

Since it was very difficult to find an HV transformer able to work in the range 50 Hz - 10 kHz, we decided to use two different transformers, one, traditional, with a frequency response from 50 to 1000 Hz and the other, designed appropriately for high frequencies, ranging from 5 to 15 kHz.

4.3.2.2 Unipolar square wave test apparatus

The apparatus for life tests with unipolar square waveforms consists of three basic modules, fully controlled by a personal computer: the HVDC power supply, the HV switch, the control and protection circuit. PC user interface allows all the waveform characteristics to be set, that is, voltage magnitude (up to 8 kV), rate of voltage rise (slew rate) of the square wave (up to 7 kV/μs), switching frequency (up to 20 kHz), adjustable duty-cycle (from 0.01% up to 99%). A scheme of the system set-up is provided in Fig. 4.4.

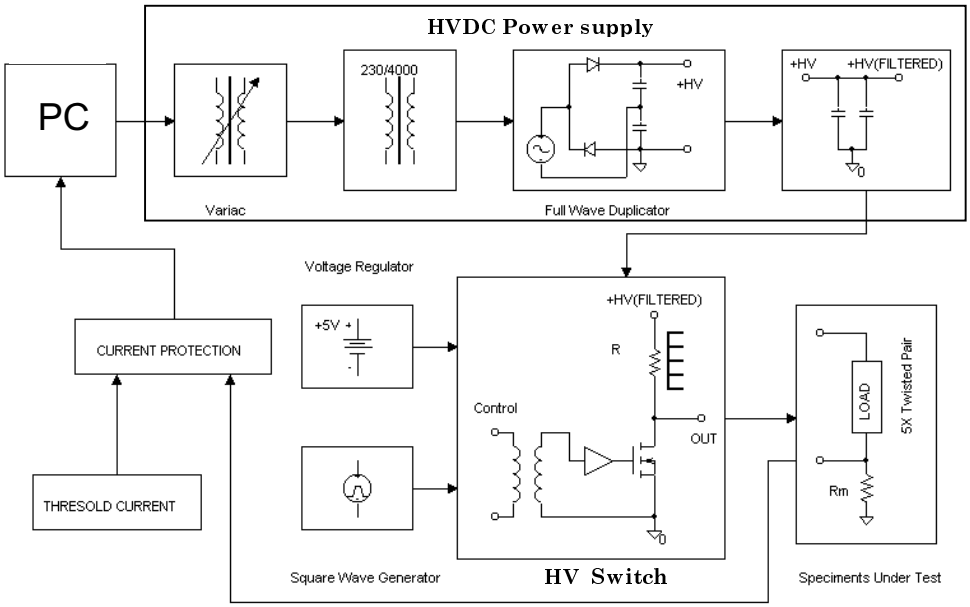

Fig. 4.4: Scheme of the unipolar life test apparatus.

The high voltage DC power supply is obtained rectifying, through a full wave duplicator, and filtering the output voltage of an elevator transformer 230/4000 V. The amplitude of the DC high voltage can be changed by means of a variable-ratio autotransformer which supplies the elevator transformer.

The high-voltage module is a solid-state switch, employing MOS-FET technology. One of the two power contacts of the switch is grounded, while the other is connected to the HVDC bus through a series of load resistors R of values ranging between 3 and 15 kΩ. One terminal of the specimens (twisted pairs) is connected to the static modulator on the

load-resistor-side, the other is always grounded. In this way, when the switch is opened the terminal of the specimens out of ground is connected to the HVDC bus, through the load resistors, so that the specimens are subjected to the whole HVDC voltage available. On the contrary, when the switch is closed, the same terminal is grounded, thus no voltage is provided to the specimens. The opening and closing commands for the switch are given by a low voltage square wave generator (0-5 V_{PP}), controlled by PC. A current control is performed in order to protect the circuit against short-circuits which occur at each specimen fail, opening in very short times (< 5 ms) the supply voltage, in order to avoid possible MOS-FET burnout; the failure time of each specimen is, finally, recorded by PC.

The load resistors, *R,* have the main purpose of limiting the current that flows to ground when the switch is closed; in fact without load resistors, closing the switch, the HVDC supply would be short-circuited. The minimum value of the load resistors R is related to the maximum peak current the switch can stand. Moreover, the desired rate of voltage rise depends on the value of R: at switch opening the specimen capacitance C_L is charged through load resistors. The time constant of this charging process is $\tau = RC_L$ and, thus, the larger R, the longer the rise time (or the smaller is the rate of voltage rise).

A typical unipolar voltage waveform obtained from the square wave generator here described is reported in Fig. 4.5 (peak voltage = 4 kV, frequency = 10 kHz, duty cycle = 50%, rise front = 1.5 kV/μs).

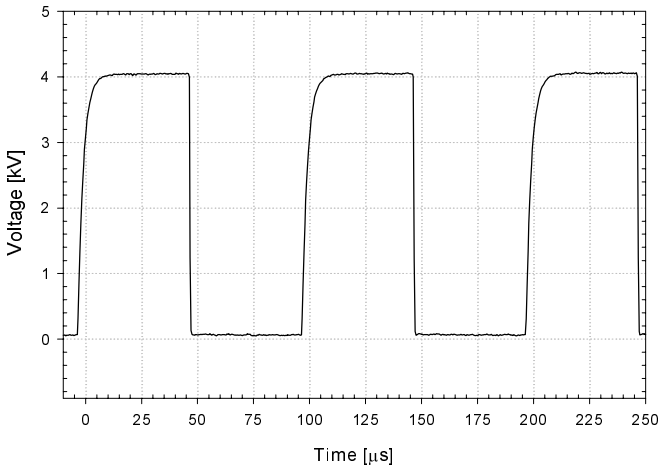

Fig. 4.5: Example of typical unipolar waveform used during life tests. The peak value is 4kV and the slew rate 1.5 kV/μs.

4.3.2.3 Bipolar square wave test apparatus

The experimental set-up used for tests with bipolar waveforms, reported in Fig. 4.6 is more complicated than that relevant to tests with unipolar waveforms, described in the previous paragraph.

First of all, the HVDC power supply must be doubled, in order to provide bipolar (+ or -) high voltage with respect to ground. The same holds for DC filter.

The high voltage module is composed by two MOS-FET solid state switches, each one similar to that used in the unipolar system. The two switches are connected in series and controlled in a push-pull way, meaning that when one is closed, the other is opened and *vice-versa*. The two power terminals of the module are connected to the bipolar supply through two resistors, R_s, of value ranging between 30 and 300 Ω, significantly smaller than that used in the unipolar generator. One of the main advantages of the push-pull configuration, in fact, is the lack of a large load resistors. As said above, in regular service (no short-circuit) the two solid-state switches are not allowed to be both closed or opened at the same time. This means that current depends only on the load: for high impedance (capacitive) loads such as twisted pairs, the average current is, thus, very small. Resistors R_s are needed only to limit the peak current at each commutation. In normal operation, in fact, switches have to charge, with positive and negative polarity, the capacitances provided by twisted pairs. Let us suppose that specimens are positively charged, i.e. with the upper switch (n- channel MOSFET of Fig. 4.6) closed. Then, this switch opens and the bottom switch connected to the negative high voltage bus closes. The charge accumulated on the specimen capacitances has to be discharged towards the negative high voltage generator. The current peak determining the discharge is limited only by R_s and the internal resistance of the solid state components. The charge which interests this transient is provided almost exclusively by means of bypass capacitances C_b. Increasing the rate of voltage rise (decreasing rise time) the peak current will increase. Rise times are limited by R_s which, in this case, are small, so very high rate of voltage rise are allowed.

PC user interface allows all the waveform characteristics to be set, that is, voltage magnitude (up to ±7.5 kV), rate of voltage rise of the square wave (up to 80 kV/μs), switching frequency (up to 10 kHz), adjustable duty-cycle (from 0.01% up to 99%).

As for every life-test experimental set-up, a protection circuit, here based on Hall-effect current transducer, is used to disconnect selectively

supply voltage when a specimen fails, recording the relevant failure time.

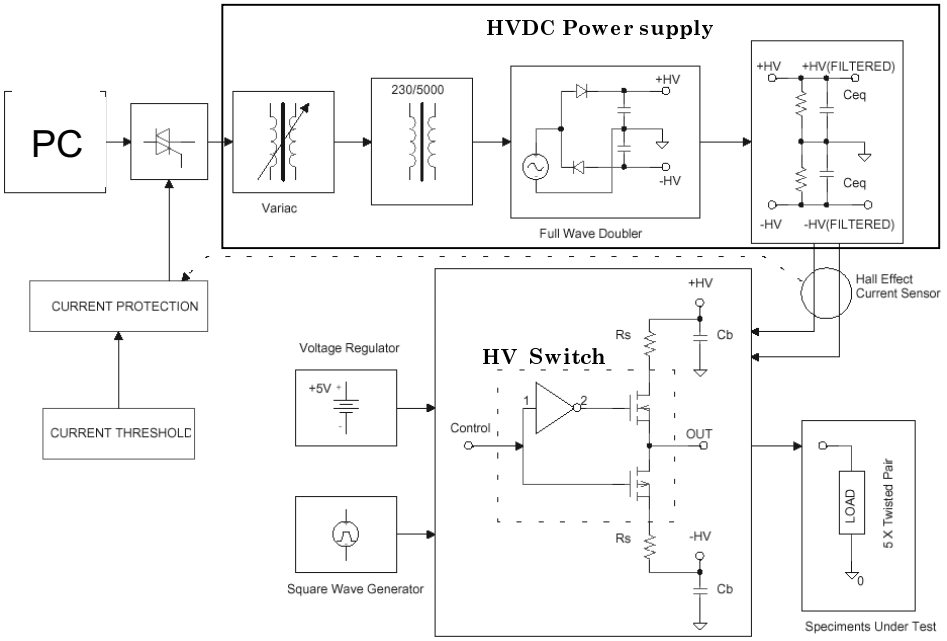

Fig. 4.6: Scheme of the bipolar life test system.

A typical bipolar voltage waveform obtained from the square wave generator is reported in Fig. 4.7 (peak-to-peak voltage = 8.4 kV, frequency = 10 kHz, duty cycle = 50%, rise front = 15 kV/μs).

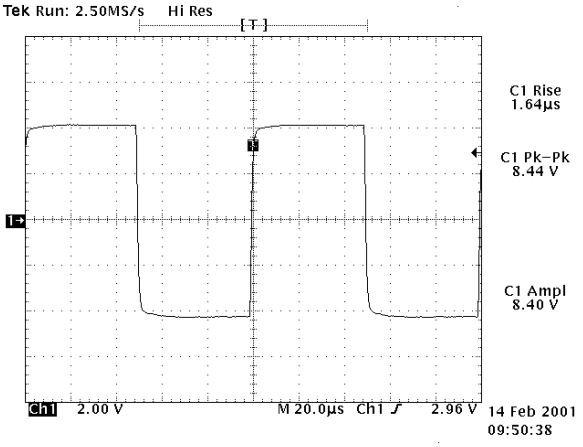

Fig. 4.7: Example of bipolar waveform used for life tests. The peak-to peak value is 8.4 kV. The slew rate is 5.3 kV/μs.

4.3.3 *Test procedures and statistical analysis of life test results*

A life test is performed on a sample of specimens applying a voltage waveform, whose characteristics (frequency, amplitude, rms, rise front, etc.) are kept constant during the test, until one of the specimens fails (insulation breakdown). At this time the failed specimen is automatically disconnected while ageing goes on for the other specimens, until all or large part of them fail (complete or censored life tests, respectively). Failure times are different, even in the same test conditions, since solid insulation is never completely homogeneous, due, e.g. to imperfections both in micro and in macro scale. Hence, failure time data must be processed by statistical analysis tools which can provide failure time estimation for a sample at a given failure probability (e.g. median value, etc.), with the relevant confidence interval. In our experimental tests samples of 5 to 7 twisted pairs were used, and the relevant failure times are processed through the two-parameter Weibull probability distribution [64]:

$$F(t_F) = 1 - \exp\left[-\left(\frac{t_F}{\alpha}\right)^{\beta}\right] \tag{4.1}$$

where t_F is failure time, α is scale parameter (corresponding to 63.2% failure probability) and β is shape parameter associated with data dispersion (β is inversely proportional to sample variance). Figure 4.8 shows an example of data reported in Weibull plot, together with the relevant Weibull graphs, obtained applying the Least Squares Regression (LSR), and the 95% confidence bounds [65]. The data are relevant to three life tests performed on material #A with bipolar square wave at 10 kHz.

Figure 4.9 indicates the way to achieve life lines:

1. A failure probability (e.g. 50% or 63.2%, etc.) for life model shall be fixed.
2. From equation (4.1) or Weibull plot, the failure percentile with probability indicated at previous item 1 can be obtained for each life test performed at different voltage levels.
3. The percentiles with the relative confidence interval are plotted as function of voltage, obtaining the so-called life plot. The life

plot co-ordinates should be chosen in such a way that the life law can be described by a linear relationship, i.e. experimental points fit a straight line. In such a way, the life line parameters can be calculated by the LSR statistical technique.

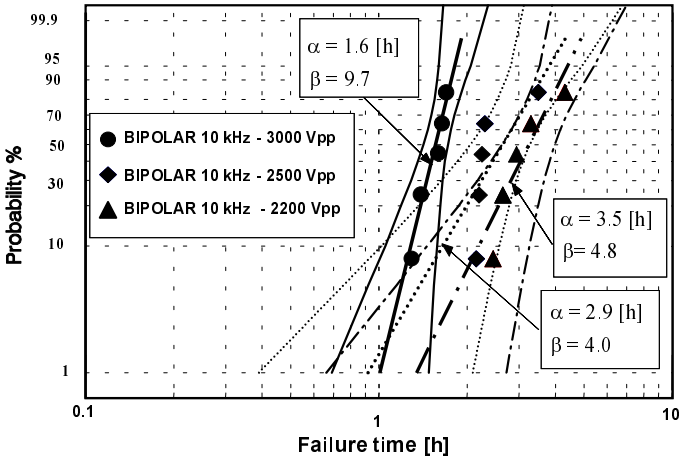

Fig. 4.8: Examples of data reported in Weibull plot together with the relevant Weibull graphs. Life tests performed at V_{pp}=2200, 2500 and 3000 V bipolar pulses.

For the life tests here reported, failure times fit quite well to the Inverse Power Model (IPM), which provides a straight line in a log-log plot (Fig. 4.9), that is [66]:

$$t_F = kV^{-N} \qquad (4.2)$$

where V is the applied voltage, t_F is breakdown time (life) at voltage V, k and N are parameters of the model. The latter, the so-called Voltage Endurance Coefficient, VEC, [66] is a measure of the ability of the material to withstand the voltage stress during its life: the higher VEC, the larger endurance. Let us note that the slope of the life line provided by the IPM model is inversely proportional to the voltage endurance coefficient. It must be emphasised once again that the fitting to a linear model, in a given test range, is the consequence of test voltage choice which triggers the same ageing mechanism at each voltage level.

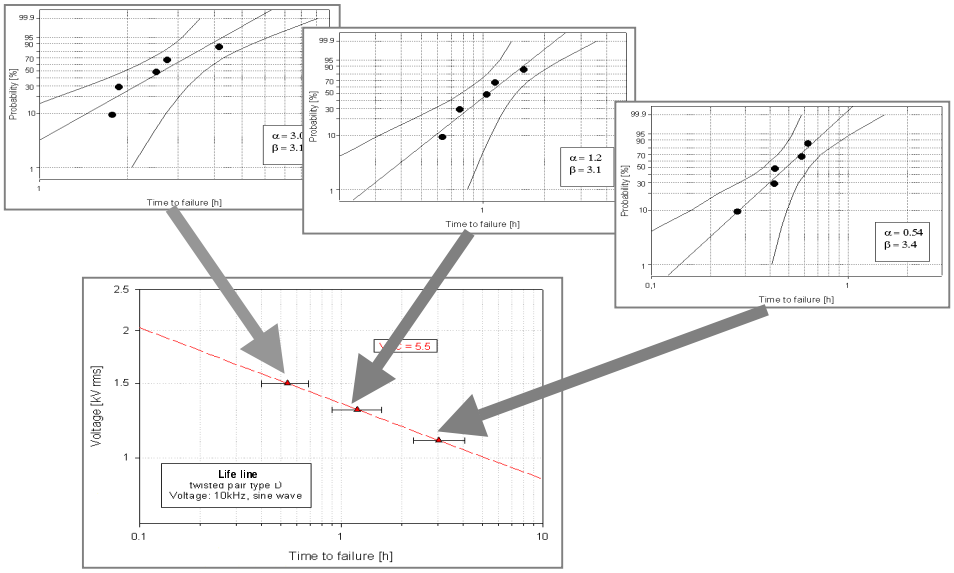

Fig. 4.9: Weibull plots and life line derivation

4.4 Space charge measurements

With the term "space charge" we mean the charge accumulated in the insulation (bulk and interfaces), with respect to neutral conditions, due to injection, molecular dissociation or ionization [67-83].

It has been observed that space charge accumulation is a typical phenomenon occurring in materials subjected to high electric fields [67-83]. The extent and way of accumulation depend on material microstructure and chemical-physical characteristics, electric field magnitude, temperature, pressure and environmental conditions.

The design of insulation systems, usually, does not take into account space charge, considering the insulation as ideal, i.e. the charge is present only on the electrodes, and this leads the field inside insulation to be laplacian. On the contrary, space charge accumulation can give rise to local electric field enhancement and, consequently, increased electromechanical stress, which my affect considerably the ageing rate of polymeric materials.

Some authors have explained differences between life performance of materials used in magnet wires hypothesising space-charge build up phenomena. In [39, 84] it is argued that the amount of space charge in

flat specimens depends on the supply waveform and may affect intrinsic ageing (in the absence of partial discharge activity).

Space charges in insulation may be generated by several factors, mainly:

- Charge carrier injection from electrodes or defects inside insulation;
- Dissociation, ionization of chemical species in the material;
- Contamination coming from conductor or semicon, or from the environment surrounding insulation.

Regarding charge carrier injection inside insulation, electrodes may inject both negative (electrons) and positive (holes) charges through the electrode-insulation interfaces. These processes depends strongly on interface conditions, which include material constituting the electrode, superficial defects, impurities and oxidation. Space charges are accumulated in the insulation only if injected charges are trapped, and this phenomenon depends on the trap density and depth in the insulating material (the time during which a charge carrier remains inside a trap depends on trap depth). Of course, the amount of space charge depends strongly on both electric field and temperature; in particular, space charge density increases with electric field and temperature.

Space charges are also classified in relation to their sign with respect to that of the closest electrode (Fig. 4.10). Homocharge indicates charges having the same polarity of that of the closest electrode (it is often generated by charge injection). The resulting space charge distribution reduces the local electric stress near the electrode, but increases the field inside the insulation. Heterocharge indicates charges of opposite polarity with respect to the closest electrode (it may be generated by ionization of dissociable species). When electric field is applied, in fact, electrons and positive ions, generated through dissociation, travel to the electrode with opposite polarity, where they can be trapped. The effect is a field enhancement near the electrodes and, consequently, a reduction in the insulation bulk.

It seems interesting to investigate the effect on space charge accumulation of additives and fillers which have been introduced in enamelled wire insulation to better withstand PWM-like supply waveforms. The additives introduced during the productive process of enamelled wires, e.g. inorganic oxides of corona resistant materials, anti-oxidant or other impurities, can, in fact, constitute additional interfaces or centres (traps) where space charge can accumulate.

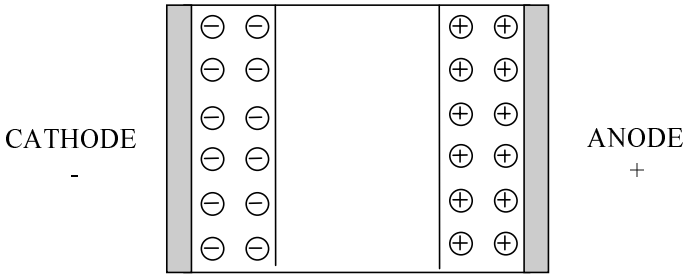

a) HOMOCHARGE

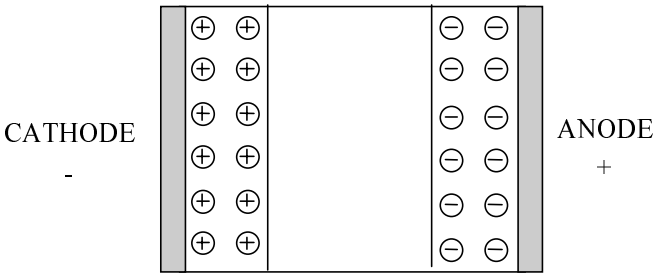

b) HETEROCHARGE

Fig 4.10: Space charge accumulation: homocharge (A) and heterocharge (B)

4.4.1 Experimental set-up

The research in the last years has brought to the development of different space charge measurement techniques which enable the observation of space charge. Among these, the pulsed electroacoustic (PEA) method is the most largely assessed. With this technique the one-dimensional space charge distribution along the thickness of the insulation can be obtained [67, 69, 81].

A scheme of the new PEA system developed with the purpose to measure space charge accumulation on enamelled wires in DC is reported in Figs. 4.11 and 4.12. This system is realised starting from the PEA version for power cable described in [85].

A front view of the test cell realised is shown in Fig. 4.11 [86]. The enamelled wire under test can be correctly positioned on the aluminium ground plate through the central fixing screw on the support structure (note that the dimensions are not in scale). The circuit diagram is reported in Fig. 4.12.

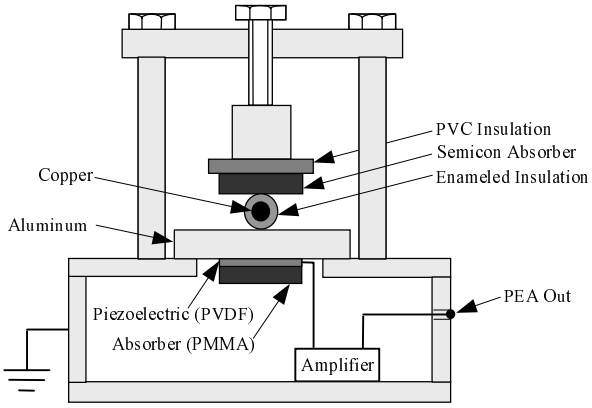

Fig. 4.11: Front view of the PEA measurement cell.

The specimen is fed by an high-voltage DC power supply. A voltage pulse, with an amplitude of 300 V, 10 ns width, repetition frequency of 110 Hz, is applied to the specimen through a 220 pF coupling capacitor. Each voltage pulse generates an impulsive electric field inside the specimen which exerts a force on the charge present in insulation, with an amplitude proportional to the net local charge. A pressure wave profile is generated from the interaction between the electrical force and the material structure, propagating through the insulation at the sound velocity. This profile is divided into two waves, propagating in two opposite directions. Each wave has the shape of the original profile, but the amplitude function of the sonic impedance encountered in the two propagating directions. One wave passes through the upper surface of the enamelled insulation and is absorbed by a thick semicon layer, in order to avoid signal reflections. The other wave propagates through the insulation down to the lower aluminium ground electrode under which the piezoelectric transducer is located. The piezoelectric transducer (PVDF) generates a voltage signal (PEA output signal) proportional to the pressure wave propagating through it. The weak voltage signal generated by the PVDF is then amplified by two large-band amplifiers, sent to an oscilloscope and recorded by a personal computer, connected with the oscilloscope through an IEEE-488 bus. A PMMA absorber is located under the piezoelectric transducer in order to avoid reflections which can disturb the PEA output signal.

Since the PEA pulse repetition frequency is 110 Hz, we obtain 110 PEA output signal per second which can be averaged from the oscilloscope in order to reduce the noise.

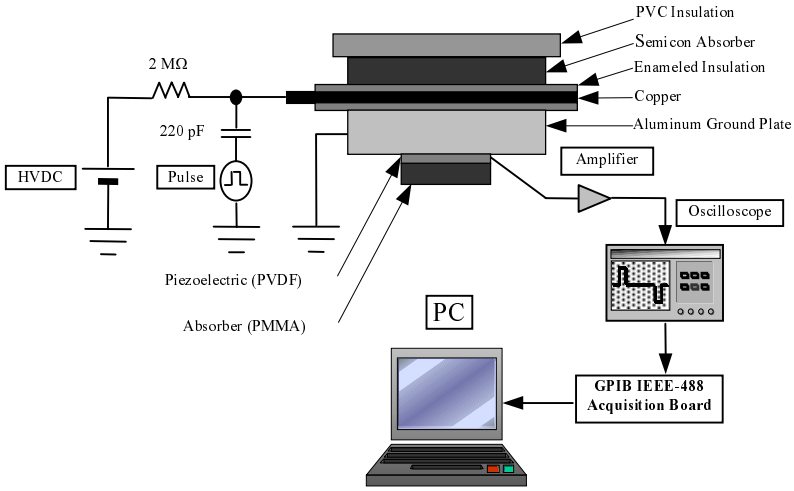

Fig. 4.12 Circuit diagram of the PEA measuring cell

The main difference, with respect to the other PEA systems developed in the past, is the specimen to be tested. Till now systems have been developed for flat specimens or thick power cables. PEA measurements on enamelled wires present specific features and difficulties. Due to the small size of the wire (diameter of about 1 mm) the contact with the aluminium ground plate may be unsatisfactory. Moreover, the small thickness of the enamelled insulation (30-40 μm) requires the use of a very short pulse and a very thin transducer, in order to achieve a good spatial resolution needed for such thin insulation.

The experimental set-up above described can perform space charge measurements under DC voltage or AC at very-low-frequencies. For higher frequencies (>1 Hz) a different acquisition system must be used and, thus, the measurement circuit becomes more complicated. PEA system for space charge measurements under square waveforms with frequencies up to 10 kHz is shown in the Fig. 4.13. First of all, the PEA measurement pulse must be synchronised with the supply voltage and its repetition frequency has to be largely increased in order to perform the average on a large number of samples, even with highfrequency supply voltage. Then, the oscilloscope has to be substituted by a digital signal averager capable of very fast averages on a large number of samples acquired. In burst mode, the pulse generator can provide a burst frequency up to 1 MHz, that can allow to perform an average on a significant number of samples even with high-frequency supply waveforms.

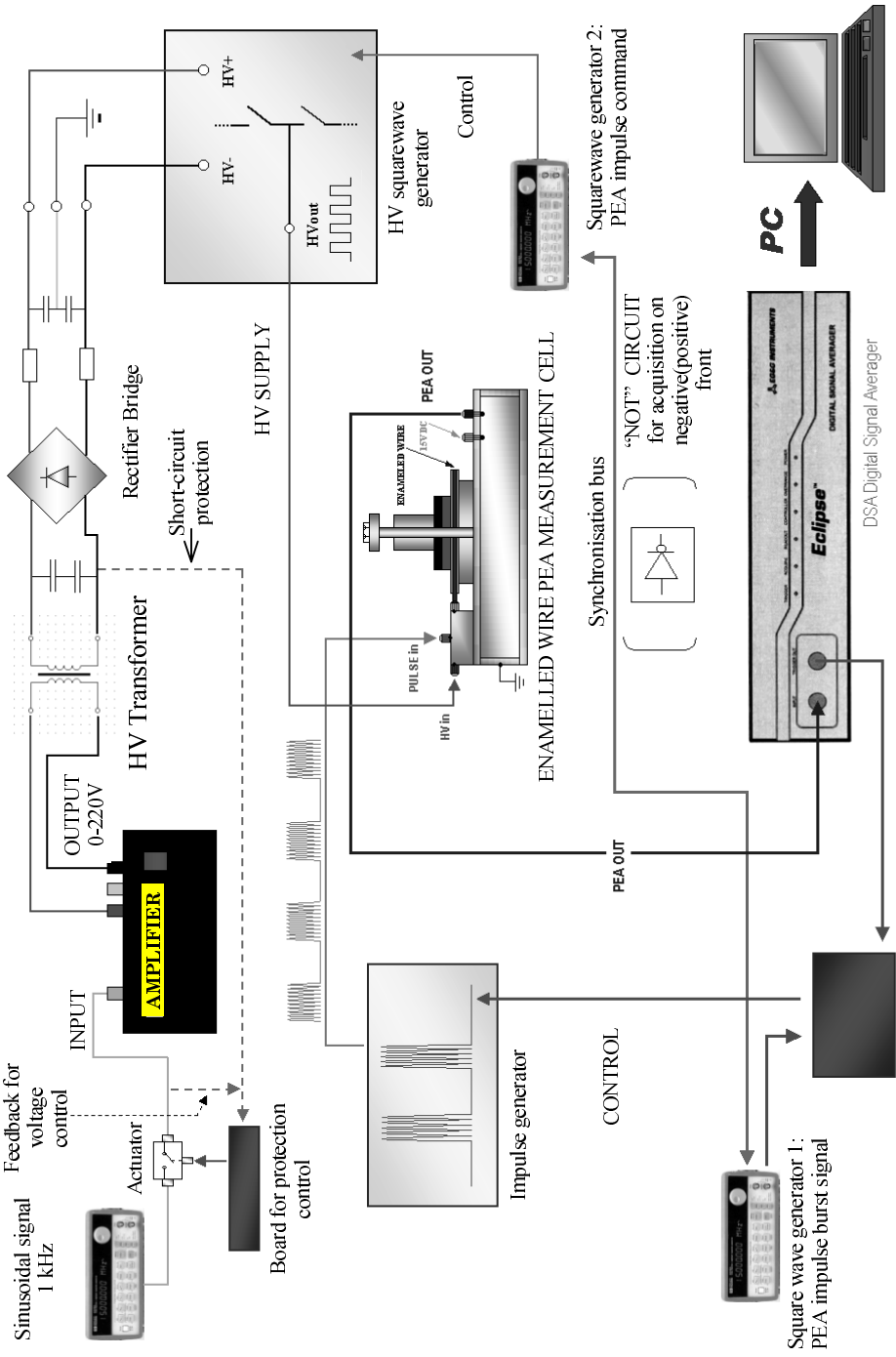

Fig. 4.13: Experimental set-up for PEA measurements under square waveforms

The pulse burst is generated for the whole half-period of the supply voltage (positive or negative), as can be seen from Fig. 4.14.

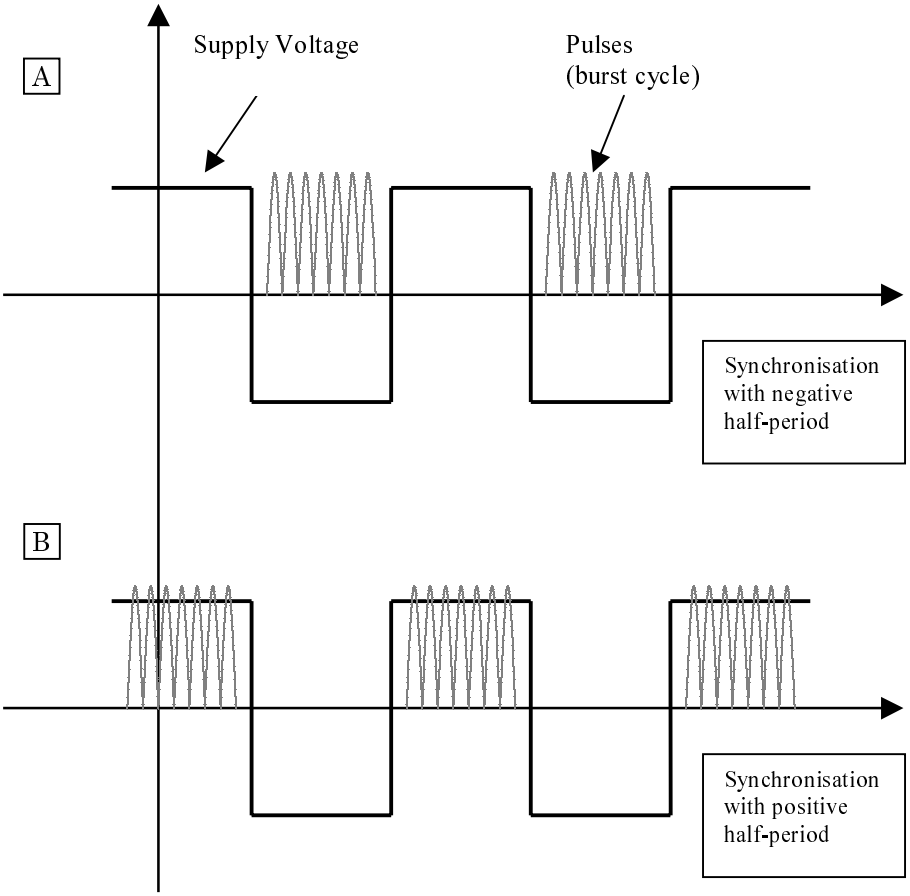

Fig. 4.14: Synchronisation of PEA measurement pulse with supply voltage: negative (A) and positive (B) half-period.

PEA pulse train is synchronised with a certain delay with respect to the rise or fall front of the supply voltage where the commutation transients can provide misleading signals. The control signal of the pulse generator is provided by a burst cycle, i.e. a cyclic wave constituted by a given number of pulses. Both the number of pulses and the frequency of the cyclic wave can be adjusted on the front panel of the square wave generator 1 of Fig. 4.13

4.4.2 Test procedure

Space charge measurements were carried out according to a polarisation/depolarisation procedure like that illustrated in Fig. 4.15. The polarisation time (t_P=3600 s) during which the poling field is applied (volt-on) is long enough to achieve a steady-state for the accumulated charge. Depolarisation (volt-off) is realised removing the supply voltage and grounding the high voltage electrode.

Typical space charge profiles obtained during volt-on (20 s after the beginning of polarisation) and volt-off (2 s after the beginning of depolarisation) are reported in Fig. 4.16 for material #B under DC supply voltage. It can be observed that after 20 s the signal peaks indicate the electrode (anode and cathode) location, corresponding to the positive and negative signal peaks, respectively (note that the large negative peak represents the ground electrode, the nearest to the piezoelectric transducer). Since charge does not appear in the insulation bulk, the likely presence of injected charge at the electrode-insulation interface should be hidden by the electrode charge. Space charge in the insulation bulk can be observed, on the contrary, from the profile taken under volt-off (t=3602 s, grey area of Fig. 4.16). This charge is generated by progressive drift from electrode interfaces to the bulk, as poling time increases. It is noteworthy that the electrode charge is considerably smaller, when the poling field is removed, than under polarisation, being only due to the image charge (of the internal charge).

In order to evaluate immediately the time evolution of space charge profiles of Fig. 4.16 during polarisation and depolarisation, coloured patterns can be used (Fig. 4.17). Polarisation and depolarisation time is reported on x-axis and specimen thickness on y-axis. Coloured scale indicates the amplitude of accumulated space charge at a given time in a particular location of insulation bulk. It can be clearly seen charge accumulated on the two electrodes positive (anode) and negative (cathode), inner charge, as well as charge drifting when voltage is removed after 3600 s.

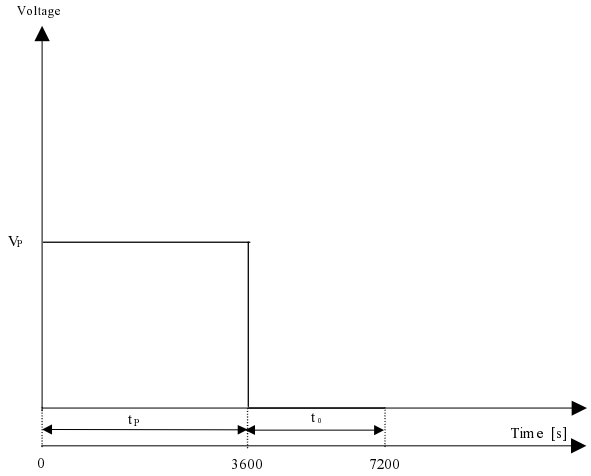

Fig. 4.15: Poling procedure for space charge measurements. V_P and t_P = 3600 s are the poling voltage and time, t_0 = 3600 s is the depolarisation time.

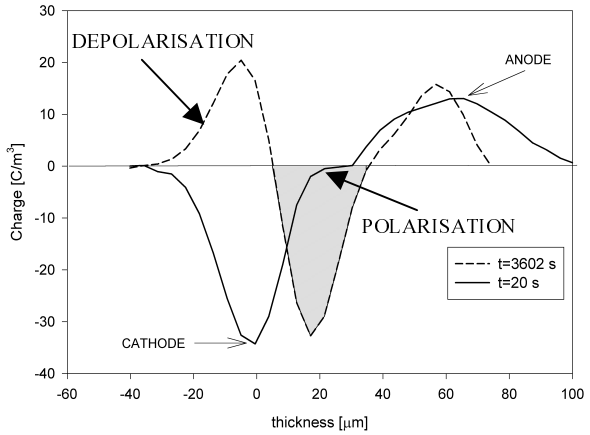

Fig. 4.16: Example of volt-on (t = 20s) and volt-off (t = 3602s) charge profiles. Material #B.

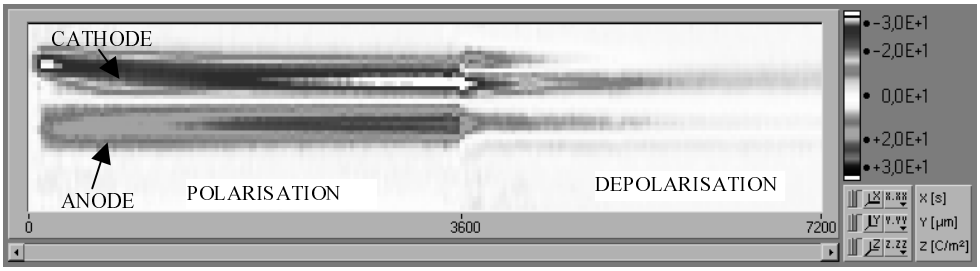

Fig. 4.17: Example of space charge pattern for test on material #B. Poling voltage: 1000V DC.

4.4.3 Data processing and quantity definition

Significant parameters, like stored charge density and rate of charge depletion, can be derived from the profiles acquired in order to be used as indicators of the space charge behaviour of the material [83].

The total absolute stored charge density after grounding can be calculated as [83, 86]

$$Q_{VO}(t) = \frac{1}{(x_1 - x_0)} \int_{x_0}^{x_1} |Q(x,t)|\, dx \qquad (4.3)$$

where x_0 and x_1 are the electrode positions (induced charges at the electrodes are not taken into account), t is the time at which the measurement is done (generally, t corresponds to a given depolarisation time).

A quantity which is useful for further analysis can be calculated from eq. (4.3), i.e. the total absolute stored charge density $Q_M = Q_{vo}(t_P)$, at the beginning of the depolarisation period ($t=t_P$). Q_M, calculated as the integral over the whole specimen thickness of the absolute value of the charge density measured at $t=t_P$, divided by the thickness itself, eq. (4.3), provides a measure of the grey area of Fig. 4.16. This parameter has the dimension of a charge volume density (C/m^3). If the purpose is to compare different materials, the time t_P must be kept constant for each material, because Q_M is a function of t_P. Actually, for DC tests Q_M is calculated considering the space charge profile recorded 2 s after depolarisation beginning, since the first profiles measured are influenced by the turning-off transient of HVDC generator. This delay time, however, does not lead to errors in evaluating the maximum stored charge since charge, in DC, is quite slow to decay during the first instants after voltage removal.

Another quantity can be extracted from the depolarisation characteristic, i.e. the slope, s. Expressing the charge measured during the volt-off in relative value to the charge measured immediately after grounding,

$$q_{VO}(t) = \frac{1}{Q_{VO}(t_P)(x_1 - x_0)} \int_{x_0}^{x_1} |Q(x,t)| dx \qquad (4.4)$$

and plotting the value calculated by eq. (4.4) as a function of time in a semi-log scale, the depolarisation characteristic is obtained, which

provides the rate of charge decay. The mean slope of this curve, s, is an useful quantity for the evaluation of electrical properties of the insulating material: the larger s, the faster is space charge depletion after field inversion, field transients or depolarisation (s is thus related to trap depth distribution and apparent charge mobility, see chapter 7). An example of depolarisation characteristic, referred to material #A, is reported in the Fig. 4.18.

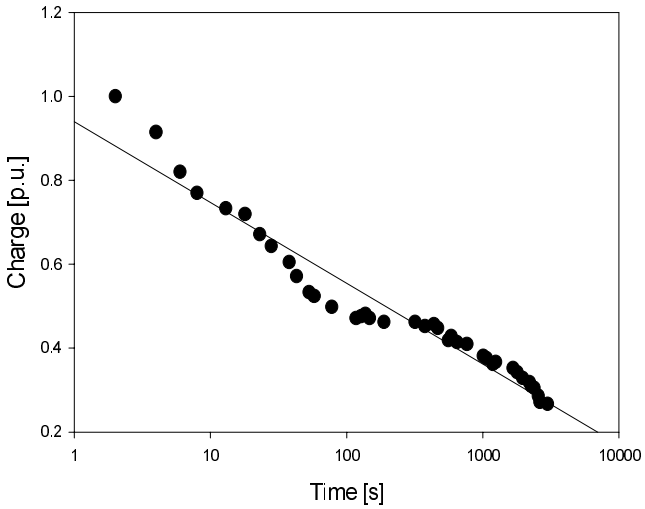

Fig. 4.18: Example of the time behaviour of the charge magnitude during volt-off, in p.u. with respect to the charge measured immediately (2s) after grounding (depolarisation characteristic). Material #A.

4.5 Partial discharge measurements

As seen in previous chapters, partial discharges are considered to be the main degradation factors due to ASD supply voltage. Therefore, PD measurements must be carried out under different conditions, varying, e.g., the kind of waveform applied (sinusoidal, square), the polarity (unipolar, bipolar) and the frequency, in order to characterise insulation endurance.

4.5.1 Experimental set-up

The measurement circuit for partial discharge detection is sketched in Fig. 4.19. The supply voltage may be either sinusoidal or square depending on which generator is connected to the measuring circuit.

Voltage generators are the same described for the life test experimental set-up: supply voltage can be varied in amplitude (0÷15000 V peak-to-peak), frequency (from 50 Hz to 10 kHz), dV/dt (from 0.5 to 80 kV/μs) and shape (sinusoidal, unipolar or bipolar square waves). Typical tested specimens consist of standard twisted pairs, the same used for life tests. The coupling capacitor, C_C, is PD-free and has capacitance of 100 pF. The specimen under test is connected with a 50 Ω resistance, specifically designed to be used with high-frequency signals, to the PD detection system [87-90].

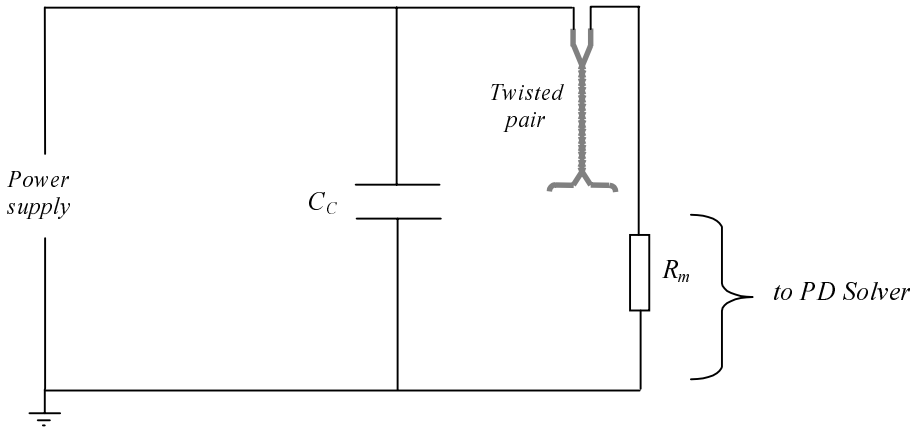

Fig. 4.19: Measurement circuit for PD detection on twisted pairs.

Partial discharges were measured by means of TechImp PDSolver system, which enables partial discharge pulses to be recorded and processed digitally, collecting a large number of pulses and allowing separation and identification tools, based on artificial intelligence and statistical processing, to be implemented [91-96].

A block scheme of the PD solver test system is reported in Fig. 4.20: the PD signal coming from the measuring resistor is conditioned before entering the PD measurement system. Very large spikes, in fact, affect PD signal under high frequency square wave supply, disturbing PD pulse acquisition, due to steep rise fronts and fast commutations of the power supply. Therefore, an appropriate high-pass filter was inserted between measuring resistor and PD Solver input, thus attenuating spikes without affecting significantly PD signals which have a frequency spectrum higher than that relevant to spikes.

PD Solver system is based on a waveform analyser (remote-controlled by PC through an IEEE-488 bus), which provides a triggerable partitioned on-line memory buffer (8 MB), a large bandwidth (0-1 GHz)

and fast sampling rate (up to 2 Gsa/s). The waveform analyser sensitivity ranges from 2 mV/div to 10 V/div. A synchronisation block is implemented in order to achieve a line or external synchronisation on applied voltage.

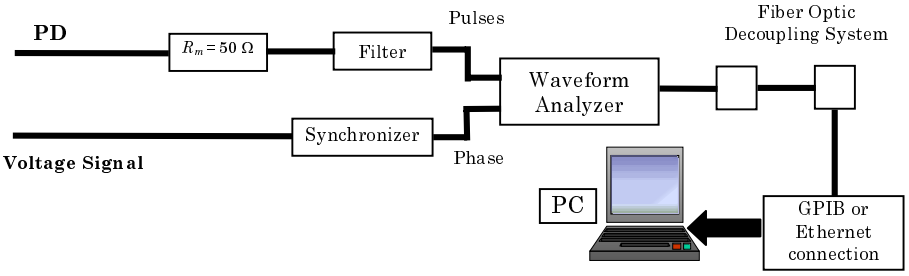

Fig. 4.20: Scheme of PD Solver testing apparatus.

4.5.2 Data acquisition and processing

The acquisition software enables a full remote control of the waveform analyser. Thus, the operator can set all the acquisition parameters (such as time base, volt/division, sampling rate, trigger level and more) taking advantage of a user friendly interface, which is shown in Fig. 4.21A.

The main feature of PD Solver acquisition system is the capability to record the entire PD pulse and not only its amplitude and phase, as it occurs usually with other commercial PD detectors. This can allow to obtain a huge amount of information which can be processed through neuro-fuzzy framework and statistic tools. This procedure classifies pulses according to their shape in order to identify and localise the defects generating PD.

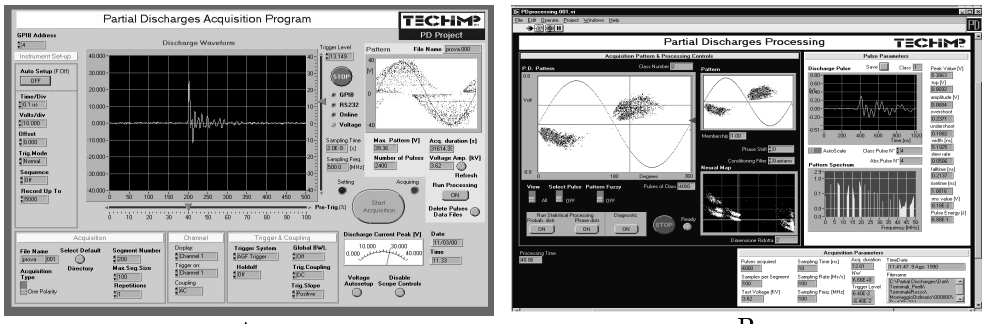

A B

Fig. 4.21: Acquisition (A) and processing (B) software user interfaces.

The instrument is able to memorise a huge amount of PD pulses during the acquisition, in order to have a data set large enough for statistical processing. After that, all these information can be processed by means of a specific software, whose user interface is shown in Fig. 4.20B: separation and classification of the PD signals are performed, resorting to PD pulse shape analysis, through a fuzzy classifier.

The fuzzy classifier mainly consists of two fundamental blocks: feature extractor and feature classifier. The feature extractor provides a mapping of the recorded pulses. The feature classifier builds a certain number of clusters, according to this map, through a fuzzy clustering algorithm that assigns to each vector of the map a membership degree [93-94]. In such a way a classification of PD pulses into clusters is carried out. Each cluster is characterised by homogeneous features of PD-pulse shape. The software, then, allows any visualisation and processing for each class to be performed. The homogeneous subsets of the acquired data are, in such a way, available for any further investigation (e.g., stochastic analysis). In particular, fuzzy classification can provide a second tool (besides the high-pass filter) for noise filtering due to square wave supply. One of the classes thus obtained is, in fact, formed by pulses generated by displacement current peaks at each voltage commutation. The system will recognise and reject this pulse class.

For each class, PD pulse amplitude vs. phase of occurrence can be collected in a phase-resolved PD pattern (PRPD pattern). This pattern provides information about the PD distribution in relation to the supply waveform, a fundamental tool for the analysis and recognition of discharge mechanisms. The fuzzy-classification approach has the purpose to enable the evaluation of simultaneous PD phenomena when 3D patterns do not permit any visible clustering to be observed and even the statistical processing is unable to separate PD phenomena.

The processing software can show each recorded pulse, highlighting its co-ordinates in the pattern and provides the most important features of each pulse (rise time, pulse width, spectral density and others). A statistical analysis (of amplitude and phase distributions) can be carried out on the acquired data-set.

The statistical processing consists of the application of the two parameter Weibull function to the whole set of PD height values, as well as to each single class provided by the fuzzy net. The two parameter Weibull distribution of PD pulse heights is given by the following expression, the same used for life test failure time processing [95]:

$$F(q) = 1 - \exp\left[-\left(\frac{q}{\alpha} \right)^{\beta} \right] \tag{4.5}$$

where q is pulse charge height, α e β are scale and shape parameters.

The pulse phase distribution is treated through 2nd, 3rd and 4th order moment evaluation. The estimation of β is particularly significant for PD identification purpose. It has been shown, in fact, that the shape parameter of the Weibull function, being associated with the dispersion of PD pulse height sequences, is characteristic of a given PD phenomenon, i.e. of the source generating PD pulse trains [95]. For example, values of $\beta<2$ indicate surface discharges, while $2<\beta<7$ is characteristic of internal discharges. Corona discharges provide very large β values.

4.5.3 Test procedures

A test procedure was established in order to evaluate the quality of the four kinds of enamelled wires under test.

First of all, ramp tests were carried out in order to detect the PD inception voltage (PDIV), analysing the behaviour of PDIV with frequency and with kind of supply waveform used. For this purpose, PDIV was measured for each specimen under test at 50 Hz, with both sinusoidal and square waves (unipolar and bipolar), at 1 kHz and 10 kHz with unipolar and bipolar square waves, increasing progressively the voltage amplitude until PD activity was observed (the rise time for the square waves was about 200 ns).

PD activity was observed under square waves at different frequencies (from 1 Hz to 10 kHz) at voltage levels close to PDIV, in order to single out the effect of frequency on some PD features, e.g. PD amplitude, phase and repetition rate.

Then, PD activity was measured at higher voltage levels, i.e. 1.5 and 2 PDIV in order to investigate the evolution of PD phenomena *versus* applied voltage according to the procedure reported in the Fig. 4.22.

A few quantities, from the huge amount of data coming from PD measurements, are used in the following as indicators for PD activity, i.e. the inception voltage PDIV, the PD mean amplitude, the PD repetition rate and the shape parameter, β, of Weibull distribution of pulse heights.

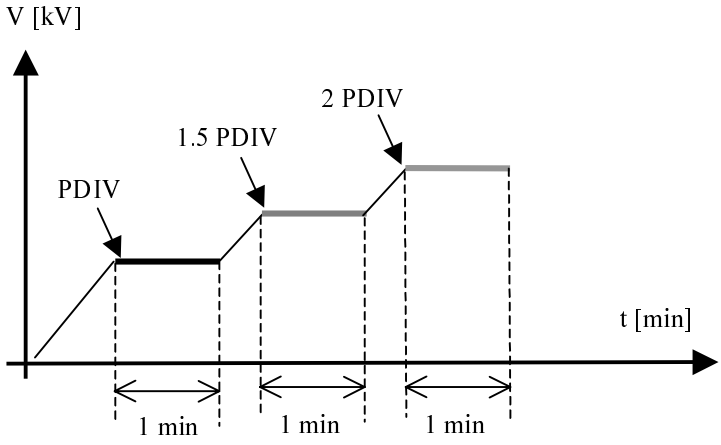

Fig. 4.22: Scheme of test procedure (ramp and constant stress).

Chapter 5

Life test results

5.1 Premise

This chapter collects the results of life tests performed on four kinds of enamelled wires, one conventional, #A, and three insulated with different corona resistant materials, #B, #C and #D, according to life test procedures described in the previous chapter.

In order to investigate the effect of partial discharges on ageing acceleration and their magnification with frequency, hypothesised in literature, life tests were performed in the presence and in the absence of PD. This was obtained using two different media surrounding specimens, that is, air and silicon oil, respectively. For this purpose the PDIV of each kind of enamelled wire was measured in oil and in air with the different kinds of voltage waveform used.

Life tests were performed under 50 Hz sinusoid, as a reference for the other tests, under 10 kHz sinusoid, to investigate the effect of frequency on ageing, under 10 kHz bipolar and unipolar square waveforms in order to reproduce the voltage waveform characterising the turn-to-turn and the phase-to-phase voltage of a motor.

In the following, life test results are shown for each material and test waveform summarising in tables the voltage level (peak-to-peak and rms), the value of the scale parameter, α, of the Weibull failure time distribution, with the relevant confidence intervals, and the shape parameter, β. The relevant Weibull plot is reported, moreover, for most tests.

5.2 Life test results

Material #A: 50 Hz sinusoidal waveform

1) In the presence of PD (air)

Test	V_{PP} [kV]	V_{rms} [kV]	α_{min} [h]	α [h]	α_{max} [h]	β
1A	12.4	4.4	1.4	7.9	11.3	1.4
1B	15.5	5.5	2.3	4.1	6.7	5.8
1C	18.7	6.6	0.57	0.9	1.6	5.2
1D	21.8	7.7	0.12	0.25	0.35	1.4

2) In the absence of PD (oil)

Test	V_{PP} [kV]	V_{rms} [kV]	α_{min} [h]	α [h]	α_{max} [h]	β
2A	18.7	6.6	23	47	63	0.9
2B	21.8	7.7	3.0	5.2	7.7	0.6
2C	24.9	8.8	0.97	1.8	3.5	0.7

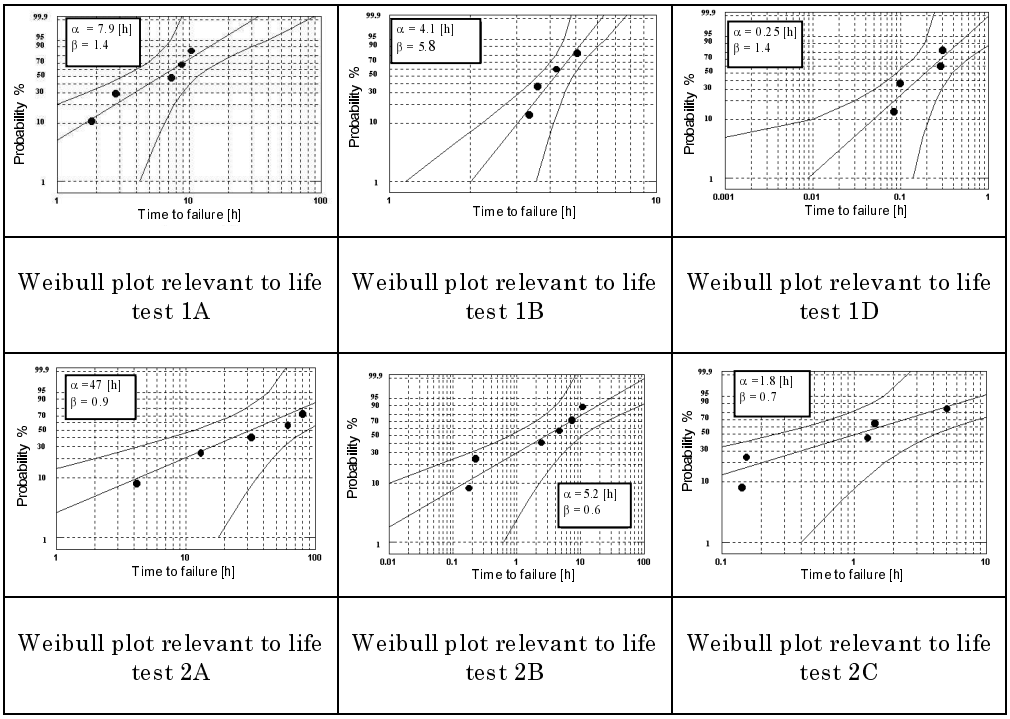

Fig. 5.1: Weibull plot relevant to 50 Hz sinusoidal life tests in air and in silicon oil for material #A.

Material #B: 50 Hz sinusoidal waveform

3) In the presence of PD (air)

Test	V_{PP} [kV]	V_{rms} [kV]	α_{min} [h]	α [h]	α_{max} [h]	β
3A	12.4	4.4	1.4	2.4	4.3	1.5
3B	15.5	5.5	0.28	0.43	0.64	2.2
3C	18.7	6.6	0.09	0.13	0.19	2.2

4) In the absence of PD (oil)

Test	V_{PP} [kV]	V_{rms} [kV]	α_{min} [h]	α [h]	α_{max} [h]	β
4A	15.5	5.5	44	75	130	1.6
4B	18.7	6.6	9.5	13	18	2.8
4C	21.8	7.7	1.0	2.8	7.7	0.9

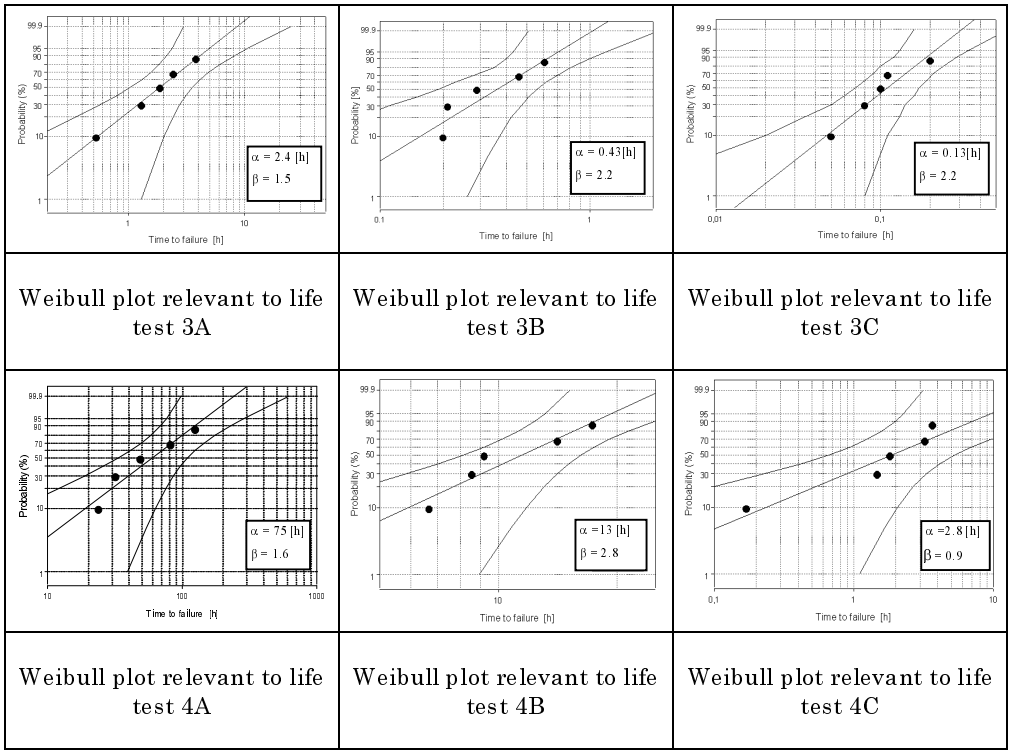

Weibull plot relevant to life test 3A	Weibull plot relevant to life test 3B	Weibull plot relevant to life test 3C
Weibull plot relevant to life test 4A	Weibull plot relevant to life test 4B	Weibull plot relevant to life test 4C

Fig. 5.2: Weibull plot relevant to 50 Hz sinusoidal life tests in air and in silicon oil for material #B.

Material #C: 50 Hz sinusoidal waveform

5) In the presence of PD (air)

Test	V_{PP} [kV]	V_{rms} [kV]	α_{min} [h]	α [h]	α_{max} [h]	β
5A	12.4	4.4	37	73	150	1.3
5B	15.5	5.5	2.2	8.7	34	0.7
5C	18.7	6.6	0.4	1.0	2.8	0.9

6) In the absence of PD (oil)

Test	V_{PP} [kV]	V_{rms} [kV]	α_{min} [h]	α [h]	α_{max} [h]	β
6A	17.0	6.0	53	107	210	1.3
6B	18.7	6.6	24	28	33	5.1
6C	21.8	7.7	5.6	8.8	14	2.2

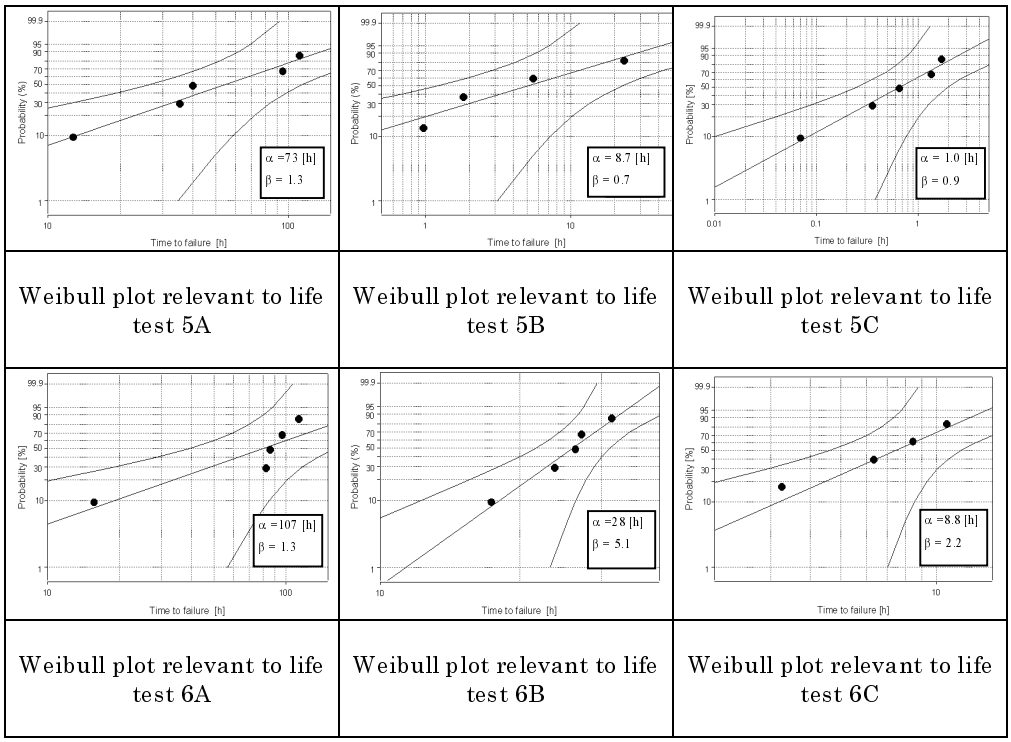

Weibull plot relevant to life test 5A	Weibull plot relevant to life test 5B	Weibull plot relevant to life test 5C
Weibull plot relevant to life test 6A	Weibull plot relevant to life test 6B	Weibull plot relevant to life test 6C

Fig. 5.3: Weibull plot relevant to 50 Hz sinusoidal life tests in air and in silicon oil for material #C.

Material #D: 50 Hz sinusoidal waveform

7) In the presence of PD (air)

Test	V_{PP} [kV]	V_{rms} [kV]	α_{min} [h]	α [h]	α_{max} [h]	β
7A	12.4	4.4	1.6	1.9	2.3	4.7
7B	15.5	5.5	0.5	0.65	0.8	3.7
7C	18.7	6.6	0.1	0.16	0.33	1.2

8) In the absence of PD (oil)

Test	V_{PP} [kV]	V_{rms} [kV]	α_{min} [h]	α [h]	α_{max} [h]	β
8A	17.0	6.0	8.4	14	24	1.7
8B	18.7	6.6	4.7	8.8	16	1.5
8C	21.8	7.7	0.44	1.3	4.0	0.8

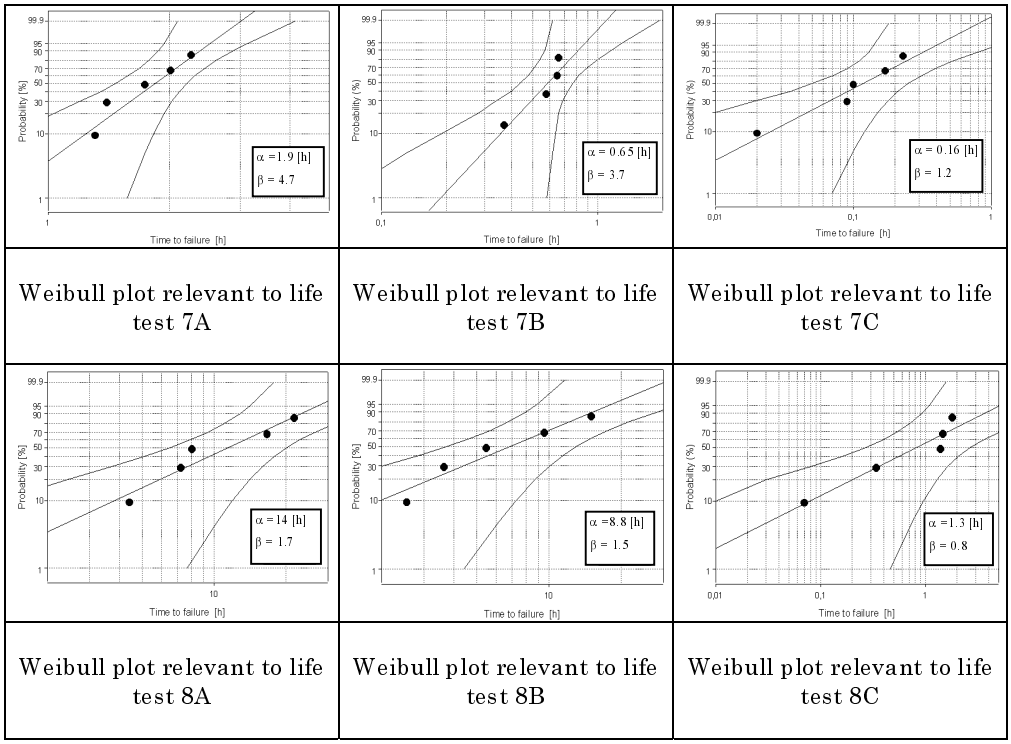

Weibull plot relevant to life test 7A | Weibull plot relevant to life test 7B | Weibull plot relevant to life test 7C

Weibull plot relevant to life test 8A | Weibull plot relevant to life test 8B | Weibull plot relevant to life test 8C

Fig. 5.4: Weibull plot relevant to 50 Hz sinusoidal life tests in air and in silicon oil for material #D.

Material #A: 10 kHz sinusoidal waveform

9) In the presence of PD (air)

Test	V_{PP} [kV]	V_{rms} [kV]	α_{min} [h]	α [h]	α_{max} [h]	β
9A	3.1	1.1	0.9	1.5	2.5	6.2
9B	4.2	1.5	0.4	0.85	1.2	4.4
9C	5.1	1.8	0.08	0.30	0.51	4.6
9D	5.6	2.0	0.05	0.14	0.21	6.5

10) In the absence of PD (oil)

Test	V_{PP} [kV]	V_{rms} [kV]	α_{min} [h]	α [h]	α_{max} [h]	β
10A	9.0	3.2	64	90	114	1.7
10B	15.5	5.5	0.44	1.6	3.6	1.4
10C	18.4	6.5	0.03	0.15	0.66	0.6

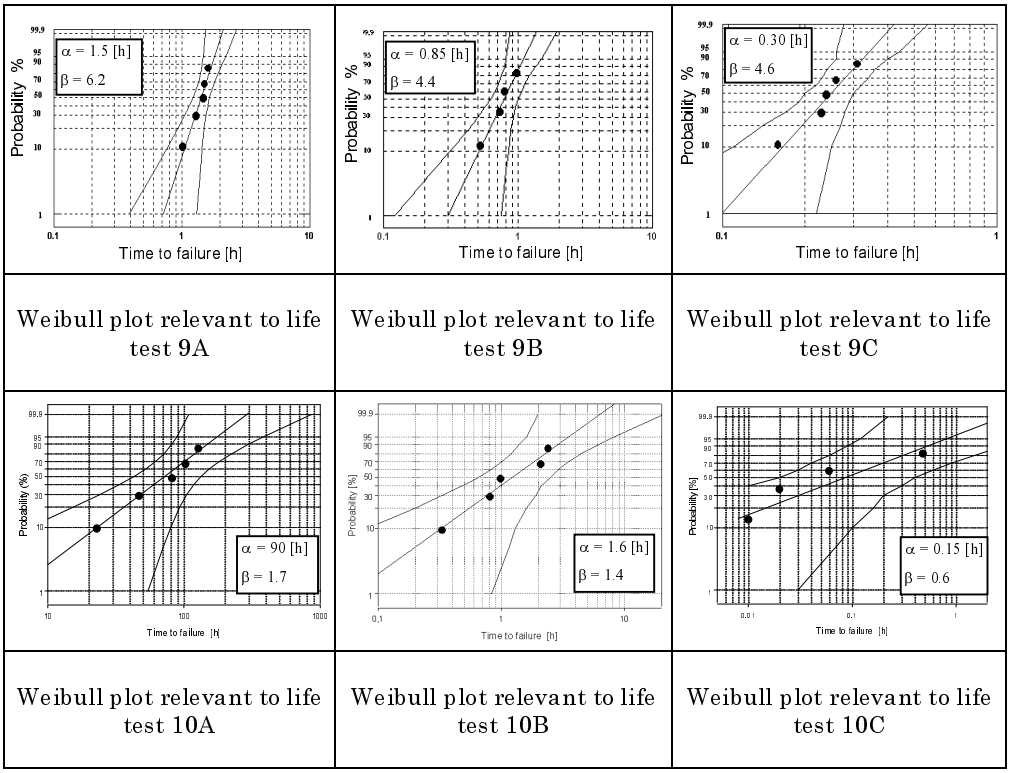

Weibull plot relevant to life test 9A	Weibull plot relevant to life test 9B	Weibull plot relevant to life test 9C
Weibull plot relevant to life test 10A	Weibull plot relevant to life test 10B	Weibull plot relevant to life test 10C

Fig. 5.5: Weibull plot relevant to 10 kHz sinusoidal life tests in air and in silicon oil for material #A.

Material #B: 10 kHz sinusoidal waveform

11) In the presence of PD (air)

Test	V_{PP} [kV]	V_{rms} [kV]	α_{min} [h]	α [h]	α_{max} [h]	β
11A	3.7	1.3	97	98	99	18
11B	4.5	1.6	49	53	57	12
11C	4.9	1.75	9.2	19	39	1.2
11D	5.7	2.0	1.7	3.2	6.0	1.4

12) In the absence of PD (oil)

Test	V_{PP} [kV]	V_{rms} [kV]	α_{min} [h]	α [h]	α_{max} [h]	β
12A	9.0	3.2	56	115	229	1.2
12B	12.4	4.4	5.2	12	36.4	0.9
12C	15.5	5.5	1.4	2.2	4.3	1.6

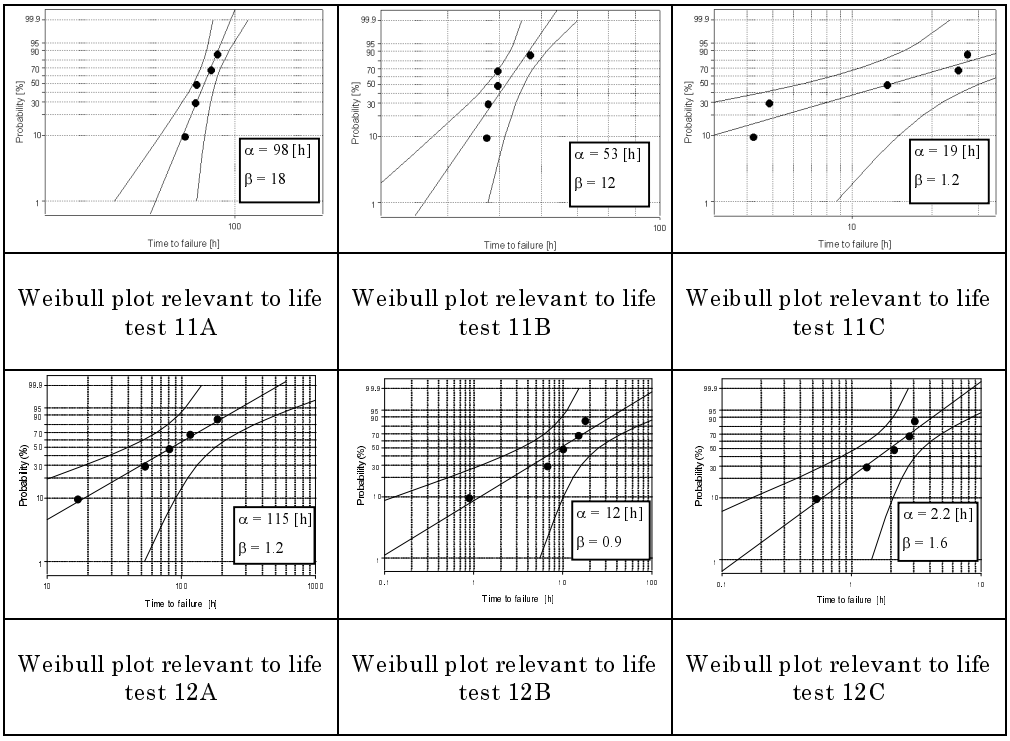

Weibull plot relevant to life test 11A	Weibull plot relevant to life test 11B	Weibull plot relevant to life test 11C
Weibull plot relevant to life test 12A	Weibull plot relevant to life test 12B	Weibull plot relevant to life test 12C

Fig. 5.6: Weibull plot relevant to 10 kHz sinusoidal life tests in air and in silicon oil for material #B.

Material #C: 10 kHz sinusoidal waveform

13) In the presence of PD (air)

Test	V_{PP} [kV]	V_{rms} [kV]	α_{min} [h]	α [h]	α_{max} [h]	β
13A	3.7	1.3	50	62	76	4.2
13B	4.2	1.5	29	40	57	2.6
13C	5.1	1.8	1.0	1.6	2.5	2.0
13D	5.6	2.0	0.5	0.54	0.59	12

14) In the absence of PD (oil)

Test	V_{PP} [kV]	V_{rms} [kV]	α_{min} [h]	α [h]	α_{max} [h]	β
14A	9.0	3.2	306	518	816	1.8
14B	12.4	4.4	42	64	109	1.8
14C	15.5	5.5	1.7	2.7	4.6	1.7

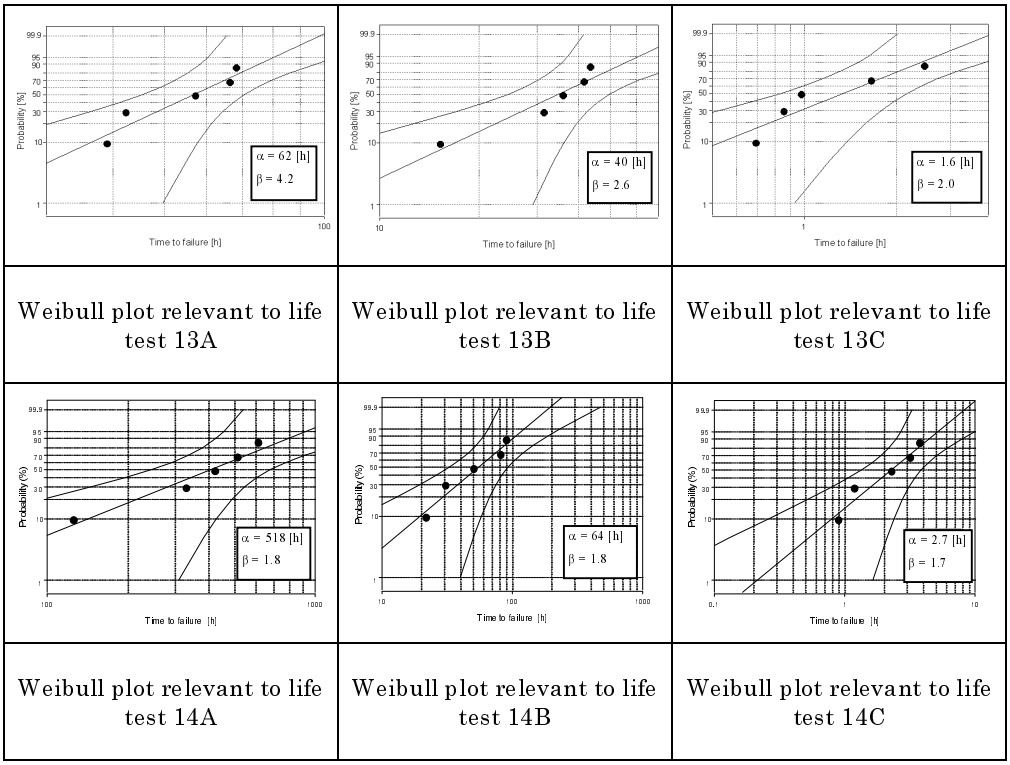

Weibull plot relevant to life test 13A	Weibull plot relevant to life test 13B	Weibull plot relevant to life test 13C
Weibull plot relevant to life test 14A	Weibull plot relevant to life test 14B	Weibull plot relevant to life test 14C

Fig. 5.7: Weibull plot relevant to 10 kHz sinusoidal life tests in air and in silicon oil for material #C.

Material #D: 10 kHz sinusoidal waveform

15) In the presence of PD (air)

Test	V_{PP} [kV]	V_{rms} [kV]	α_{min} [h]	α [h]	α_{max} [h]	β
15A	3.1	1.1	2.3	3.0	4.1	3.1
15B	3.7	1.3	0.9	1.2	1.6	3.1
15C	4.2	1.5	0.41	0.54	0.69	3.4

16) In the absence of PD (oil)

Test	V_{PP} [kV]	V_{rms} [kV]	α_{min} [h]	α [h]	α_{max} [h]	β
16A	9.0	3.2	52	64	88	3.3
16B	12.4	4.4	2.8	6.5	14	1.1
16C	15.5	5.5	0.41	0.84	1.8	1.3

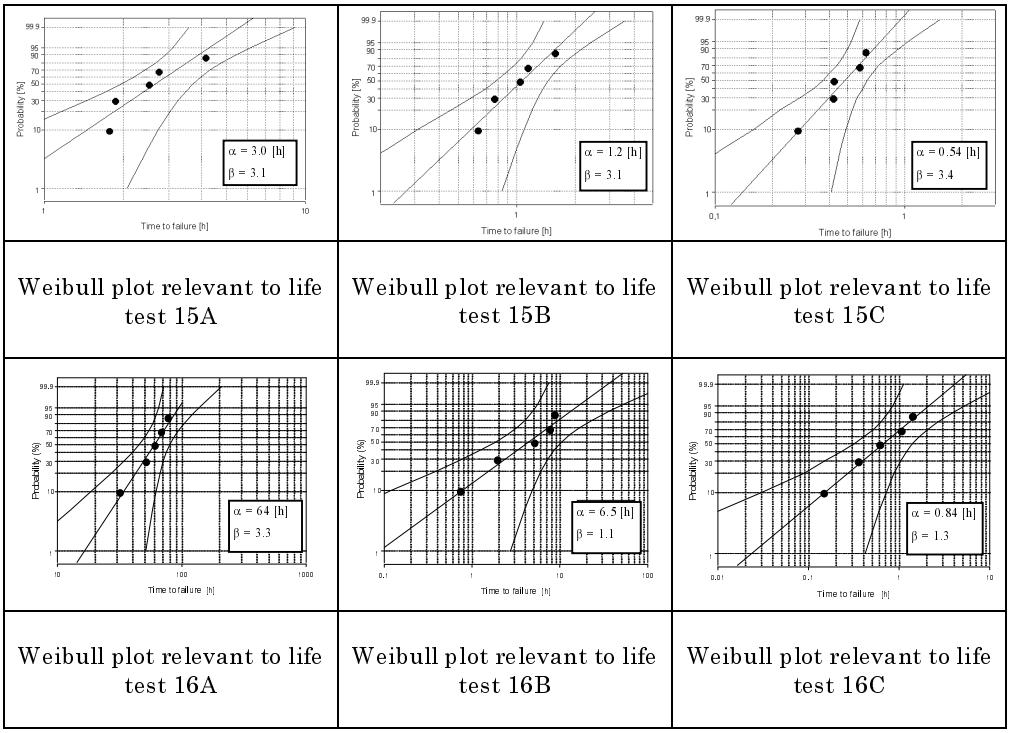

Weibull plot relevant to life test 15A	Weibull plot relevant to life test 15B	Weibull plot relevant to life test 15C
Weibull plot relevant to life test 16A	Weibull plot relevant to life test 16B	Weibull plot relevant to life test 16C

Fig. 5.8: Weibull plot relevant to 10 kHz sinusoidal life tests in air and in silicon oil for material #D.

Material #A: 10 kHz square waveform, in the presence of PD (air)

17) Unipolar

Test	V_{PP} [kV]	V_{rms} [kV]	α_{min} [h]	α [h]	α_{max} [h]	β
17A	1.8	1.3	8.1	14	21.1	5.3
17B	2.5	1.8	2.3	3.5	5.7	4.2
17C	3.0	2.1	1.1	2.2	4.2	6.0

18) Bipolar

Test	V_{PP} [kV]	V_{rms} [kV]	α_{min} [h]	α [h]	α_{max} [h]	β
18A	2.2	1.1	2.8	3.5	4.5	4.8
18B	2.4	1.2	2.4	2.8	3.7	4.0
18C	3.0	1.5	1.4	1.8	2.0	9.7
18D	4.0	2.0	0.9	1.1	1.4	8.5

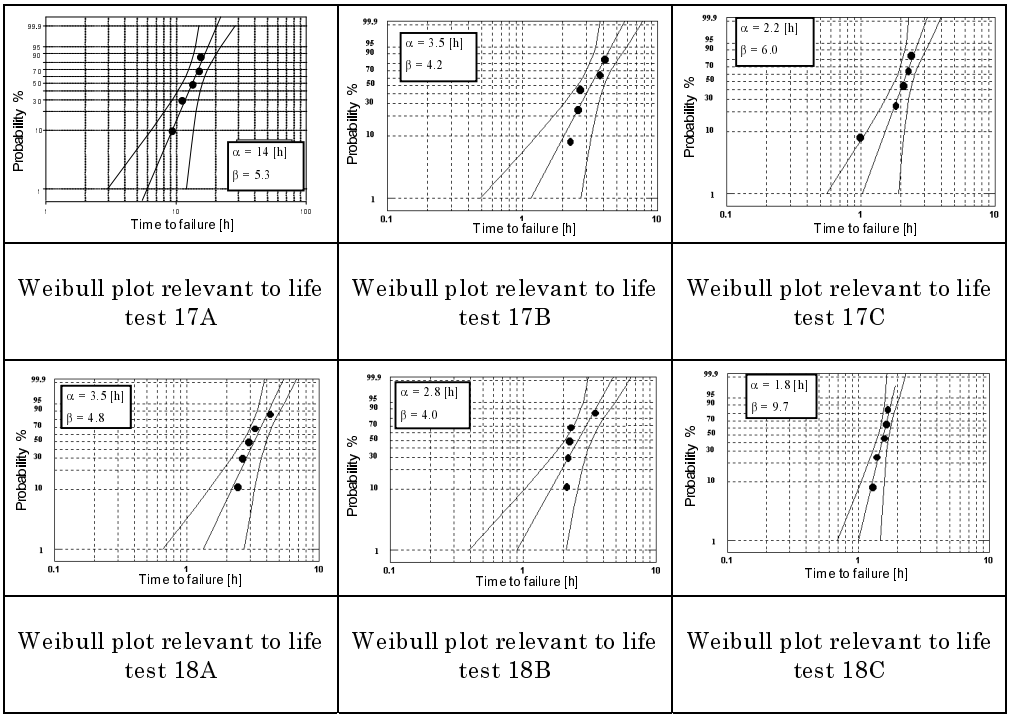

Weibull plot relevant to life test 17A | Weibull plot relevant to life test 17B | Weibull plot relevant to life test 17C

Weibull plot relevant to life test 18A | Weibull plot relevant to life test 18B | Weibull plot relevant to life test 18C

Fig. 5.9: Weibull plot relevant to 10 kHz squarewave life tests in air for material #A.

Material #B: 10 kHz square waveform, in the presence of PD (air)

19) Unipolar

Test	V_{PP} [kV]	V_{rms} [kV]	α_{min} [h]	α [h]	α_{max} [h]	β
19A	2.2	1.5	880	1100	2700	2.4
19B	3.0	2.1	270	300	340	8.1
19C	3.5	2.5	113	116	120	33

20) Bipolar

Test	V_{PP} [kV]	V_{rms} [kV]	α_{min} [h]	α [h]	α_{max} [h]	β
20A	4.0	2.0	31	45	61	9.8
20B	3.5	1.75	76	96	115	9.6
20C	3.0	1.5	167	210	256	5.9

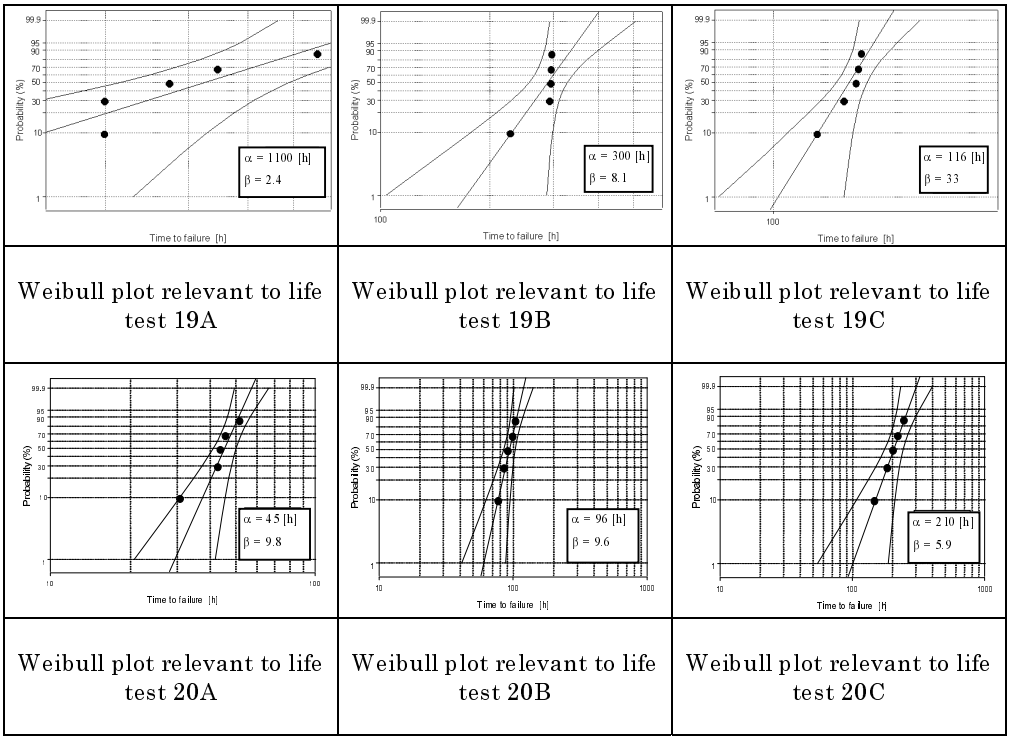

Weibull plot relevant to life test 19A	Weibull plot relevant to life test 19B	Weibull plot relevant to life test 19C
Weibull plot relevant to life test 20A	Weibull plot relevant to life test 20B	Weibull plot relevant to life test 20C

Fig. 5.10: Weibull plot relevant to 10 kHz squarewave life tests in air for material #B.

Material #C: 10 kHz square waveform, in the presence of PD (air)

21) Unipolar

Test	V_{PP} [kV]	V_{rms} [kV]	α_{min} [h]	α [h]	α_{max} [h]	β
21A	2.2	1.5	480	520	580	11
21B	3.0	2.1	78	89	102	7.0
21C	3.5	2.5	20	23	27	5.9

22) Bipolar

Test	V_{PP} [kV]	V_{rms} [kV]	α_{min} [h]	α [h]	α_{max} [h]	β
22A	3.5	1.75	51	52	54	24
22B	4.0	2.0	3.0	5.5	10	1.5
22C	5.0	2.5	1.2	1.4	1.7	5.0

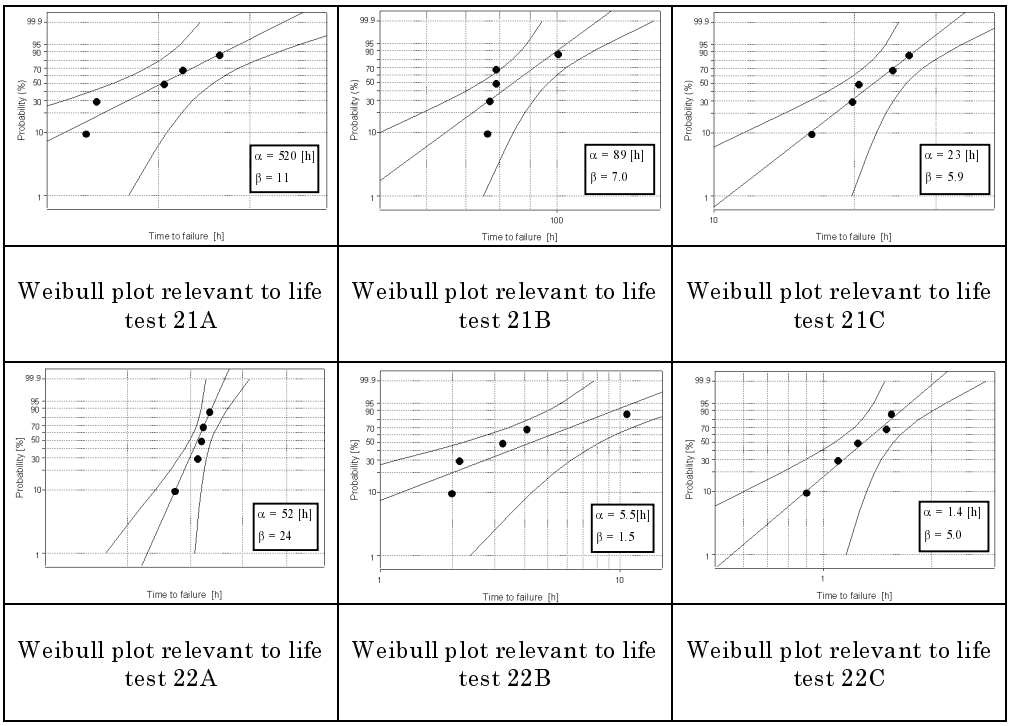

Weibull plot relevant to life test 21A	Weibull plot relevant to life test 21B	Weibull plot relevant to life test 21C
Weibull plot relevant to life test 22A	Weibull plot relevant to life test 22B	Weibull plot relevant to life test 22C

Fig. 5.11: Weibull plot relevant to 10 kHz squarewave life tests in air for material #C.

Material #D: 10 kHz square waveform, in the presence of PD (air)

23) Unipolar

Test	V_{PP} [kV]	V_{rms} [kV]	α_{min} [h]	α [h]	α_{max} [h]	β
23A	1.8	1.3	20	22	24	10
23B	2.2	1.5	5.0	7.9	12	1.9
23C	3.0	2.1	2.4	2.9	3.6	4.5

24) Bipolar

Test	V_{PP} [kV]	V_{rms} [kV]	α_{min} [h]	α [h]	α_{max} [h]	β
24A	2.5	1.25	3.5	5.7	9.2	1.8
24B	3.0	1.5	2.1	3.6	5.5	1.9
24C	4.0	2.0	1.1	1.2	1.3	9.5

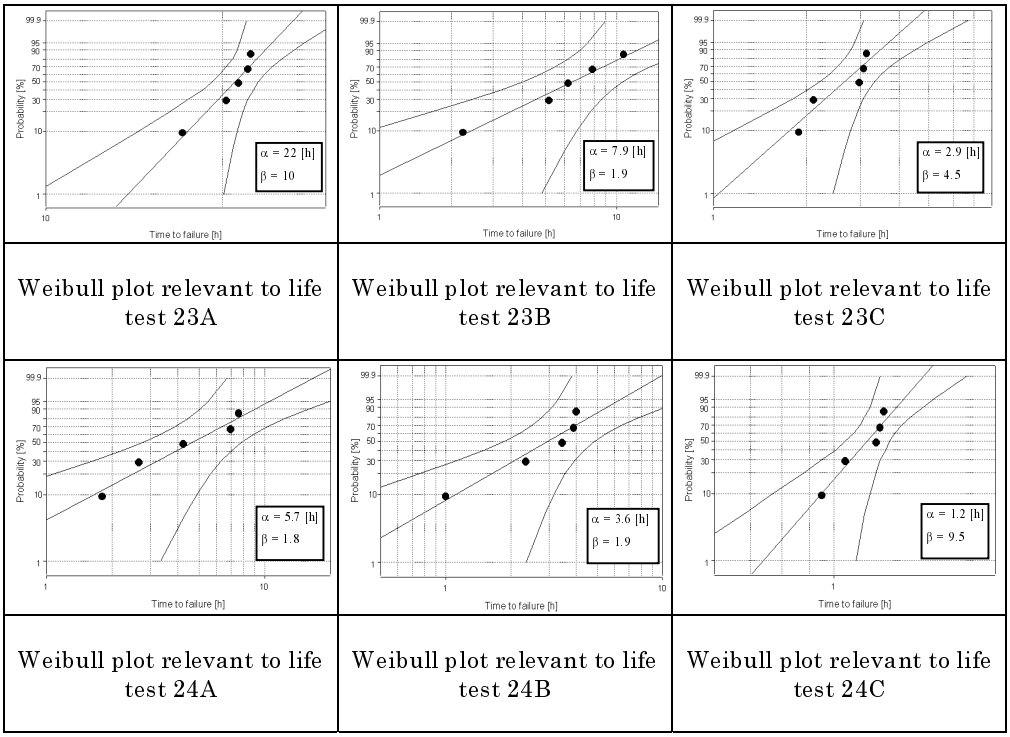

Weibull plot relevant to life test 23A | Weibull plot relevant to life test 23B | Weibull plot relevant to life test 23C

Weibull plot relevant to life test 24A | Weibull plot relevant to life test 24B | Weibull plot relevant to life test 24C

Fig. 5.12: Weibull plot relevant to 10 kHz squarewave life tests in air for material #D.

5.3 Discussion on life test results

A comparison of life performance of the four materials can be carried out. Looking at life lines relevant to tests with 50 Hz sinusoidal wave in the absence of PD (Fig. 5.13), one can see that conventional material, #A, exhibits the best life performance, i.e. longer failure times and larger endurance coefficient (11.7). Corona resistant (CR) materials show a contrasting behaviour. The life times relevant to #C are close to those of #A, even if the endurance coefficient is slightly smaller (10.2). Material #B and #D, on the contrary, provide shorter failure times, reduced of about 1/4 and 1/10, respectively, with respect to those relevant to #A at the same rms voltage level, and smaller endurance coefficients.

This behaviour can be due to different causes, from the presence of fillers not well attached to the matrix (see the SEM observation in Fig. 4.1) in some of the CR materials, to the quality of the manufacturing process and the macrointerfaces between the different material layers that constitute CR wire insulation.

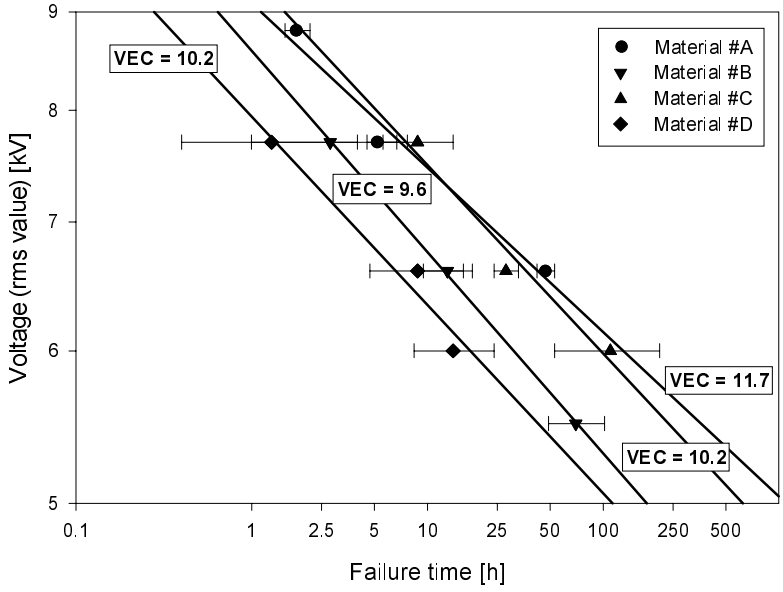

Fig. 5.13: Results and life lines for tests performed in oil at 50 Hz on the four tested materials. The VEC are also indicated.

CR materials should exhibit longer life when partial discharge are active. Comparing life test results at 50 Hz sinusoidal wave under PD

regime (Fig. 5.14), two different behaviours can be observed. Material #C provides failure times much longer than #A and endurance coefficient considerably larger. Moreover, the large VEC shown by #C would ensure longer failure times, especially going towards the design field (low voltage on Fig. 5.14). On the contrary, the other two remaining corona resistant materials (#B, #D) show significantly shorter failure times, even with respect to #A, as occurs also in the absence of PD. Voltage endurance coefficients are also reduced with respect to the absence of PD and comparable to that of #A.

This behaviour may be explained in the framework discussed above, regarding failure in the absence of PD, thinking that, in the presence of PD, functionality of CR materials is affected by contrasting phenomena: the weakness caused by interfaces (fillers to matrix, layer to layer) and the increased PD resistance due to inorganic filler properties. Breakdown times result from these features, and may increase or decrease (with respect to the conventional material) depending on which feature is prevailing.

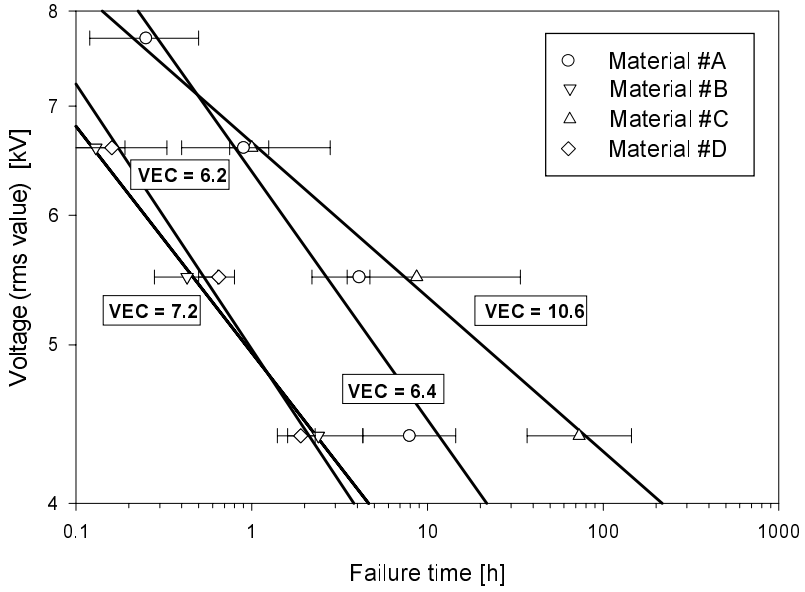

Fig. 5.14: Results and life lines for tests performed in air at 50 Hz on the four tested materials. The VEC are also indicated.

CR materials exhibit, nevertheless, a better life performance at high frequency and in the presence of PD, as can be seen by Figs. 5.15 and 5.16, where life lines under sinusoidal regime (Fig. 5.15), square unipolar and bipolar (Fig. 5.16), at 10 kHz frequency, are plotted.

Material #C presents a large endurance coefficient, especially with bipolar waveforms (for sinusoidal and square waves is 12.6 and 10.5, respectively), even better than at 50 Hz. Specimens #B show also long failure times (especially at high voltages) and quite large endurance coefficient.

Material #D, even if designed to withstand high frequency pulses, provides failure times slightly longer than those relevant to #A, but much shorter than those of #B and #C. The endurance coefficient of #D, compared with that relevant to #A, is slightly larger for sinusoidal waveforms (5.5 and 4.2 for #D and #A, respectively) and for bipolar square wave (3.4 and 1.9 for #D and #A, respectively), while it is almost the same (4.2 and 3.7 for #D and #A, respectively) for unipolar square waveforms.

Conventional material, #A, is confirmed to be the worst material at 10 kHz, due to its poor resistance to PD activity (Figs. 5.15 and 5.16), with any kind of supply waveform, and shows life reduced of several orders of magnitude with respect to the life at 50 Hz in the absence of PD, which may be the normal operating condition in motors not controlled by power electronics. This supports the experimental evidence of loss of reliability of electrical motors insulated by conventional materials and fed by adjustable speed drives.

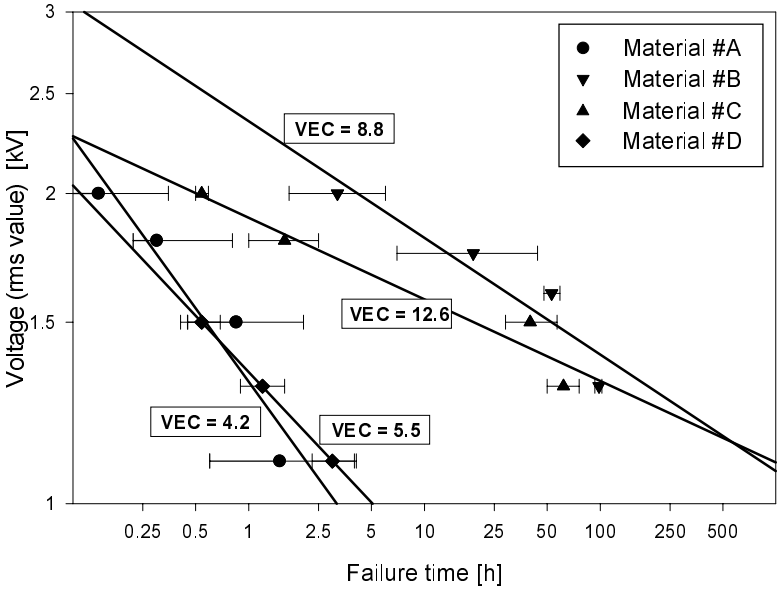

Fig. 5.15: Results and life lines for tests performed in air (under PD) at 10 kHz sinusoidal on the four tested materials. The VEC are also indicated.

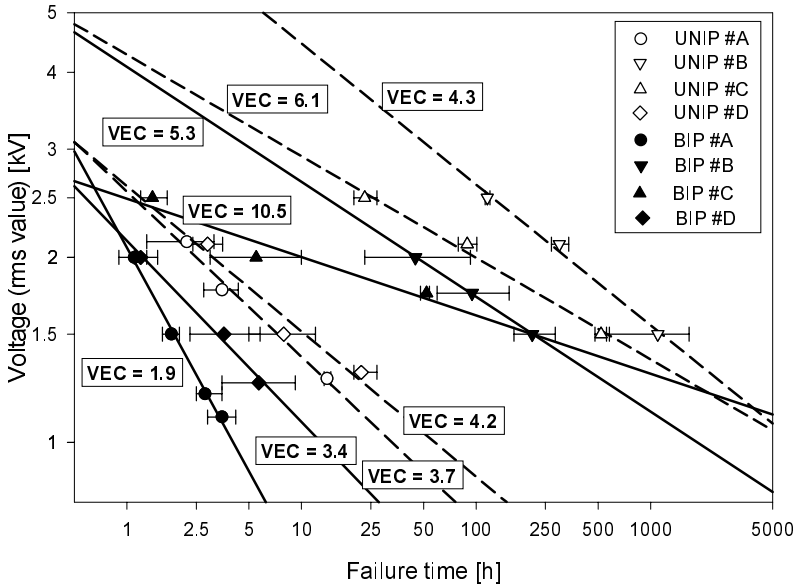

Fig. 5.16: Results and life lines for tests performed in air (under PD) at 10 kHz with unipolar (dashed lines) and bipolar (continuous lines) voltage waveforms on the four tested materials. The VEC are also indicated.

The significant improvements obtained at high frequencies under PD regime using CR materials can be addressed to the explanation given above. At high frequency the degradation (surface erosion) effect of PD is much more significant than at 50 Hz, so that the protective effect of fillers prevails with respect to interfacial problems.

Summarising, materials #A and #C perform better than #B and #D in the absence of PD, while #C seems the best when PD are active. Considering, in fact, that the voltage values used in the life tests are significantly larger than those really affecting the insulation in service, the large endurance coefficient of #C at 50 Hz and 10 kHz could provide quite long failure times even in the presence of PD at low voltage levels (typical of ASD controlled motors).

5.3.1 Partial discharge effect

Failure times relevant to the different test waveforms and conditions (presence and absence of PD) are reported in Figures 5.17-5.20 for each material as function of the peak-to-ground voltage.

Looking at the figures it comes out clearly that PD action shortens failure times significantly, of about one order of magnitude for #A and #C, even more for #B and #D The VEC value for #A is reduced

dramatically in the presence of PD, almost halved (from 11.7 to 6.5), as one would expect for an organic material in the presence of PD degradation. Similar drop can be observed also for VEC relevant to material #B (from 12 to 7.1) and for #D (from 10.2 to 6.1). The endurance coefficient relevant to #C, on the contrary, remains quite the same in the absence and in the presence of PD.

Looking at 10 kHz life lines relevant to sinusoidal tests in oil and in air, failure time and VEC decrease in the presence of PD is much more emphasised, especially for #A and #D, meaning that the larger the frequency, the more stressing becomes the effect of PD on insulation degradation.

However, frequency increase can cause degradation acceleration also in the absence of PD. It can be observed, in fact, that life and VEC decrease significantly passing from 50 Hz to 10 kHz (continuous lines in Figs. 5.17-5.20). For material #A, failure times for life tests in oil at 10 kHz are reduced, in fact, of the ratio between the frequencies with respect to failure times at 50 Hz, i.e. the failure times at 10 kHz are about 200 times shorter than at 50 Hz. The increase of dielectric and polarisation losses with frequency and, consequently, of insulation temperature as well as bulk electromechanical fatigue, may accelerate insulation degradation at 10 kHz. The small value of VEC indicates that at low voltage values life is remarkably shortened even in the absence of PD.

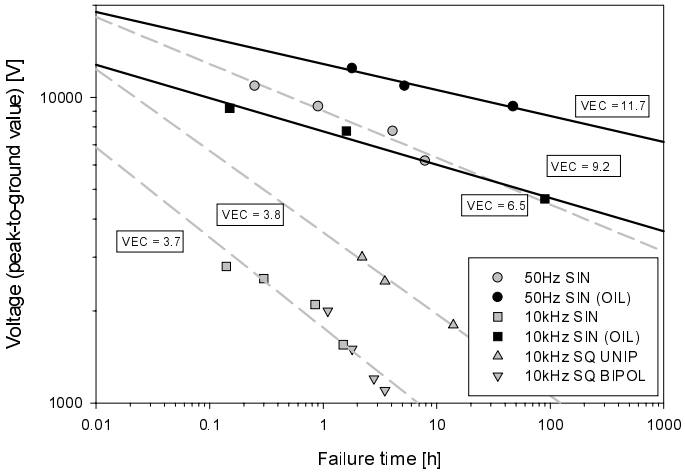

Fig. 5.17: Life test results (at probability 63.2%) and life lines as function of peak-to-ground voltage for tests performed in air and in oil with sinusoidal wave at 50 Hz and 10 kHz and for tests in air with 10 kHz square wave on material #A.

Despite of literature, that considers PD activity the only factor accelerating insulation degradation [23, 34-36, 39, 42, 44-48, 50-58, 60, 61, this important result can provide evidences that intrinsic degradation occurs also in the absence of PD but, of course, with slower rate.

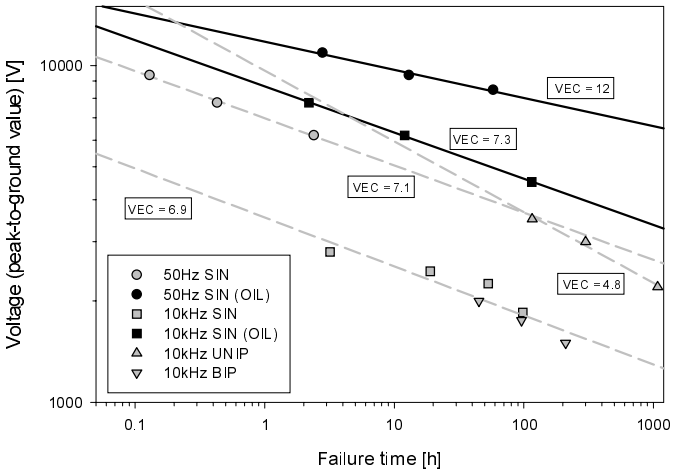

Fig. 5.18: Life test results (at probability 63.2%) and life lines as function of peak-to-ground voltage for tests performed in air and in oil with sinusoidal wave at 50 Hz and 10 kHz and for tests in air with 10 kHz square wave on material #B.

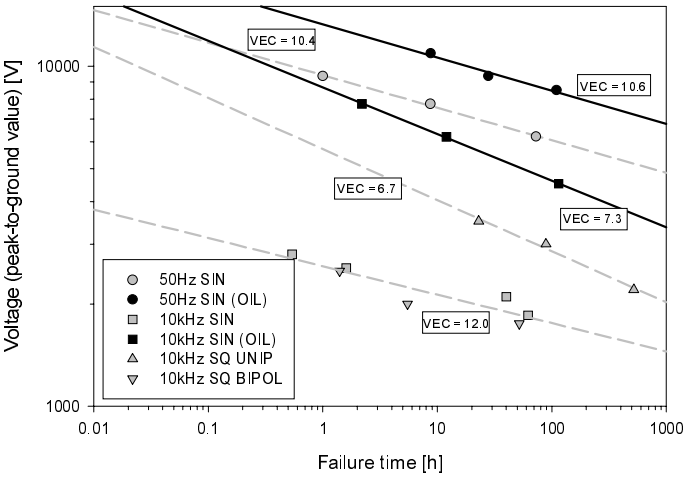

Fig. 5.19: Life test results (at probability 63.2%) and life lines as function of peak-to-ground for tests performed in air and in oil with sinusoidal wave at 50 Hz and 10 kHz and for tests in air with 10 kHz square wave on material #C.

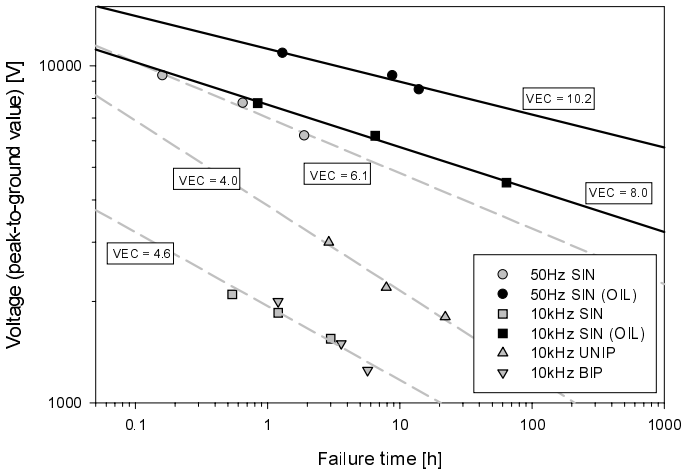

Fig. 5.20: Life test results (at probability 63.2%) and life lines as function of peak-to-ground for tests performed in air and in oil with sinusoidal wave at 50 Hz and 10 kHz and for tests in air with 10 kHz square wave on material #D.

Life reduction from 50 Hz to 10 kHz can be evaluated quantitatively by means of the following equations obtained from the experimental results:

$$L_f = L_{50}\,(f_0/f)^{\gamma} \qquad (5.1)$$

where L_f and L_{50} are the failure times at frequency f = 10 kHz and f_0 = 50 Hz, respectively. The exponent γ is experimentally estimated as 1 and 1.8 in the absence and in the presence of partial discharges, respectively, for material #A. Thus, it is further on evident that the life reduction due to frequency increase is enhanced dramatically by PD.

Moreover, it can be observed from Figs. 5.17-5.20 that experimental points relevant to life tests under PD, with high frequency bipolar waveforms, both sinusoidal and square, fit quit well the same straight line as a function of the peak-to-ground voltage, so that the effect of voltage shape (sinusoidal or square bipolar) seems to be negligible as ageing factor. Unipolar square waveforms, on the contrary, result less stressing than bipolar with the same peak-to-ground amplitude (still under PD), confirming the results provided by Kaufhold (cfr. par. 3.3) [39, 43, 45]. Failure times are, in fact, significantly longer, even if VEC value is smaller than that relevant to bipolar waves, e.g. for #B and #C.

Figure 5.21 shows the life lines for material #A with sinusoidal waveform (at 50 Hz and 10 kHz) in the absence and in the presence of

PD. It is noteworthy that decreasing voltage amplitude below PDIV in air, partial discharges extinguish; this may lead to a discontinuity of the life line, which, below the PDIV, should fit that obtained in the absence of PD (black in Fig. 5.21). In practical, a steep change of life line slope, near to PDIV, can be observed. The life line becomes almost horizontal and, thus, failure times are much longer (see the figure: the curvilinear junction lines in the figures describes the likely life behaviour of test objects both at 10 kHz and at 50 Hz). This phenomenon is not very surprising, since ageing mechanisms are noticeably different in PD regime and in the absence of PD.

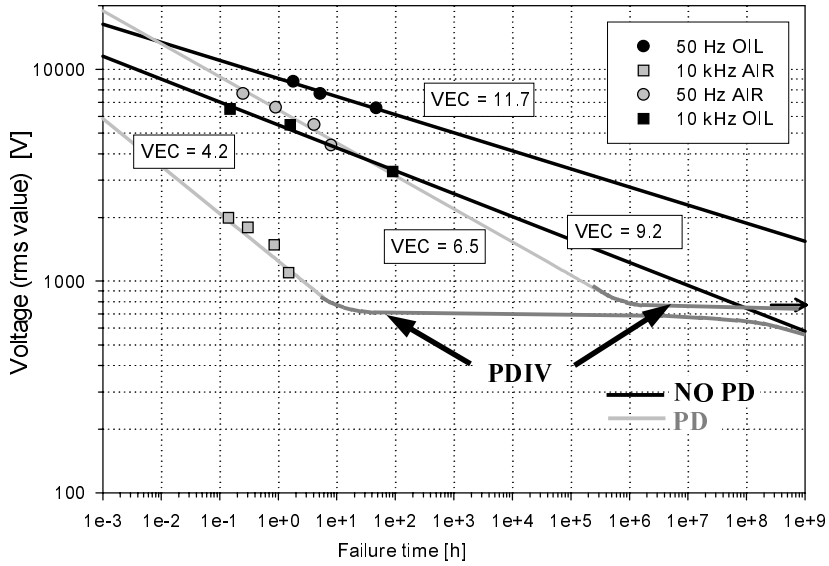

Fig. 5.21: Results and life lines as function of rms voltage for tests performed in air and in oil with sinusoidal wave at 50 Hz and 10 kHz on material #A. The life behaviour near to PDIV is showed by dark-grey curves connecting life lines in the presence (light-grey) and in the absence (black) of PD .

5.3.2 Waveform factors accelerating ageing

The voltage waveforms used for life tests can be described by means of two quantities [16-18]:

$$K_P = \frac{V_P}{V_{1P}^*} \qquad (5.2)$$

$$K_f = \lambda \frac{\sqrt{f / t_r}}{\omega_0} \qquad (5.3)$$

where V_P is the peak-to-peak value of the considered waveform, V_{1P}^* is the reference voltage; f is the switching frequency, t_r is the rise time of the considered waveform (here equal to the fall time); ω_0 = 314 rad/s; λ=2 or 2·√2 for unipolar or bipolar waveforms, respectively.

Quantity K_P, defined in (5.2), is linked to peak, whereas K_f, the parameter which takes into account the waveshape, is related to rms of the steepness of the considered waveform.

Definition (5.3) is valid for square waveforms; in sinusoidal conditions K_f is 1 and 200 for 50 Hz and 10 kHz, respectively [18].

On the basis of these quantities, a correlation analysis pointing out the most important features of the supply waveforms which affect failure times (excluding frequency) can be performed by means of multivariate regression technique.

The results of the statistical analysis are summarised in Fig. 5.22, where the main effect plot (Fig. 5.22A) and the interaction plot (Fig. 5.22B) of logarithms of the above factors are reported for material #A. The MEP gives information about the effect of each factor on accelerated degradation of a given insulating system: the steeper the line, the more stressing the effect given by the relevant factor [97, 98].

Figure 5.22A shows that the effect of peak voltage on ageing acceleration is stronger than that of waveshape (the slope of the line

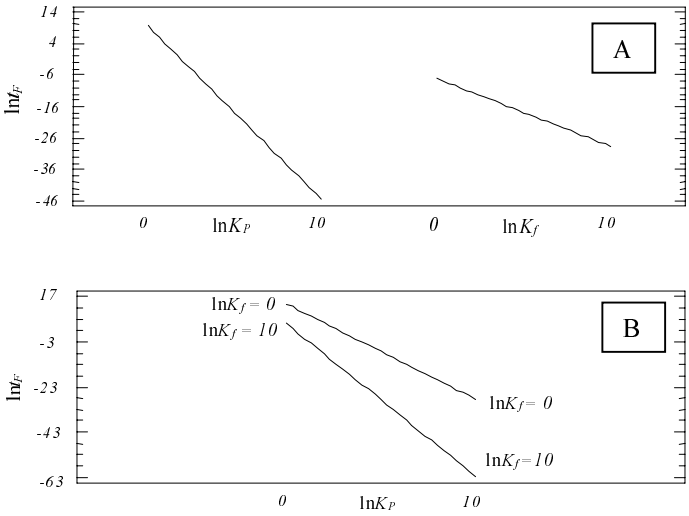

Fig. 5.22: Main Effect Plot (A) and Interaction Plot (B) relevant to the factors lnK_P and lnK_f and logarithm of time-to-failure. Material #A.

relevant to K_P factor is larger than that of K_f,), as it has been observed for capacitors-cable and low-frequency distortion [13-17]. A slight interaction could be observed in Fig. 5.22B, since the slope of $\ln t_F$ vs. $\ln K_P$ line increases with $\ln K_f$.

Therefore a second order life model can be derived:

$$\ln t_F = \ln t_{F0} - a \ln K_f - b \ln K_P - c \ln K_P \ln K_f \qquad (5.4)$$

where $t_{F0} = 1.1 \cdot 10^6$, a = 0.88, b= 4.2 and c = 0.25. The values of a, b and c confirm that the effect of K_P predominate on ageing acceleration, followed by that of K_f and by the interaction between the two factors which, however, is very small.

Since peak-to-peak voltage seems to be the main ageing factor of the voltage waveform, independently of the shape, Figs. 5.23-5.26 report all the life test results, included bipolar and unipolar square wave tests, plotted as function of peak-to-peak voltage. It can be understood that the peak-to-peak voltage is the most important parameter for life inference, since the tests performed with different waveforms at a given frequency fit quite well the same line for each material. Hence, switching frequency and peak-to-peak voltage are the main factors which describe the electrical life behaviour of these insulating materials. The slew rate seems to have a negligible effect on ageing acceleration, at least in the range of test values here considered (≤1kV/μs).

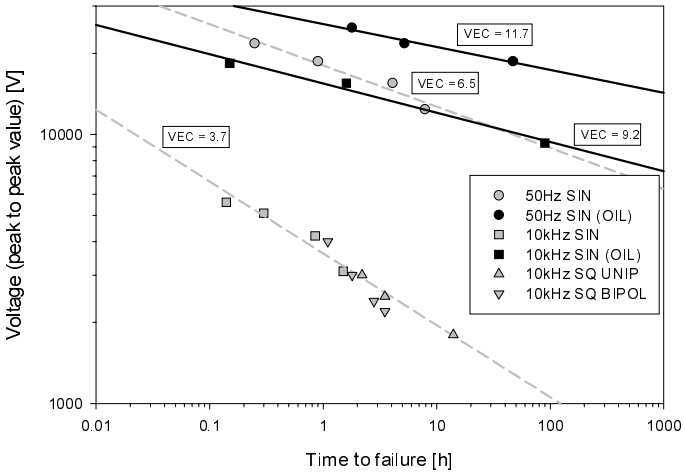

Fig. 5.23: Life test results (at probability 63.2%) and life lines as function of peak-to-peak voltage for tests performed in air and in oil with sinusoidal wave at 50 Hz and 10 kHz and for tests in air with 10 kHz square wave on material #A.

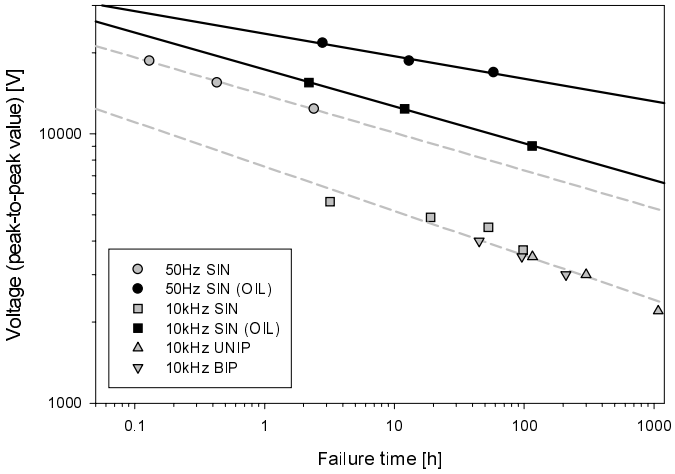

Fig. 5.24: Life test results (at probability 63.2%) and life lines as function of peak-to-peak voltage for tests performed in air and in oil with sinusoidal wave at 50 Hz and 10 kHz and for tests in air with 10 kHz square wave on material #B.

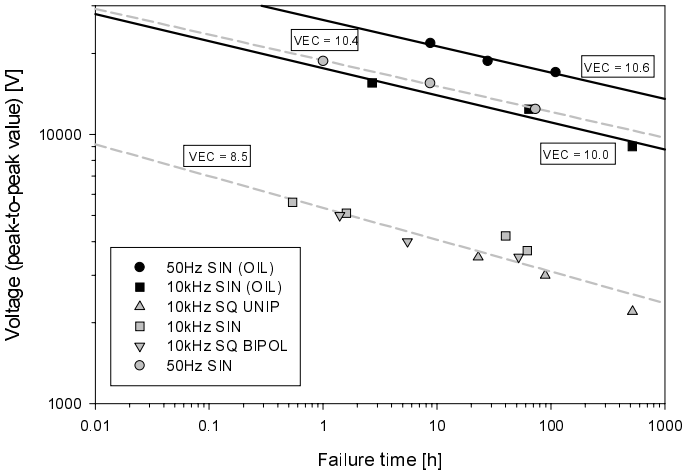

Fig. 5.25: Life test results (at probability 63.2%) and life lines as function of peak-to-peak voltage for tests performed in air and in oil with sinusoidal wave at 50 Hz and 10 kHz and for tests in air with 10 kHz square wave on material #C.

Performing life tests on material #A at a peak-to-peak voltage of 1.5 kV, at six different levels of slew rate (0.75, 1, 2, 5, 50 and 75 kV/μs) the effect of the slew rate (dV/dt) of the voltage waveform on the life of the wire can be singled out. Some authors found, in fact, large life reduction when the slew rate increases [34, 44], while others, did not obtain any

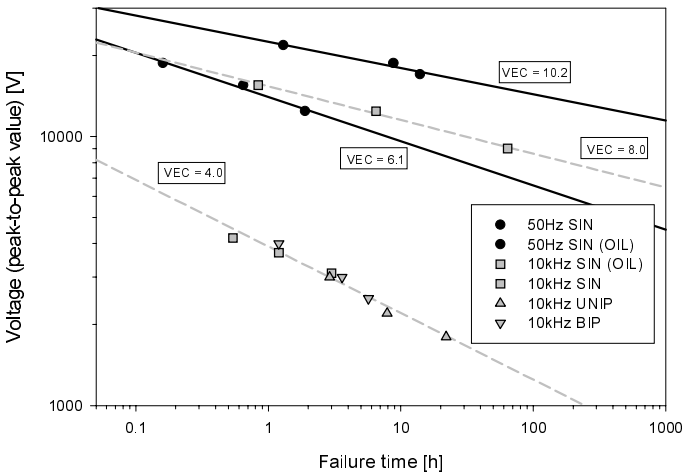

Fig. 5.26: Life test results (at probability 63.2%) and life lines as function of peak-to-peak voltage for tests performed in air and in oil with sinusoidal wave at 50 Hz and 10 kHz and for tests in air with 10 kHz square wave on material #D.

correlation with degradation acceleration [39, 46]. The results of life tests reported in Fig. 5.27 show that a linear relation exists between life and slew rate in the range 5-75 kV/μs. The higher the slew rate the shorter the life, i.e. the increase of the switching rate of electronic components (the rise of the slew-rate improves the IGBT and MOS-FET efficiency) can overstress the insulation system, reducing its life. However, below 5 kV/μs life seems to be quite independent of the slew rate confirming test results reported in Figs. 5.23-5.26, which were performed with slew rate ≤1kV/μs.

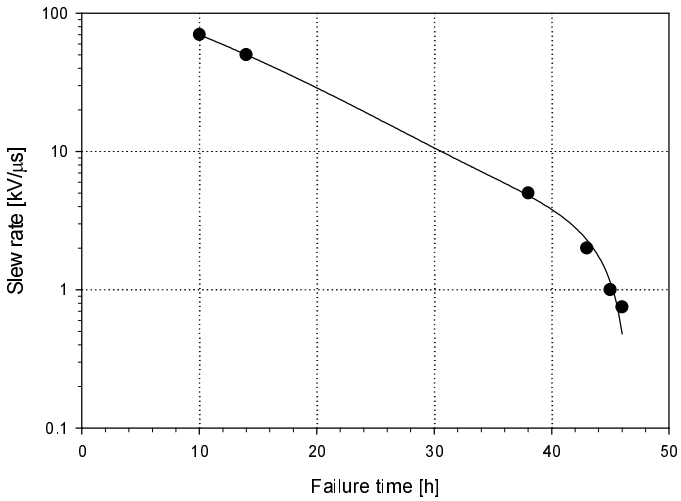

Fig. 5.25: Behaviour of the slew-rate as a function of the ageing time. Bipolar square wave at 10 kHz, Vpp=1.5 kV, material #A.

Chapter 6

Space charge measurement results

6.1 Premise

Space charge measurements on enamelled wires are rather innovative and could have been performed thanks to the special PEA system described in the fourth chapter.

Since some authors hypothesised interactions between life behaviour and space charge trapping features of insulating materials, the space charge measurements here performed have the purpose of providing a contribution to the investigation of this topic.

The space charge measurements here presented are carried out in DC and AC, the latter at three different frequencies, i.e. 0.1 Hz, 50 Hz and 10 kHz, with unipolar and bipolar square waveforms. While DC measurements have the main purpose of characterising material behaviour in terms of injection and transport properties, AC measurements should provide information on the extent (increase/decrease) of trapped charge as a function of frequency, involving frequencies typical of PWM modulating and carrying.

Under DC poling field, the amount of trapped charge increases with time until a steady state is reached. Looking at the Fig. 6.1, which shows the maximum stored charge density Q_M for material #A as a function of poling time, steady state is reached after 30 min and 60 min for poling fields of 30 kV/mm and 15 kV/mm, respectively.

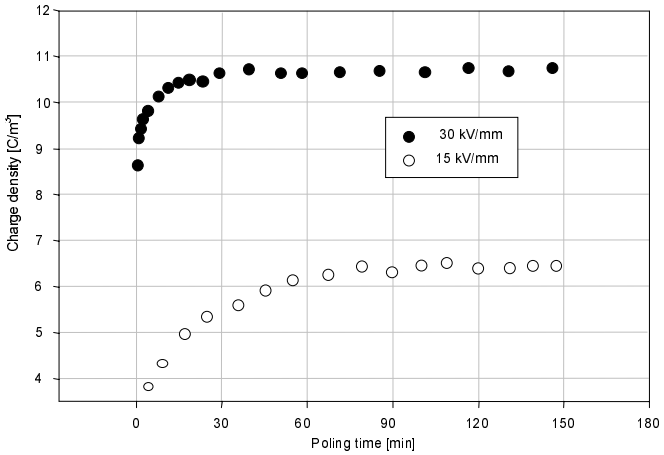

Fig. 6.1: Stored charge as function of poling time for two different electric field levels (30 kV/mm DC and 15 kV/mm DC).

A poling time of 3600 s and a field of 30 kV/mm, which means an applied voltage of 1 kV for an enamel thickness of 35 μm, were chosen both for AC and DC tests. Then, voltage is removed and a depolarisation period of about 3600 s follows polarisation. As can be observed in the Fig. 6.2, in DC case polarisation is performed with positive and negative voltage, in order to investigate the dependence of space charge on voltage polarity.

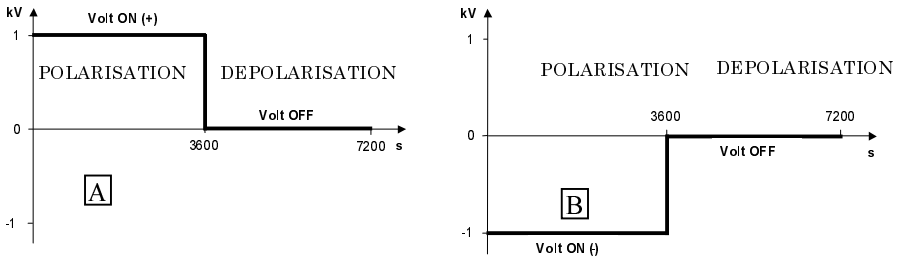

Fig. 6.2:Positive (A) and negative (B) poling procedure

Space charge profiles obtained during polarisation and depolarisation, as well as space charge quantities, total absolute stored charge density, Q_M, and the slope of the depolarisation characteristics, i.e. the rate of charge decay, s, are reported in the following for each test. Patterns are also provided, showing the behaviour of space charge distribution in the insulation bulk as function of test time.

6.2 DC space charge measurements

6.2.1 Positive polarity

Figures 6.3-6.6 show the polarisation profiles (A) 20 s and 3600 s after beginning of polarisation, as well as depolarisation profiles (B) obtained 2 second after grounding, i.e. 3602 s after test beginning, and 100 s later. The dashed areas indicate trapped charge considered to calculate total absolute stored charge density Q_M. Moreover, the blue dashed lines show the electrode location.

These profiles show an evident space charge accumulation, with extent depending on the kind of insulating material. The enamelled wire labelled as #A (Fig. 6.3) shows an accumulation of negative charge near the cathode (homocharge), thus decreasing the charge on the negative electrode and increasing that on the positive electrode, due to relevant image charge (Fig. 6.3A). This is more evident from the profiles obtained during depolarisation, Fig. 6.3B, which show electrode charge due only to the image of accumulated internal charge. After 100 s from voltage removal a large amount of trapped charge is disappeared (expelled or recombined). This can be observed also by pattern of Fig. 6.7.

Materials #B and #C shows an similar behaviour of homocharge accumulation (Figs. 6.4A and 6.5A), but the extent of trapped charge is so large (and they are so closed to the electrodes) that the negative peak on the anode seems to move inside the insulation during polarisation. The large amount of trapped charge can be seen clearly by depolarisation profiles of Figs. 6.4B and 6.5B; 100 second after voltage removal the charge is significantly decreased.

The patterns, reported in Figs. 6.7-6.10, emphasise the clear evolution of negative peak on the cathode during polarisation.

Finally, material #D shows an accumulation of homocharge also near to the positive electrode (Fig. 6.6A), with consequent apparent moving of the peak inside the insulation. Therefore, after voltage removal, a large amount of charge (in absolute value) is accumulated in insulation bulk (Fig. 6.6B). Note that charge decrease during depolarisation is significantly slower than for the other materials, especially for positive stored charge. This can be seen also by the patterns (Figs. 6.7-6.10).

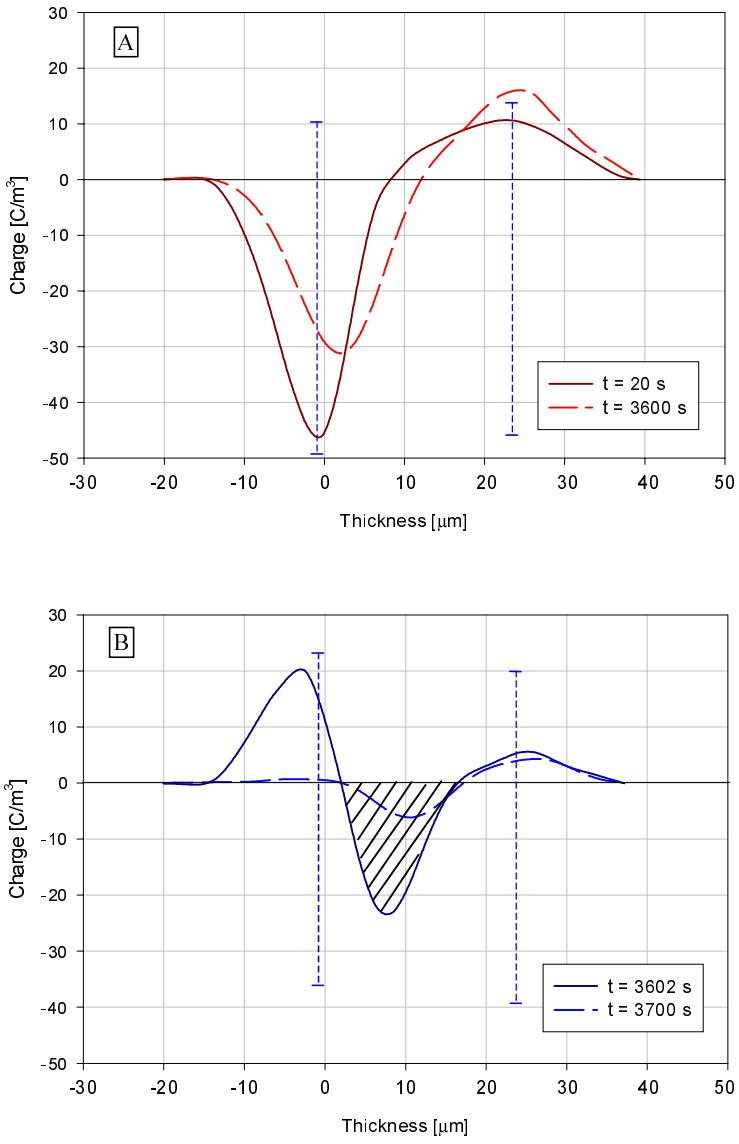

Fig. 6.3: Space charge profiles during polarisation (A) and depolarisation (B). Material #A. Poling voltage 1 kV DC positive.

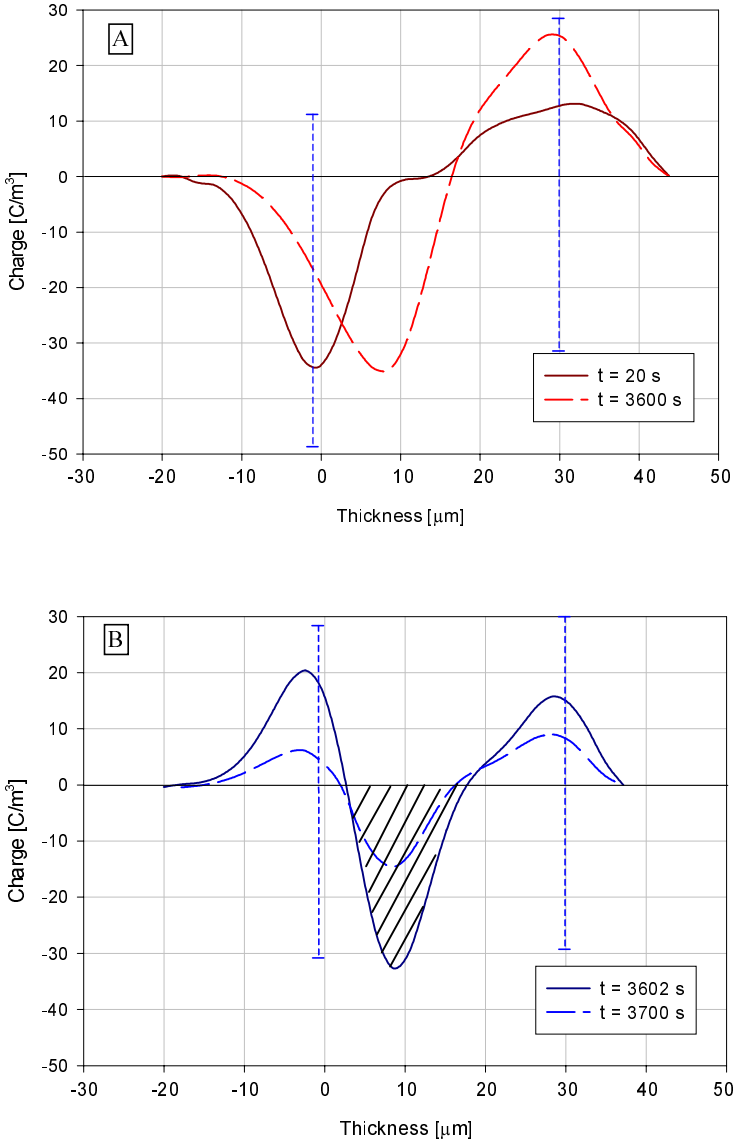

Fig. 6.4: Space charge profiles during polarisation (A) and depolarisation (B). Material #B. Poling voltage 1 kV DC positive.

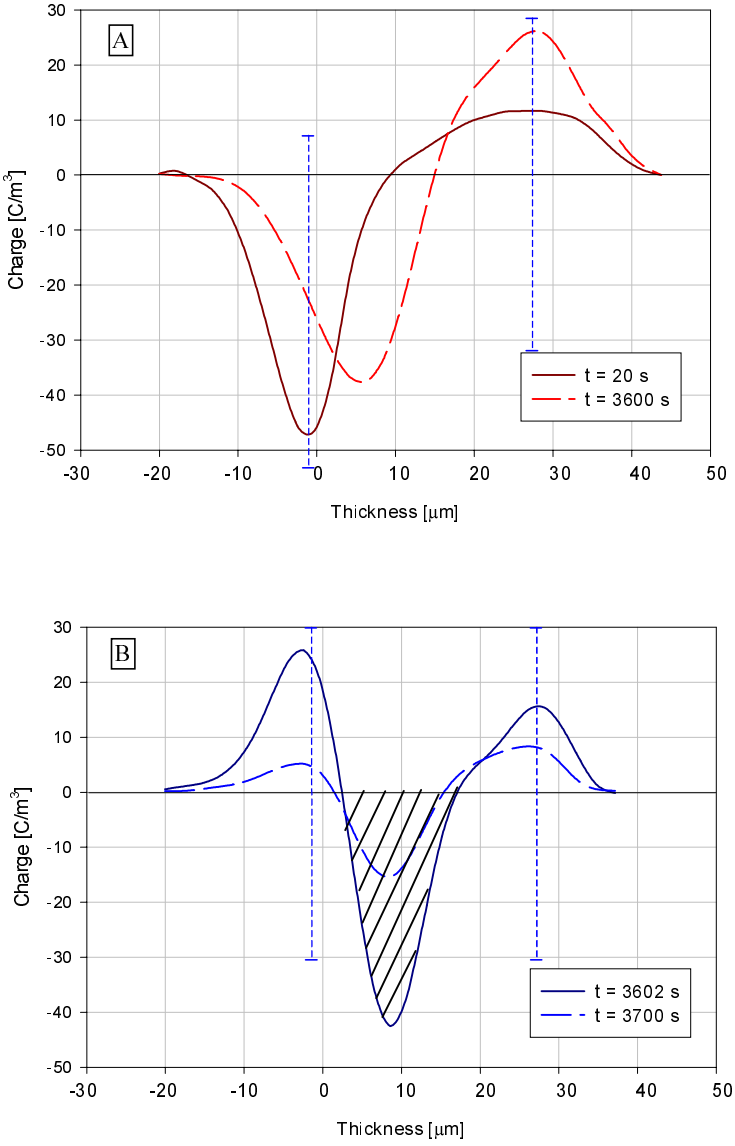

Fig. 6.5: Space charge profiles during polarisation (A) and depolarisation (B).
Material #C. Poling voltage 1 kV DC positive.

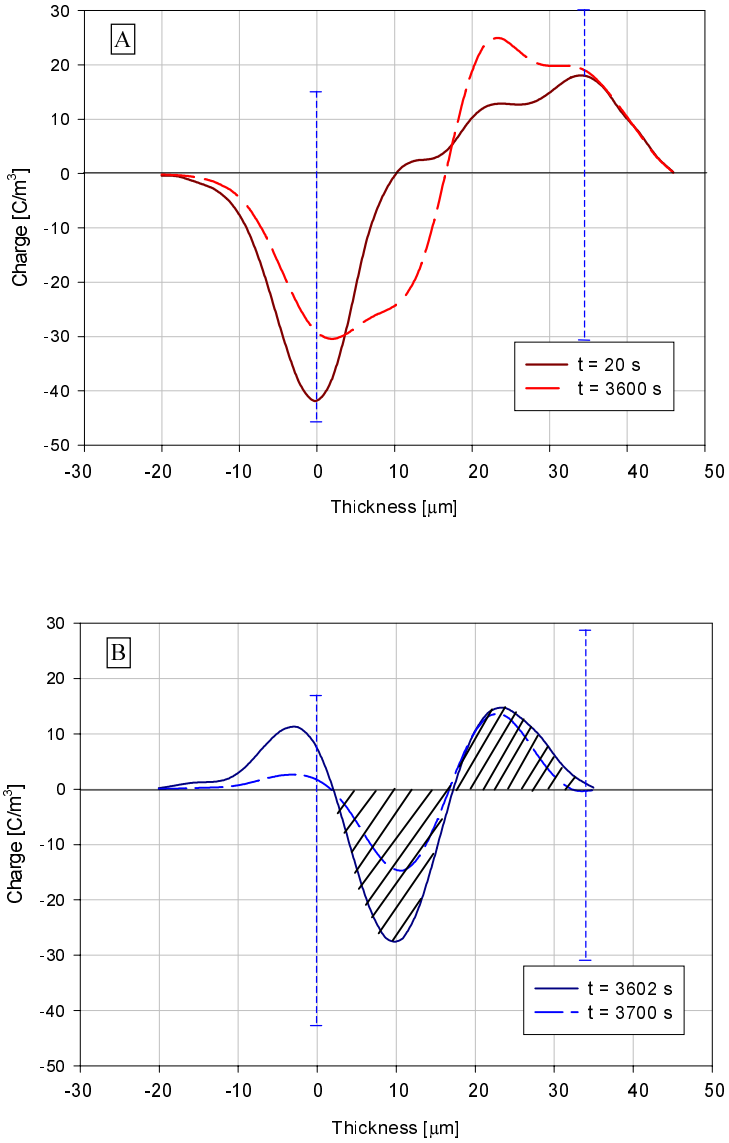

Fig. 6.6: Space charge profiles during polarisation (A) and depolarisation (B).
Material #D. Poling voltage 1 kV DC positive.

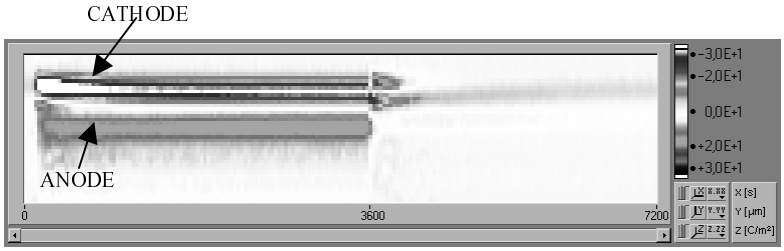

Fig. 6.7: Space charge pattern for material #A. Poling voltage 1 kV DC positive.

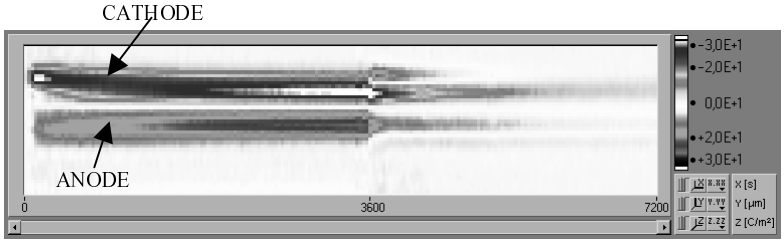

Fig. 6.8: Space charge pattern for material #B. Poling voltage 1 kV DC positive.

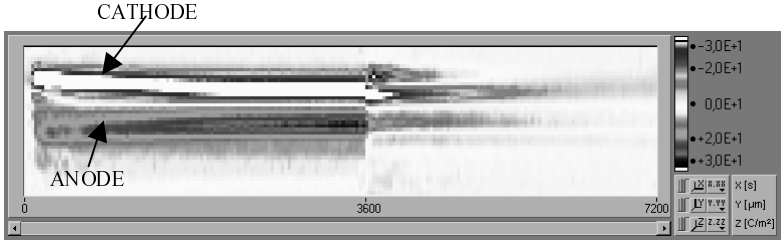

Fig. 6.9: Space charge pattern for material #C. Poling voltage 1 kV DC positive.

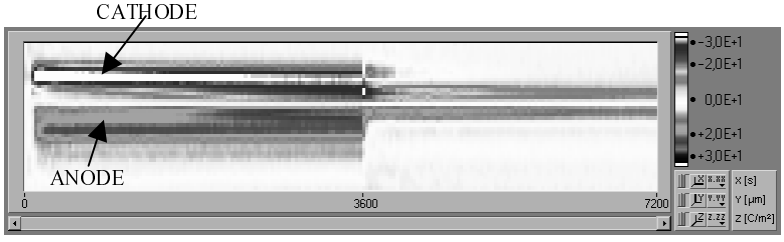

Fig. 6.10: Space charge pattern for material #D. Poling voltage 1 kV DC positive.

Indeed, the depolarisation characteristic of material #D is considerably different from the others (Fig. 6.11). This material is characterised by a rate of charge decay very small (the slope of

depolarisation characteristic is s = 0.14), due to the likely presence of a broad distribution of traps occupied by injected charges, having lower limit which corresponds to traps deeper than for the other materials (this will be more deeply discussed in the next chapter). We recall that charges accumulated in deeper traps will suffer longer detrapping, and, hence, transport times.

The other CR materials show, on the contrary, larger rate of charge recombination/expulsion similar to that relevant to traditional material #A, which seems to be the largest.

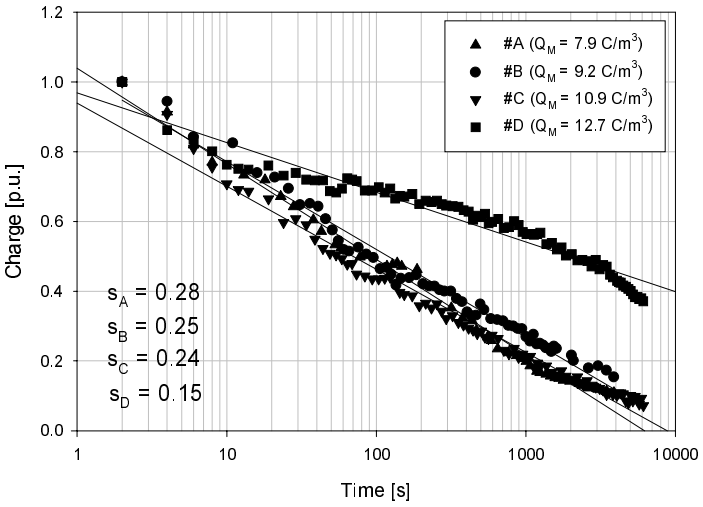

Fig. 6.11: Depolarisation characteristics for #A, #B, #C and #D. Poling voltage: DC positive. The slope of the regression line, s, is also indicated.

The amount of charge accumulation is provided by quantity Q_M plotted for each material in Fig. 6.12, together with *s*. Material #D, besides being the slowest to detrap charge, shows attitude to accumulate a larger amount of charge (Q_M=12.7), followed by #C (Q_M=10.9), #B (Q_M=9.2) and #A (Q_M=7.9).

Let us note that disomogenities of multistrate CR insulation can introduce interfaces acting as charge centres and traps, whose depth depends on chemical and microstructural material properties, thus inducing insulation to accumulate a larger amount of space charge with respect to the traditional one.

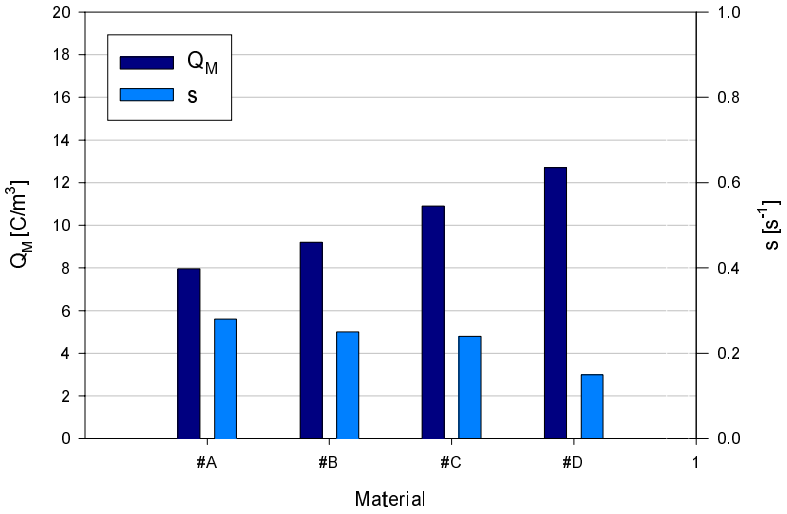

Fig. 6.12: Values of space charge quantity Q_M and s for materials #A, #B, #C and #D.

6.2.2 Negative polarity

Figures 6.13 - 6.16 provide polarisation (A) and depolarisation (B) profiles, for space charge measurements under DC negative voltage (1 kV poling voltage, 30 kV/mm field).

These profiles show again an homocharge accumulation (positive), and consequently a reduction of the charge peak on the electrode near which the charge builds up. The charge accumulation depends on the insulating material, but is larger than with positive voltage (with the exception of #A which does not show significant changes as regard amount of accumulated charges. The electrode charge apparent peak movement inside the insulation, sign of large homocharge accumulation, is more evident than with positive voltage, as shown by patterns of Figs. 6.17-6.20.

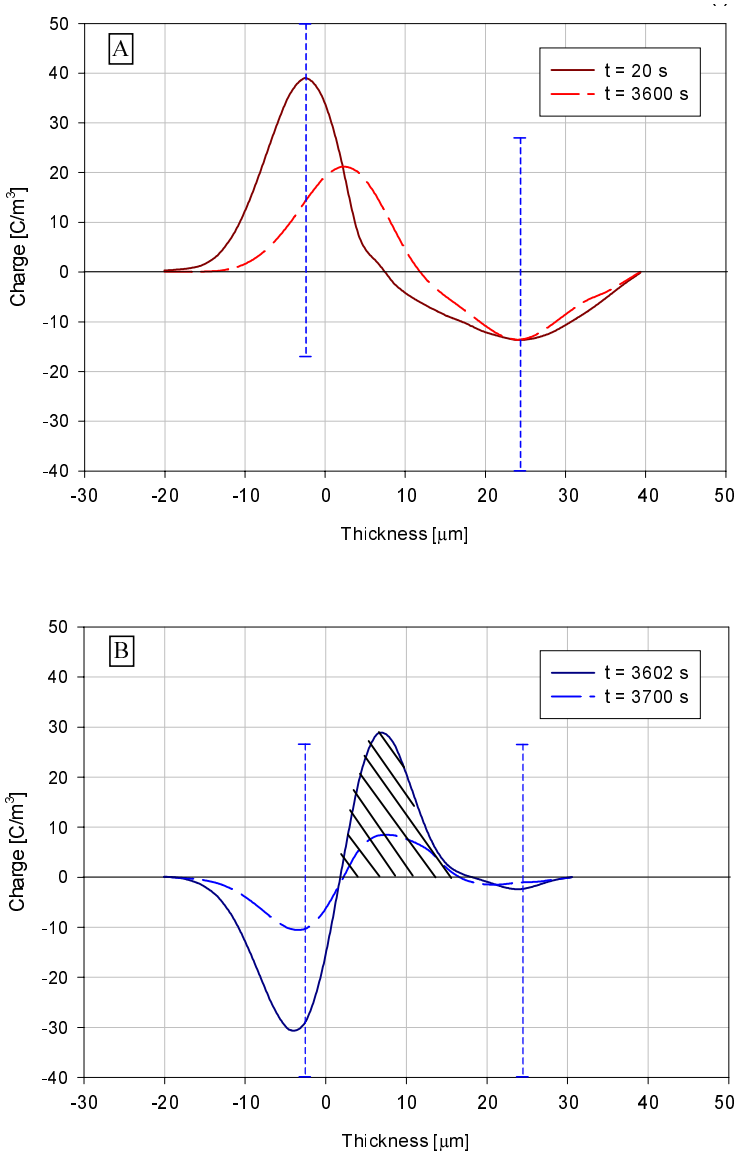

Fig. 6.13: Space charge profiles during polarisation (A) and depolarisation (B). Material #A. Poling voltage 1 kV DC negative.

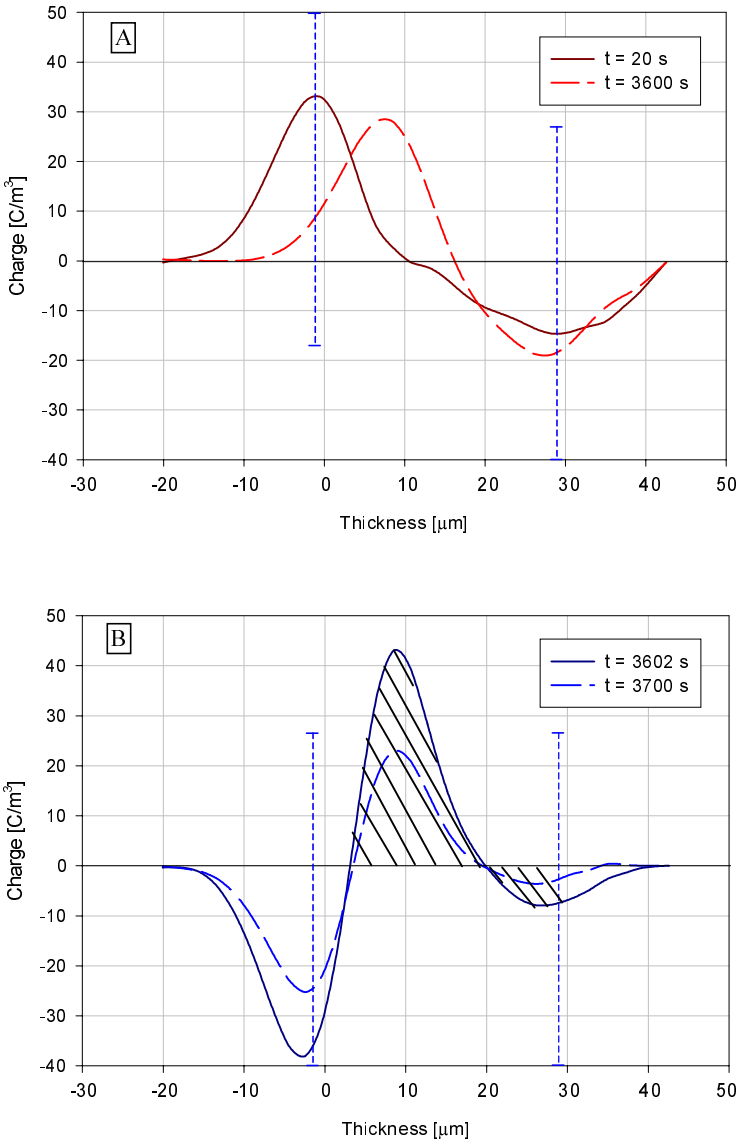

Fig. 6.14: Space charge profiles during polarisation (A) and depolarisation (B). Material #B. Poling voltage 1 kV DC negative.

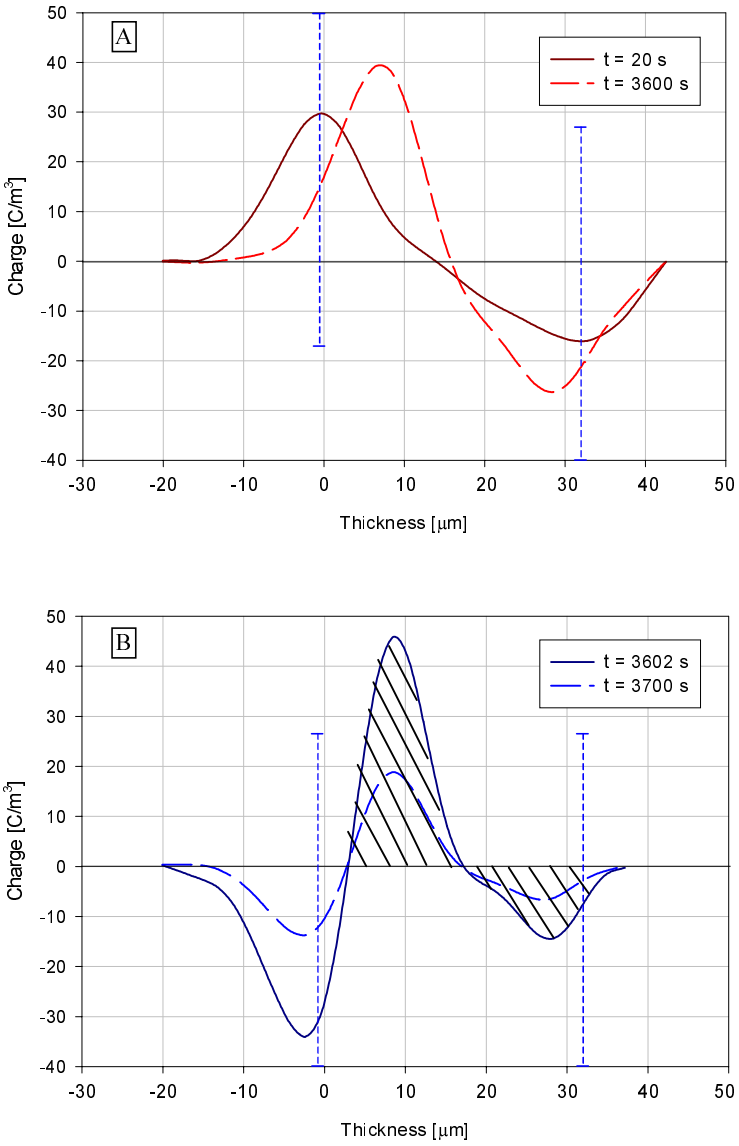

Fig. 6.15: Space charge profiles during polarisation (A) and depolarisation (B). Material #C. Poling voltage 1 kV DC negative.

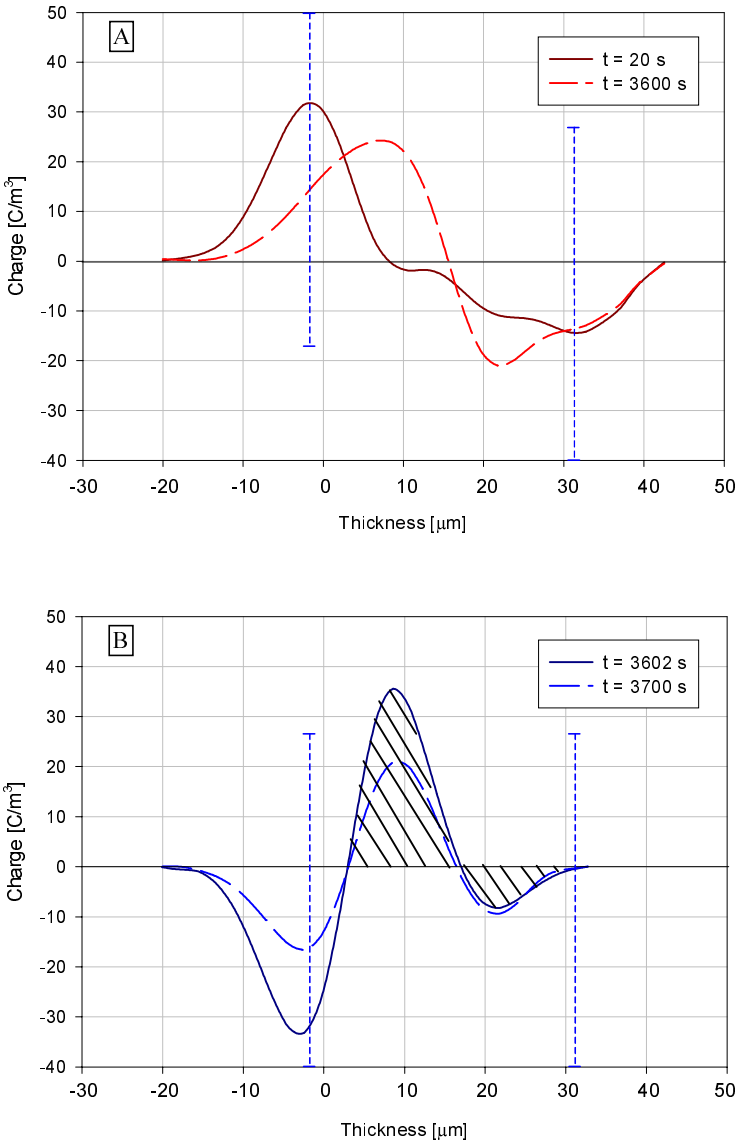

Fig. 6.16: Space charge profiles during polarisation (A) and depolarisation (B). Material #D. Poling voltage 1 kV DC negative.

Fig. 6.17: Space charge pattern for material #A. Poling voltage 1 kV DC negative.

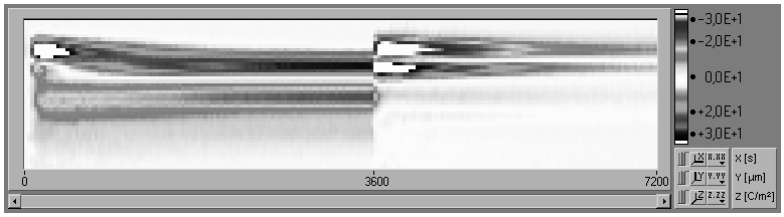

Fig. 6.18: Space charge pattern for material #B. Poling voltage 1 kV DC negative.

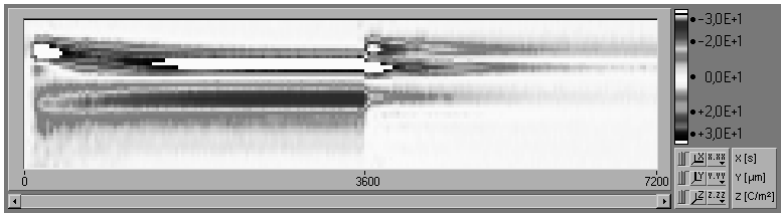

Fig. 6.19: Space charge pattern for material #C. Poling voltage 1 kV DC negative.

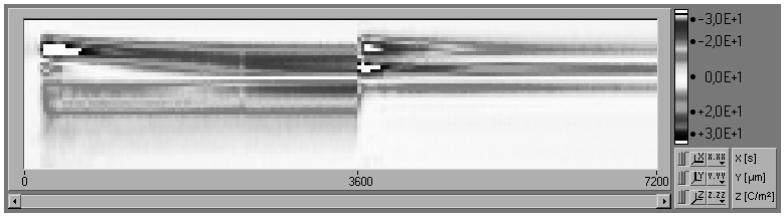

Fig. 6.20: Space charge pattern for material #D. Poling voltage 1 kV DC negative.

Depolarisation characteristics reported in Fig. 6.21 highlight the same behaviour as under positive poling field, i.e. material #D is again the slowest in charge drifting, even if (less than in tests with positive voltage). Table 1 summarises quantities Q_M and s for the four materials with positive and negative voltage.

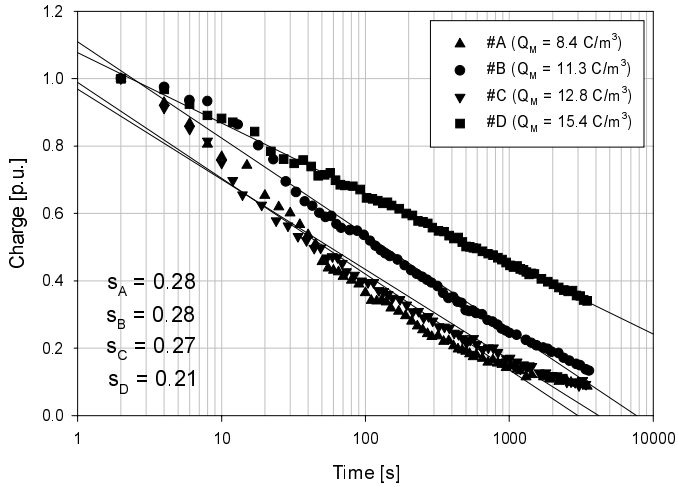

Fig. 6.21: Depolarisation characteristics for #A, #B, #C and #D. Poling voltage: DC negative. The slope of the regression line, s, is also indicated.

Tab. 6.1: Values of space charge quantities Q_M and s calculated for positive and negative poling voltage.

Test	Quantity	Material #A	Material #B	Material #C	Material #D
Positive	Q_M [C/m^3]	7.9	9.2	10.9	12.7
	s [s^{-1}]	0.28	0.25	0.24	0.15
Negative	Q_M [C/m^3]	8.4	11.3	12.8	15.4
	s [s^{-1}]	0.28	0.28	0.27	0.21

6.3 AC space charge measurements

The results of space charge measurements under square waveforms varying voltage frequency (0.1Hz, 50Hz and 10kHz) and waveshape (unipolar, bipolar) are collected in this paragraph.

The peak value of the square wave was kept constant at 1000 V, the same amplitude used for DC measurements, in order to compare directly AC with DC results. The experimental set-up is more complicated in this case and is described in the chapter 4. The poling period, as well as depolarisation time, was 3600 s.

As can be seen from Fig. 6.22, acquisitions performed by the digital signal averager (DSA) were synchronised with positive peak of the square wave. Each space charge profile displayed is the result of an average of several acquisitions recorded and collected by the DSA.

6.3.1 Unipolar Square wave

Figures 6.23 and 6.24 show space charge profiles during polarisation (A) and depolarisation (B) under square waveform at 0.1 Hz for materials #A and #C, respectively. Profiles relevant to #B and #D, that do not reveal significant qualitative differences, are not reported. Passing from DC to 0.1 Hz we can observe a significant decrease of the amount of trapped charge. Moreover, after voltage removal, the charge is expelled faster than in DC regime, so that after 100 s a very small residual charge can be observed. Material #C shows, again, charge accumulation larger than #A.

It is noteworthy that the amount of accumulated charge is smaller than under DC, even if a non-negligible DC component is present in the unipolar square waveform (however, the rms voltage of this component is considerably smaller than that of DC tests, i.e. $1/\sqrt{2}$).

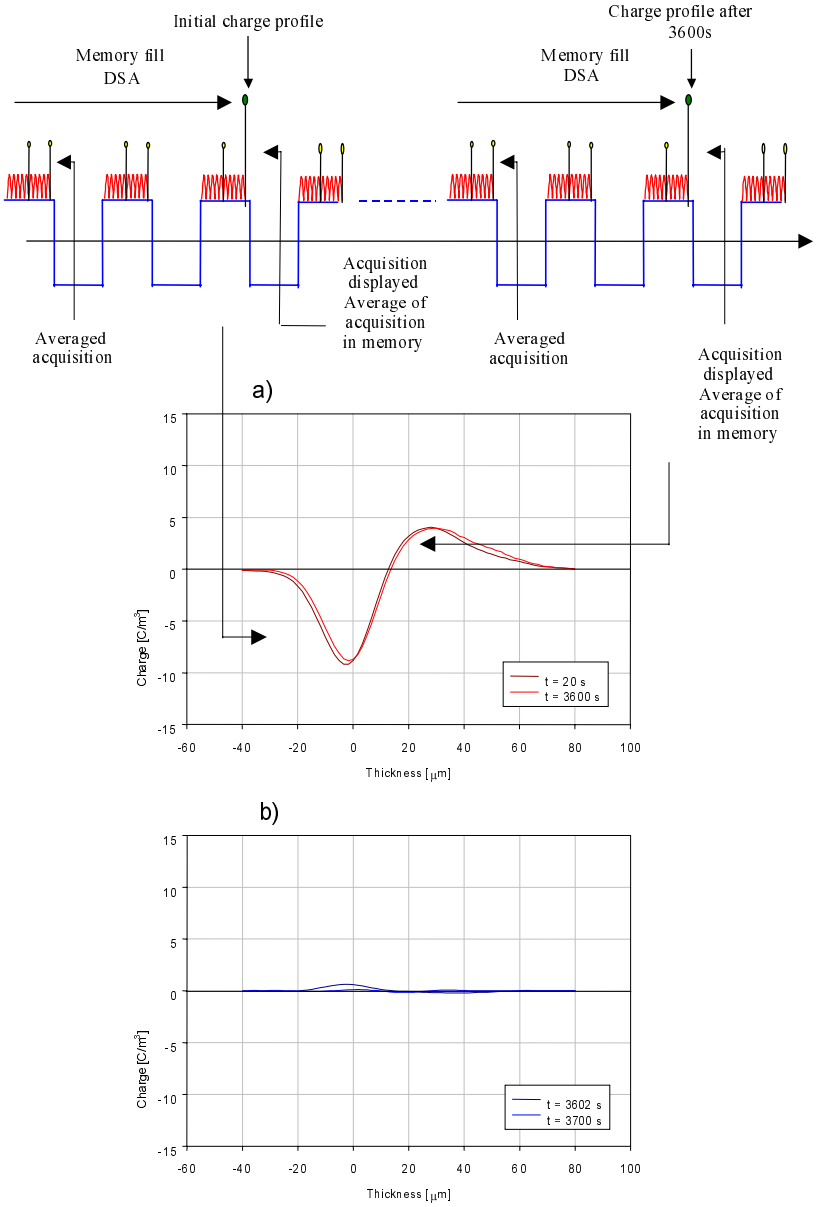

Fig. 6.22: Example of acquisition procedure for AC poling voltage and PEA data acquired during polarisation (A) and depolarisation (B) period.

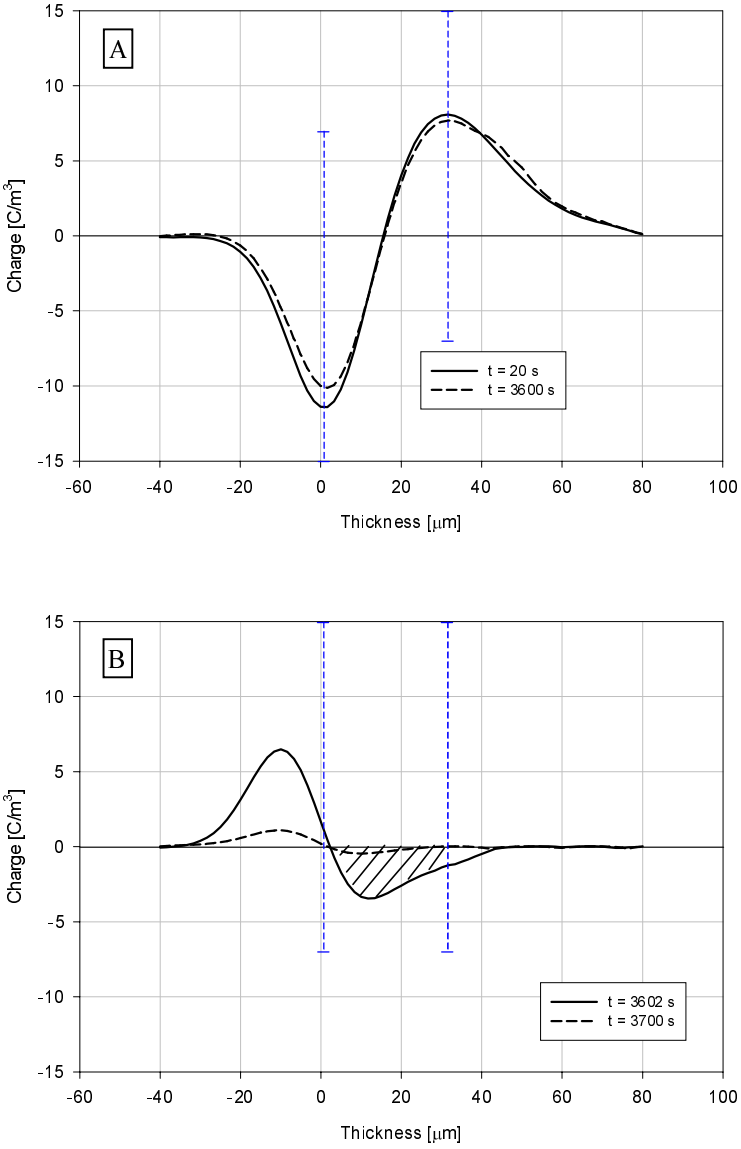

Fig. 6.23: Space charge profiles during polarisation (A) and depolarisation (B). Material #A. Poling voltage squaewave unipolar 0.1 Hz, 1 kV peak.

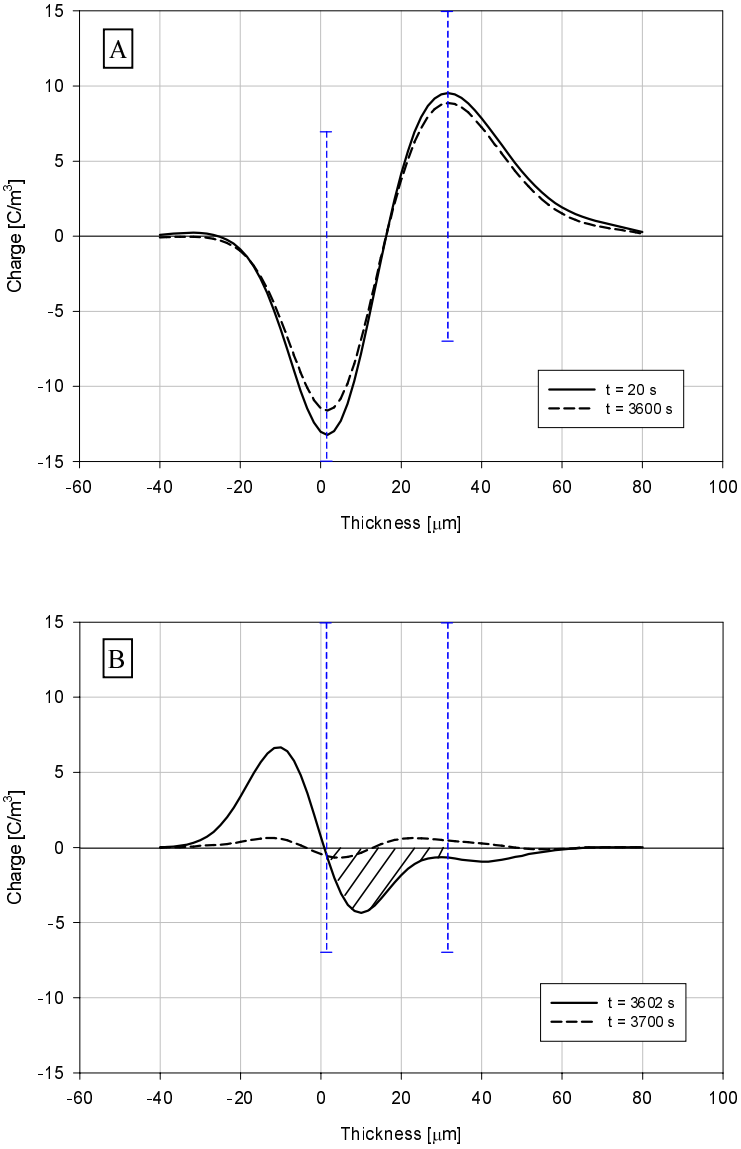

Fig. 6.24: Space charge profiles during polarisation (A) and depolarisation (B). Material #C. Poling voltage squarewave unipolar 0.1 Hz, 1 kV peak.

It is possible to observe from Fig. 6.25 that the behaviour of the depolarisation characteristics for materials #B, #C and #D exhibits a bend, while for material #A it is quite linear. Experimental points can, thus, be fitted by two lines with different slopes. For materials #B and #D the line which approximate the depolarisation characteristic for the first 150s shows a slope of 0.42 and 0.41, respectively, and a second slope of 0.18 (#B) and 0.25(#D) relevant to the subsequent period. For material #C the depolarisation characteristic is approximated by a line with slope 0.51 for the first 40-50 s and by a second line with slope 0.19 for the subsequent period. This behaviour and the larger values of slope with respect to DC polarisation, may be explained observing that AC injected charge is much smaller than in DC [77] and, moreover, charge is mainly located very close to the electrodes (only small amount of charge penetrates in insulation bulk, i.e. that relevant to the DC component). Hence, in this case the depolarisation characteristic is largely influenced, especially in the first part, by charge extraction (from material to electrode), while the long time behaviour of the depolarisation characteristic is likely due to the slow drift of charges accumulated in the bulk and reaching electrodes, as it happens prevailingly in DC: for this reason the slope of the long-term part of the depolarisation characteristic in AC unipolar is close to that obtained in DC.

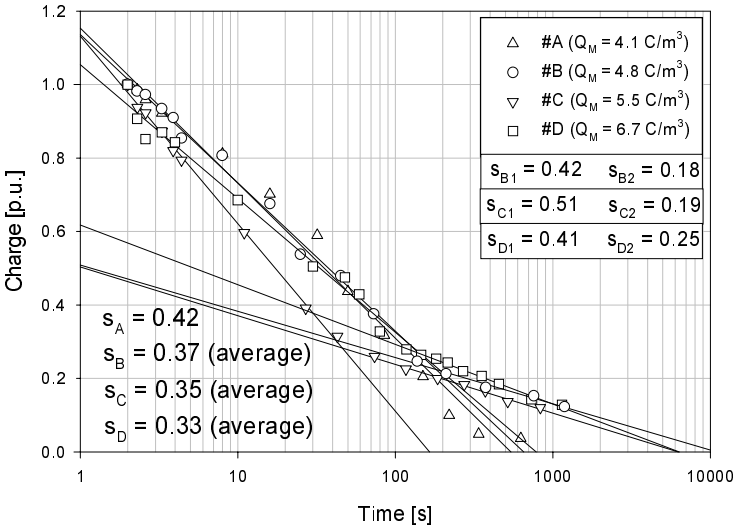

Fig. 6.25: Depolarisation characteristics for #A, #B, #C and #D. Poling voltage: 0.1 Hz square unipolar. The slope of the regression line, s, is also indicated.

Figures 6.26 and 6.27 show space charge profiles during polarisation (A) and depolarisation (B) for tests performed with square waves unipolar at 50 Hz, for materials #A and #C, respectively, while Figs. 6.28 and 6.29 report space charge profiles relevant to tests with unipolar square wave at 10 kHz, again for materials #A and #C, respectively.

As already mentioned, space charge accumulation is quite significant also at high frequency, but smaller than in DC case. Then, as can be seen from depolarisation characteristics, after voltage removal, the charge is dissipated very quickly. As expected with increased frequency, charge is accumulated closer and closer to the electrodes, so that the low-slope long term depolarisation behaviour detected at 0.1 Hz (Fig. 6.25) appears less clearly in Fig. 6.30 and 6.31. This is also the reason because the depolarisation characteristics for all the tested materials have almost the same slopes: detrapping does not interest, in fact, the bulk properties (trap distribution, mobility), but, rather, the interfacial behaviour.

Looking to depolarisation characteristics relevant to tests at 50 Hz (Fig. 6.30) and 10 kHz (Fig. 6.31), one can observe that material #D is always the slowest material to drift charge.

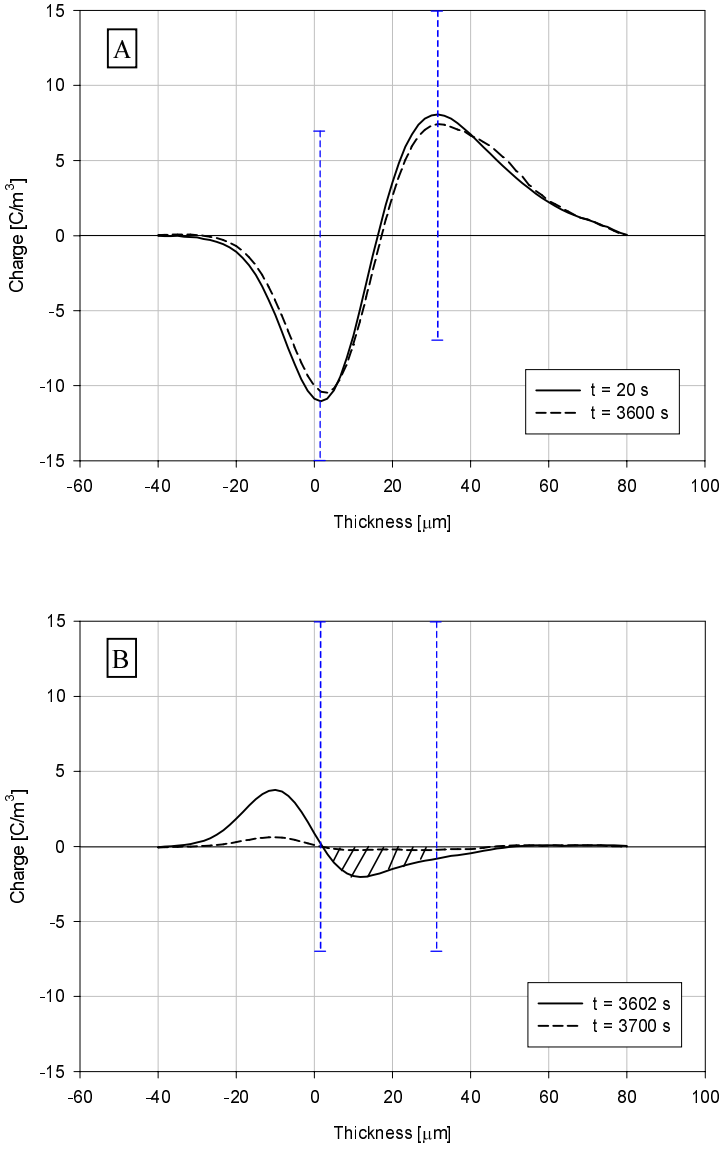

Fig. 6.26: Space charge profiles during polarisation (A) and depolarisation (B). Material #A. Poling voltage squarewave unipolar 50 Hz, 1 kV peak.

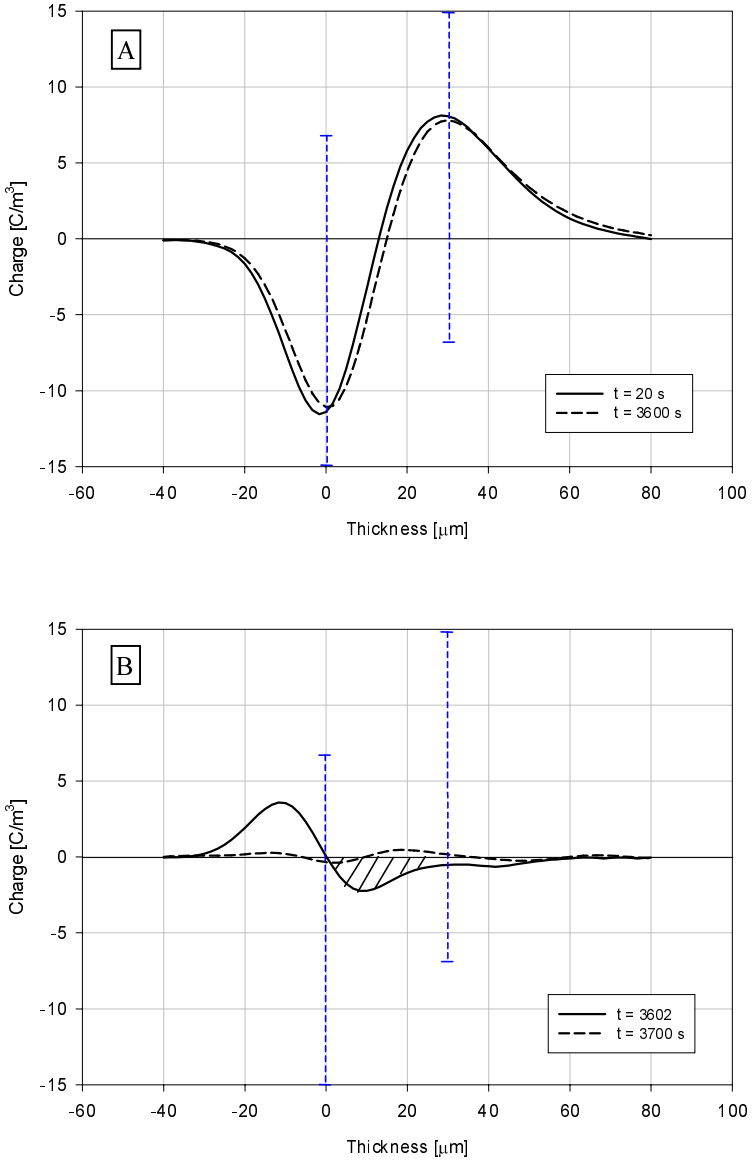

Fig. 6.27: Space charge profiles during polarisation (A) and depolarisation (B). Material #C. Poling voltage squarewave unipolar 50 Hz, 1 kV peak.

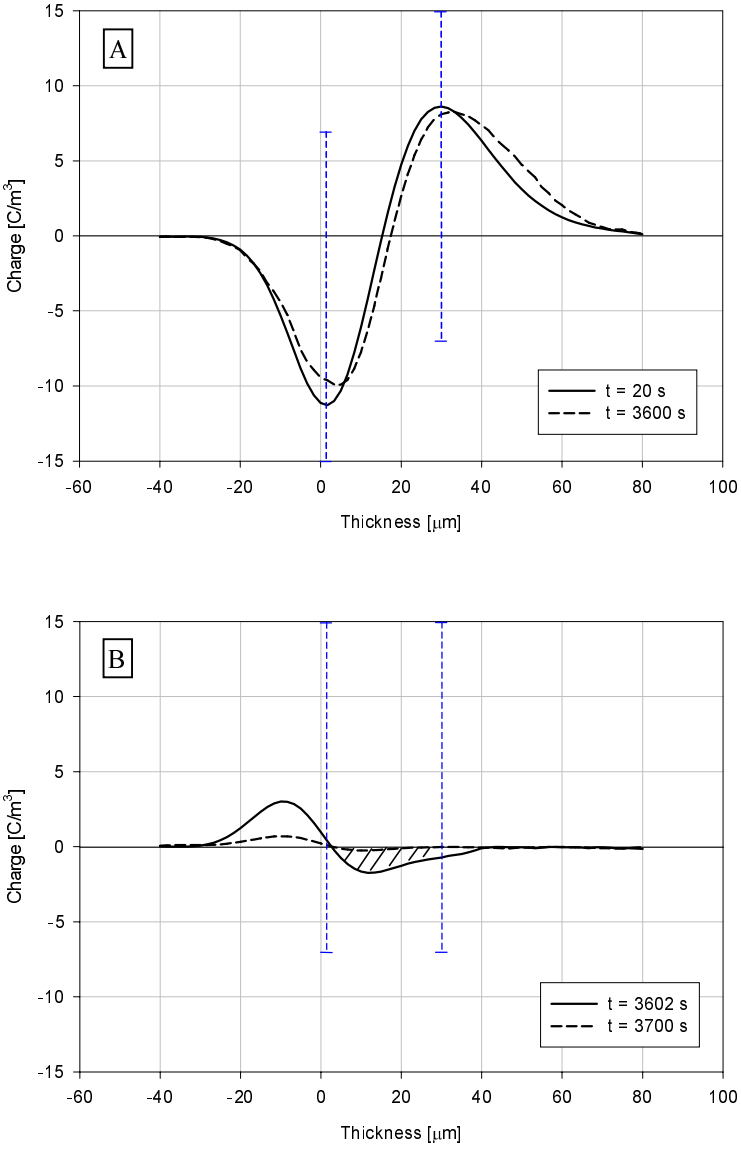

Fig. 6.28: Space charge profiles during polarisation (A) and depolarisation (B). Material #A. Poling voltage squarewave unipolar 10 kHz, 1 kV peak.

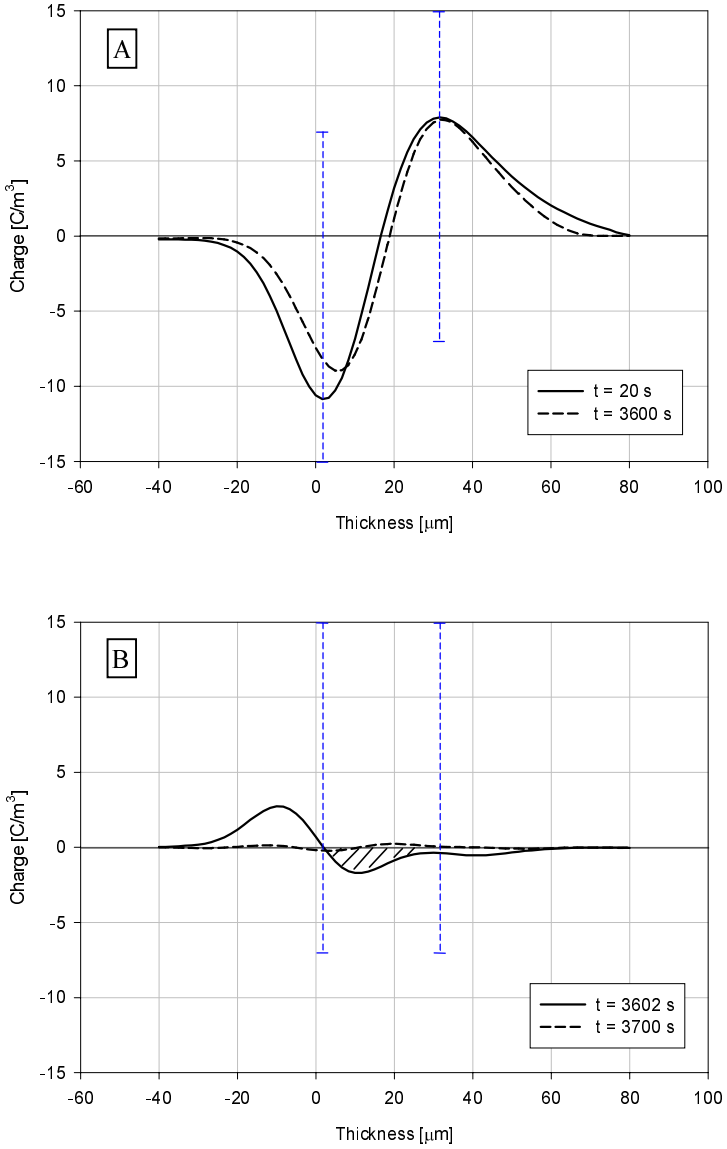

Fig. 6.29: Space charge profiles during polarisation (A) and depolarisation (B). Material #C. Poling voltage squarewave unipolar 10 kHz, 1 kV peak.

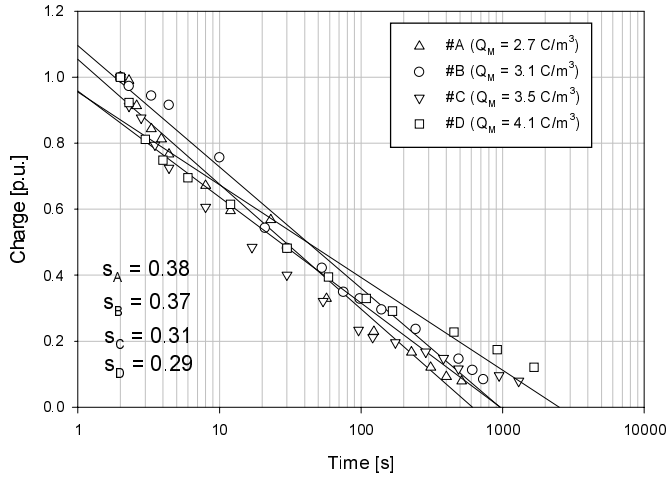

Fig. 6.30: Depolarisation characteristics for #A, #B, #C and #D. Poling voltage: 50 Hz square unipolar. The slope of the regression line, s, is also indicated.

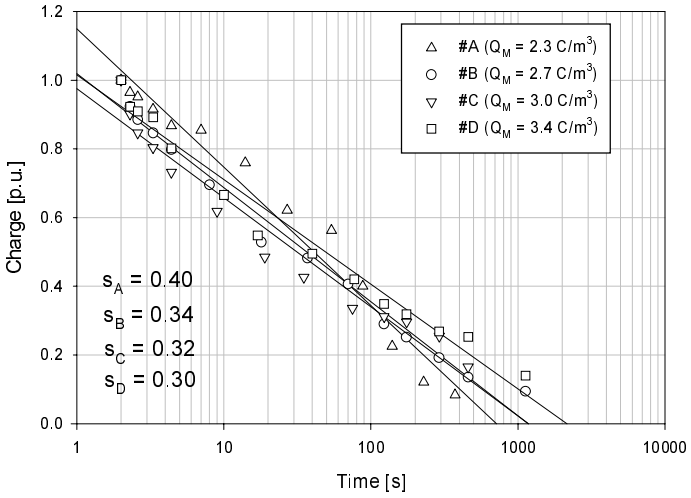

Fig. 6.31: Depolarisation characteristics for #A, #B, #C and #D. Poling voltage: 10 kHz square unipolar. The slope of the regression line, s, is also indicated.

Table 6.2 and Fig. 6.32 summarise the quantities obtained from space charge measurements, i.e. the stored charge, Q_M, and the rate of charge drift, s, relevant to the tests with unipolar square waveform at three different frequencies for each material.

A decrease of Q_M as the frequency increases is evident, due to frequent poling voltage inversions which does not allow net charge to be accumulated significantly inside insulation [77].

Looking at Fig. 6.32, the fitting curves show a sort of tendency to a threshold. The decrease of accumulated space charge is steep up to 50 Hz, reaching a lower limit value of 2-3 C/m^3, depending on the material. This value can be attributed to DC component of the AC waveform and to a small amount of AC-injected (superficial) charge.

Comparing these results with those obtained under DC regime, one can see that material #A is, even with unipolar voltage, the material which accumulates less charge and with the largest slope, while #D is again a material in which space charge is largely accumulated and hardly dissipated.

Finally a comment regarding space charge profiles. Due to the spatial resolution of the space charge measurement system (around 8 μm) and the small thickness of specimens, charge appears to be spread in the bulk even at increasing frequencies (this is also the reason of apparent movement of electrode charge peak in the bulk). However, measurements carried out on thicker (flat) specimens show clearly that the charge injected by the AC-component of poling field is largely accumulated close to electrodes [99].

Tab. 6.2: Values of space charge quantities Q_M and s calculated for unipolar square wave at different frequencies.

Test	Quantity	Material #A	Material #B	Material #C	Material #D
Unipolar 0.1Hz	Q_m [C/m^3]	4.1	4.8	5.5	6.7
	s_{med} [s^{-1}]	0.42	0.37	0.35	0.33
Unipolar 50Hz	Q_m [C/m^3]	2.7	3.1	3.5	4.1
	s [s^{-1}]	0.38	0.37	0.31	0.29
Unipolar 10kHz	Q_m [C/m^3]	2.3	2.7	3.0	3.4
	s [s^{-1}]	0.40	0.34	0.32	0.30

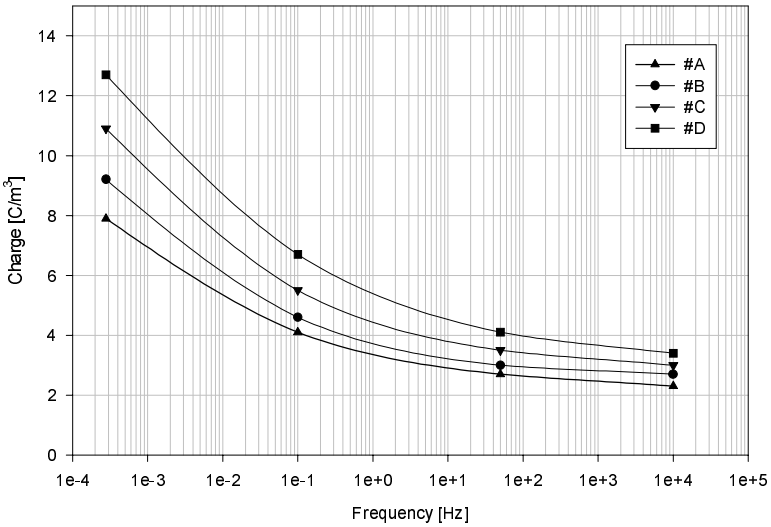

Fig. 6.32: Stored charge density behaviour for #A, #B, #C and #D as function of the voltage frequency. Poling voltage: square unipolar.

6.3.2 Bipolar Square wave

Profiles (polarisation/depolarisation) obtained from space charge measurements are reported in Figs. 6.33 and 6.34 for tests with bipolar square waveform at 0.1 Hz relevant to material #A and #C, respectively. We can see that trapped space charge is significantly less with respect to DC or unipolar wave. Looking at charge profile during depolarisation relevant to material #C an unexpected behaviour can be observed. Four charge profiles recorded during depolarisation are reported in Fig. 6.34B (after 2s, 4s, 20s and 100s). Instead of continuous trapped charge decrease during depolarisation, after 3-4 s an inversion of charge peaks and an increase of signal amplitude can be noted. This phenomenon occurs both at 0.1 Hz and at 50 Hz for the three CR materials, but not for #A. This fact can be seen more clearly comparing the depolarisation characteristics of Figs. 6.35A and 6.38A, relevant to 0.1 Hz and 50 Hz tests, respectively. After a rapid initial decrease, CR materials (especially #C) show a constant increase of charge (calculated in absolute value) for a period of time of 20-30 s, afterwards a slow charge decrease takes place, extending for a long time with a behaviour similar to that seen in tests with DC voltage or unipolar square wave. This could be explained remembering that the tested materials showed a larger space charge accumulation under negative voltage, with respect to positive. The charge injected at each negative half-period can be

trapped in deeper traps or on internal interfaces (which are present, in practical, prevailingly on CR materials). This deep charge can be depleted only after that injected in the positive half-period, which probably is located close to the surface or in shallower traps.

The slope of the first transient of depolarisation characteristic can be evaluated through Figs. 6.35B and 6.38B, which restrict the characteristics plotting only the first four seconds. As explained above, only surface-trapped charge is extracted at the beginning of depolarisation (since charge is trapped prevailingly at the electrode-insulation interface under AC). Among CR materials, #C and #B show a larger slope, i.e. 4.8 and 4.4, respectively, while that relevant to #D is smaller (3.9); conventional material #A is the slowest, having the smallest slope (3.2).

Finally, Fig. 6.39 and Tab. 6.3 summarise the behaviour of trapped charge as function of frequency for bipolar square wave tests. A fast decrease of stored charge with frequency is observable. Contrary to what happens with unipolar waves, at high frequency the stored charge reaches values below the sensitivity of the measuring system. For this reason 10 kHz space charge profiles are not here reported and in Tab. 6.3 the value of Q_M relevant to these tests is generically indicated as < 0.5 C/m^3.

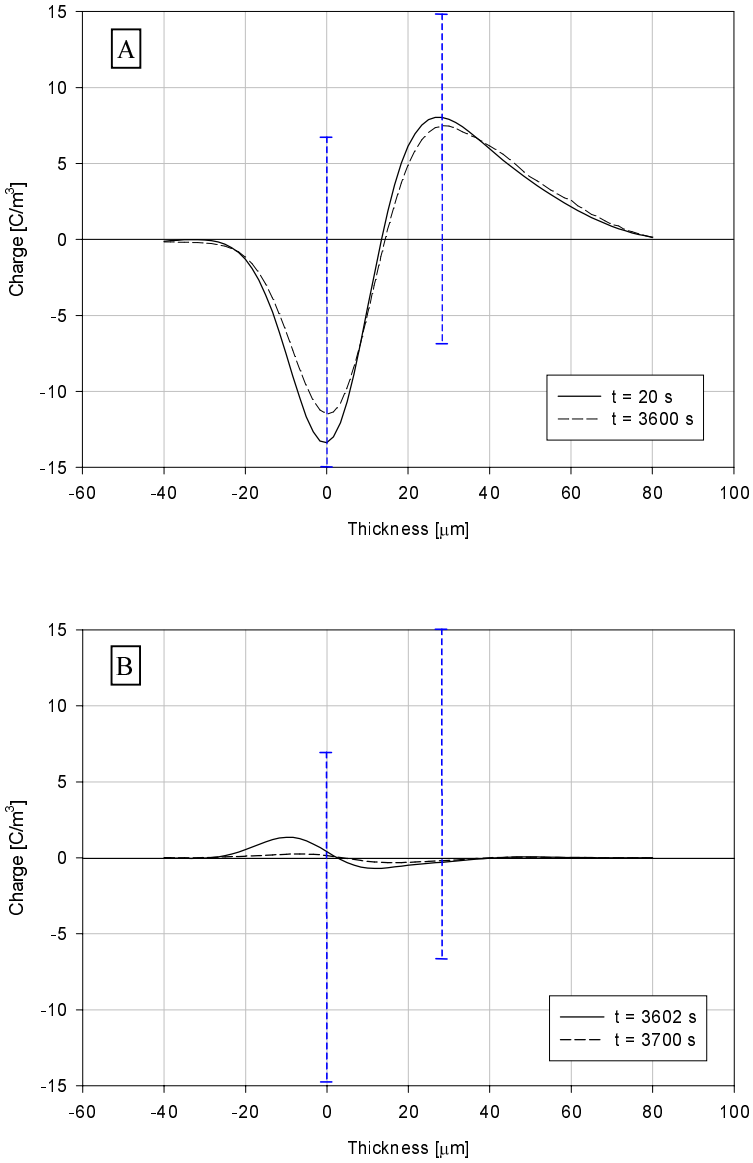

Fig. 6.33: Space charge profiles during polarisation (A) and depolarisation (B). Material #A. Poling voltage squarewave bipolar 0.1 Hz, 1 kV peak.

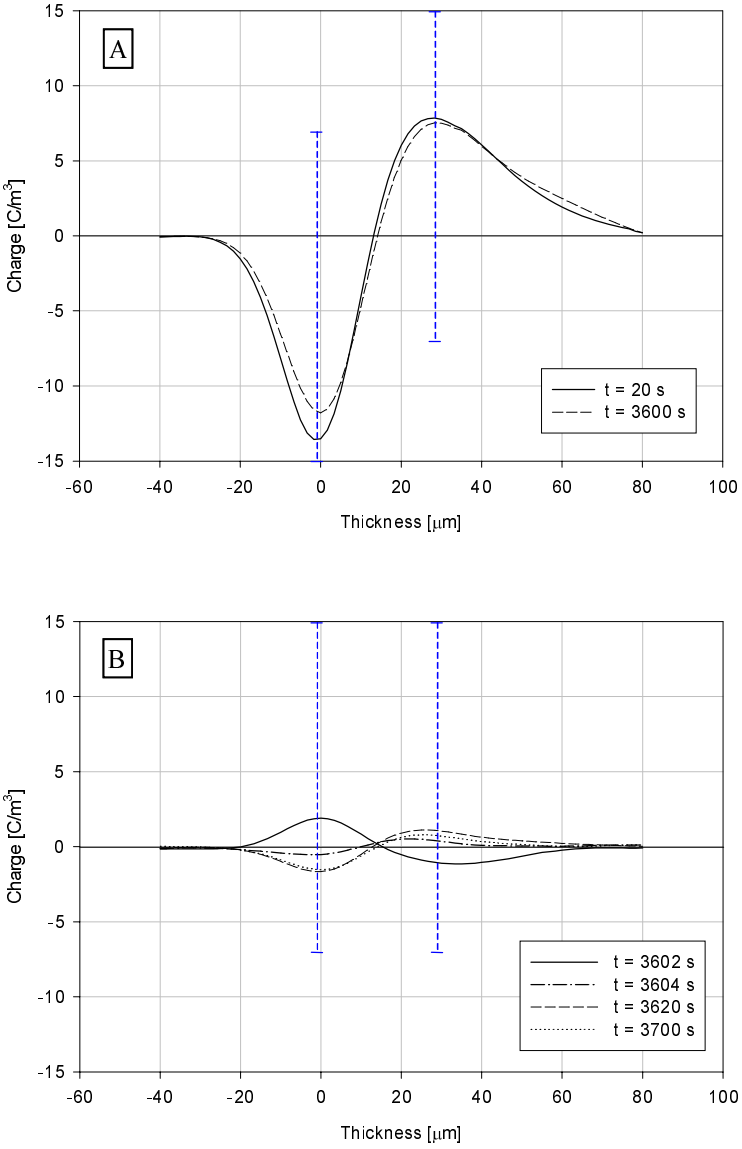

Fig. 6.34: Space charge profiles during polarisation (A) and depolarisation (B). Material #C. Poling voltage squarewave bipolar 0.1 Hz, 1 kV peak.

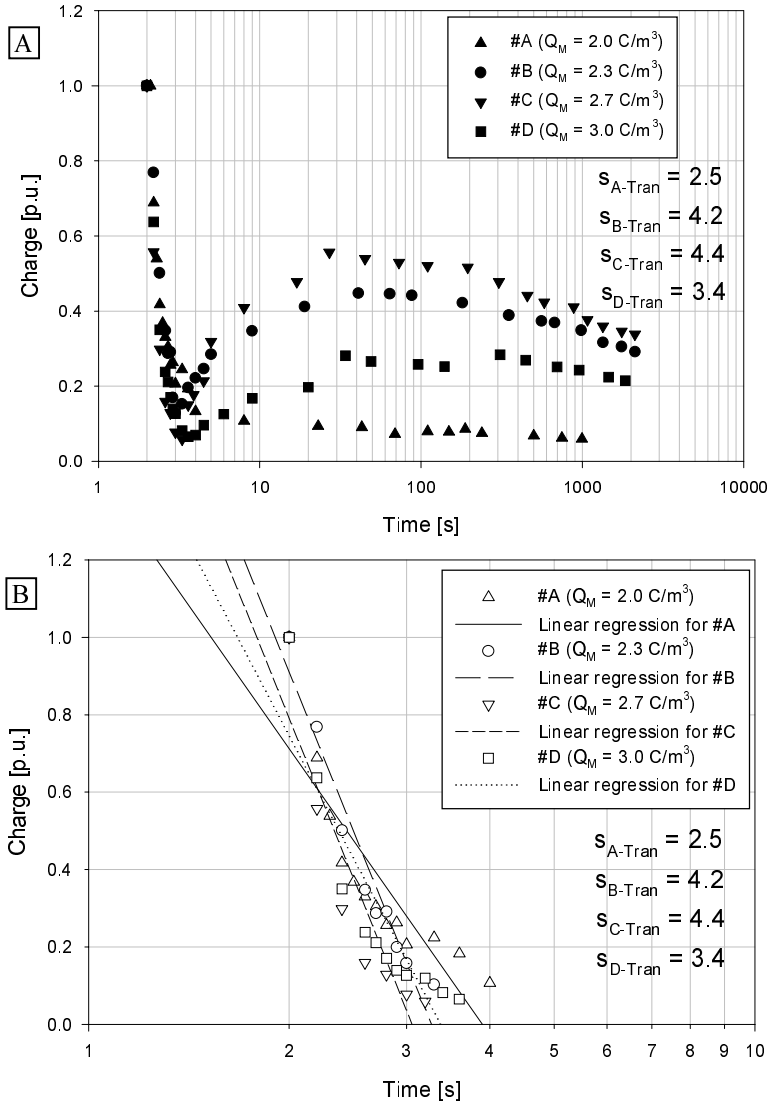

Fig. 6.35: Depolarisation characteristics for #A, #B, #C and #D: entire acquisition (A) and first part, up to 4 s after volt-off (B). Poling voltage: 0.1 Hz square bipolar. The slope of the regression line, *s*, is also indicated.

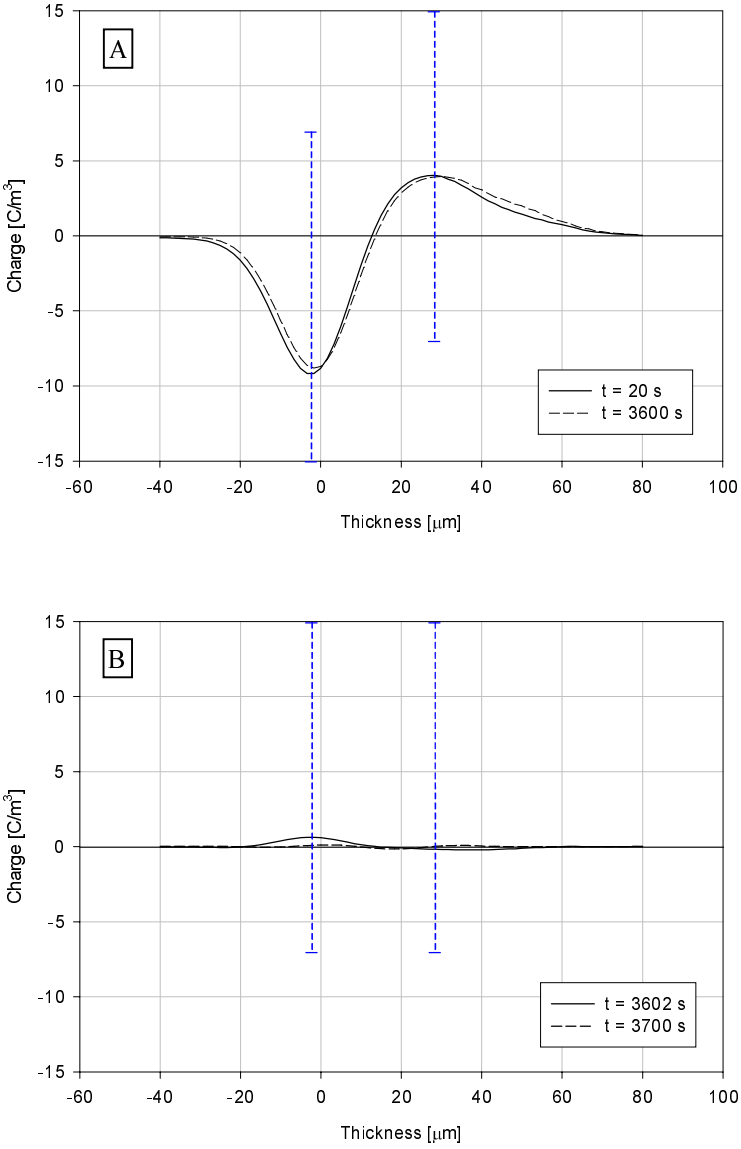

Fig. 6.36: Space charge profiles during polarisation (A) and depolarisation (B). Material #A. Poling voltage squarewave bipolar 50 Hz, 1 kV peak.

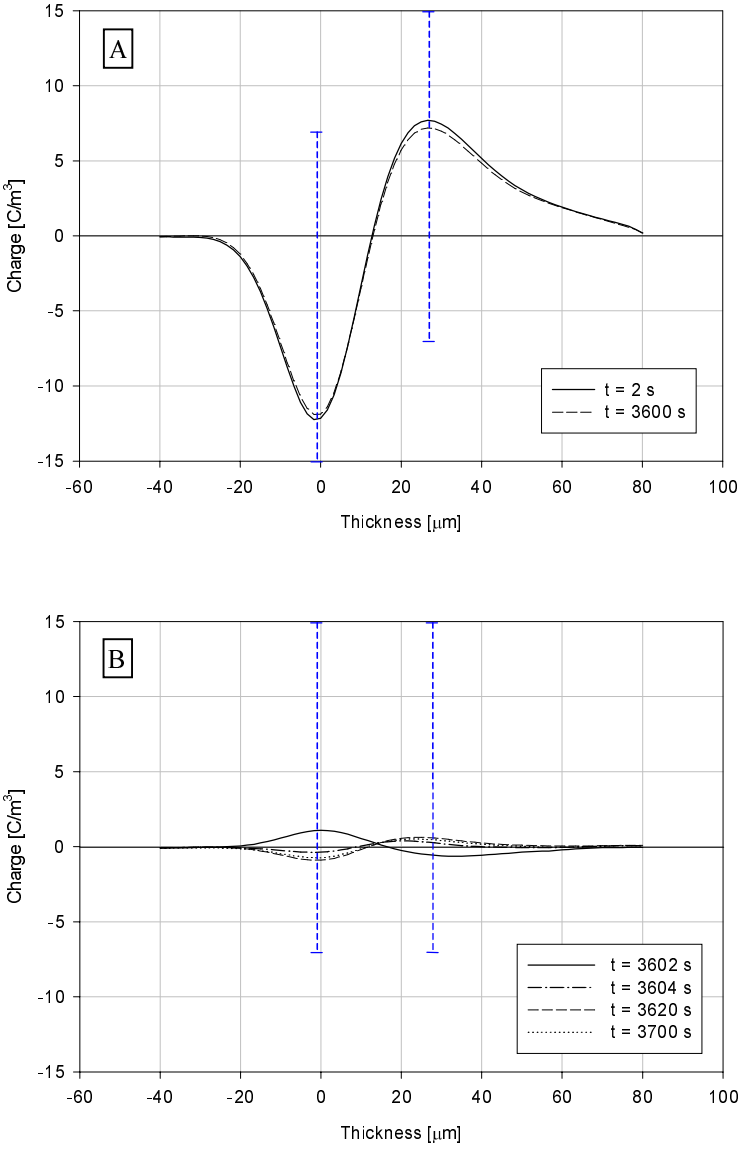

Fig. 6.37: Space charge profiles during polarisation (A) and depolarisation (B). Material #C. Poling voltage squarewave bipolar 50 Hz, 1 kV peak.

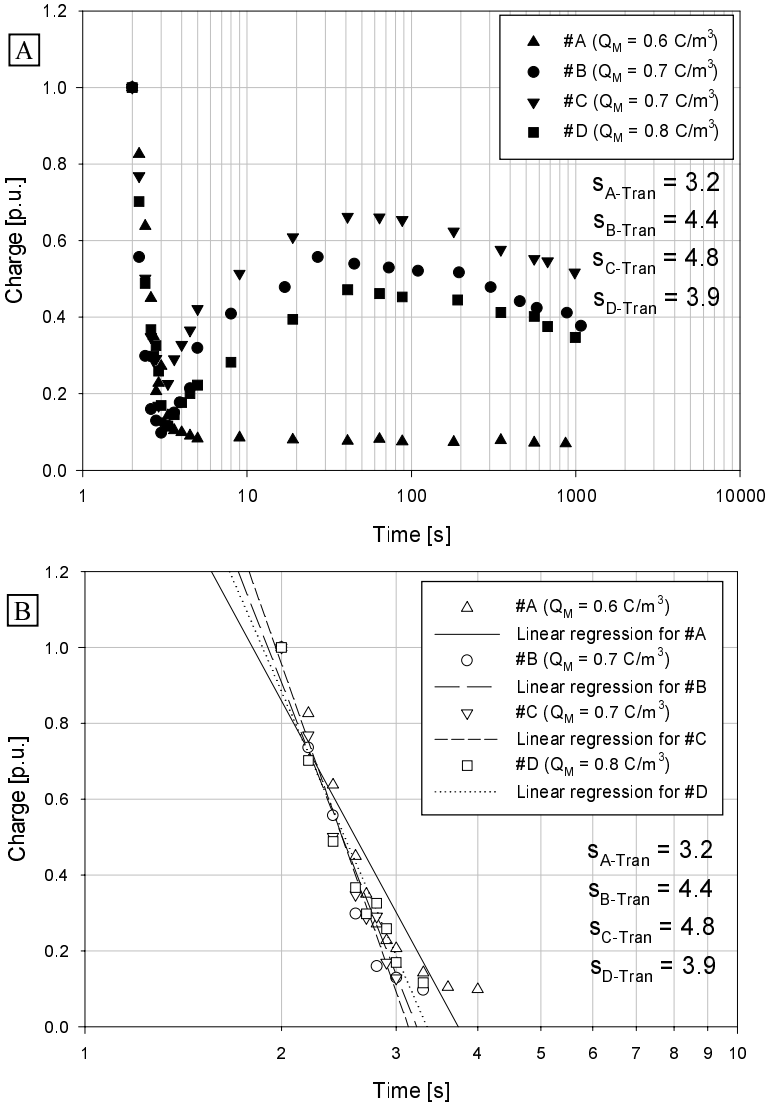

Fig. 6.35: Depolarisation characteristics for #A, #B, #C and #D: entire acquisition (A) and first part, up to 4 s after volt-off (B). Poling voltage: 50 Hz square bipolar. The slope of the regression line, *s*, is also indicated.

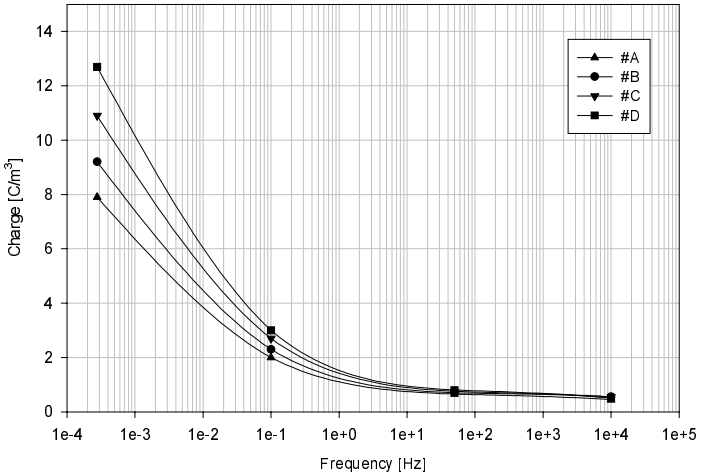

Fig. 6.39: Stored charge density behaviour for #A, #B, #C and #D as function of the voltage frequency. Poling voltage: square bipolar.

Tab. 6.3: Values of space charge quantities Q_M and s calculated for bipolar square waves at different frequencies.

Test	Quantity	Material #A	Material #B	Material #C	Material #D
Bipolar 0.1Hz	Q_m [C/m^3]	2.0	2.3	2.7	3.0
	s_{tran} [s^{-1}]	2.5	4.2	4.4	3.4
Bipolar 50Hz	Q_m [C/m^3]	0.6	0.7	0.7	0.8
	s_{tran} [s^{-1}]	3.2	4.4	4.8	3.9
Bipolar 10kHz	Q_m [C/m^3]	< 0.5	< 0.5	< 0.5	< 0.5
	s_{tran} [s^{-1}]	_	_	_	_

Chapter 7

Discussion on experimental results and comparison with PD measurements

7.1 Premise

Life tests and space charge measurements were performed with the purpose to understand better ageing acceleration of insulating materials under high-frequency pulsed waveforms with respect to the behaviour under 50 Hz sinusoidal supply. Of course, if the problem is to evaluate life performance of insulating materials candidate to be used in enamelled wires, life tests can provide exhaustive information.

However, life tests can hardly explain the reasons why a given material shows failure times longer than another one or provides better endurance. The investigation of some insulation properties through analytical and non-destructive tests (e.g. space charge and partial discharge measurements), and correlation with life performance can provide, in principle, an answer to the above questions, allowing failure mechanisms to be singled out, as well as giving a feedback to material manufacturers about the changes a material must undergo in order to exhibit improved features of endurance and reliability.

Previous chapters, reporting experimental results on enamelled wires, raised several questions, e.g. why some corona resistant materials, like #C, behave better than #A at high frequency while others, like #D, do not show any improvement with respect to #A.

This chapter tries to provide an explanation of insulation behaviour under different supply conditions in the presence of PD, which constitute the main factor accelerating ageing. For this purpose, additional PD measurements were carried out and the results correlated with life tests and space charge measurements, achieving an informative framework for insulation characterisation.

7.2 Striking items

Among the wealth of experimental results shown in the previous chapters, our attention will focus here on the following striking items:

- Space Charge behaviour: accumulation of space charge as a function of waveform and frequency. Enamelled wires seem to accumulate charge under DC and with unipolar waveforms even at high frequency, while under bipolar waveforms space charge accumulation becomes negligible increasing frequency.
- Partial Discharge behaviour: PDIV is almost independent of frequency, but affected by waveform polarity (unipolar, bipolar) and space charge accumulation. PD repetition frequency and amplitude depend on supply frequency and on insulating enamel capability of draining the charge deposited by partial discharge on the insulation surface.
- Life behaviour: peak-to-peak voltage, as well as frequency, is the main factor accelerating ageing; some corona resistant materials (#B, #C) show an improved life performance at high frequency in the presence of PD, while others, as #D, behave worse than material #A.

7.3 Space charge behaviour

Among the effects that can be attributed to space charge accumulation, certainly the most important is electric field modifications, both inside insulation, due to space charge stored in insulation bulk, and outside, in the air gap between two wires, due to charge located on insulation surface.

Space charge accumulation in insulation bulk is a phenomenon which does not occur in the same way changing frequency and with each waveform. Looking at Fig. 7.1, in fact, we can observe that as frequency increases, the total stored charge density becomes smaller in insulation bulk. On one hand, charge injected by each electrode is not effective in travelling inside the insulation under bipolar waveforms if electric field changes polarity rapidly, so that charge remains mainly concentrated in the proximity of the electrodes (already at some tens of Hz, the amount of stored charge is negligible, compared with DC field). On the other hand, if the applied electric field has a DC component, stored charge decreases with frequency but it shows a sort of tendency to a threshold

at high frequency, which corresponds to significant charge accumulation. Hence, even at 10 kHz a considerable amount of space charge in the insulation bulk can be observed.

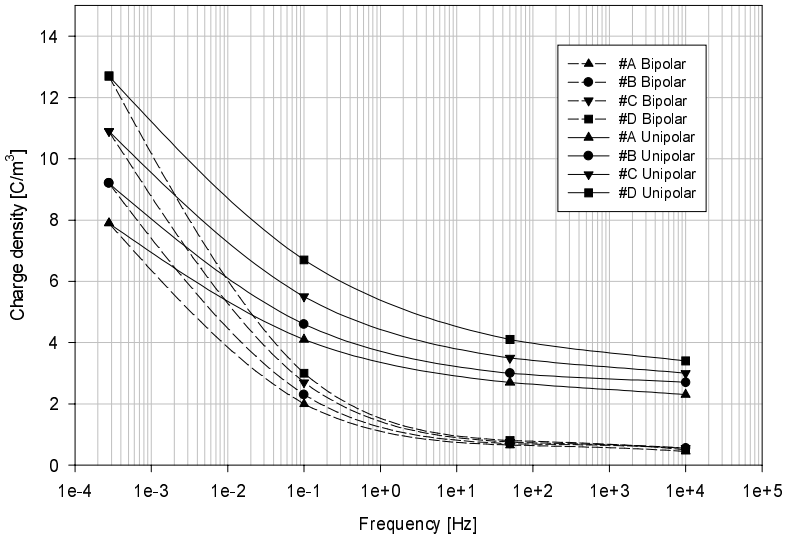

Fig. 7.1: Charge accumulation behaviour with frequency for unipolar and bipolar supply waveforms. Materials #A, #B, #C and #D.

Besides charge injected by the electrode and located in insulation bulk, charge of other nature can affect the insulation/air interface, e.g., coming from interfacial polarisation or partial discharge activity, if any. This charge, as well as that in insulation bulk, can modify the electric field in the air gap.

7.3.1 Electric field modifications due to space charge

Observing that PD activity depends on the electric field in the air gap between two enamelled wire surfaces, e.g. between the adjacent wires of a twisted pair turn, a simplified expression of that electric field can be very useful for further analysis on PD behaviour.

Figure 7.2 shows on the left-side a typical twisted pair and on the right-side the enamel/air/enamel insulation system relevant to zoomed part of one turn (indicated by the rectangle on the left-side figure). On a small scale, the electric field can be calculated as for a plane capacitor with mixed dielectrics.

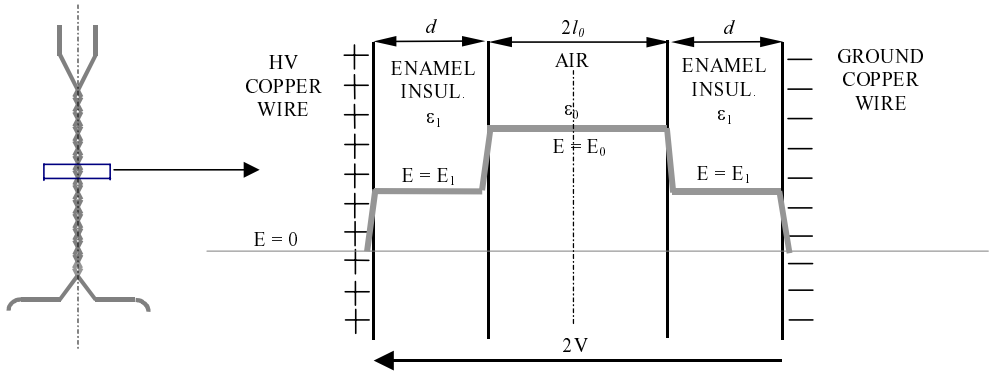

Fig. 7.2: Model describing the insulation system (enamel-air-enamel) between the two wires of a single turn of a twisted pair. The electric field behaviour is also reported (in grey)

Considering the system symmetrical with respect to the axis passing from the middle of the air gap and if no space charge is accumulated in the insulation bulk or on air/insulation interfaces the expression of electric field in the air gap E_0 is given by:

$$E_0 = \frac{V}{\frac{\varepsilon_0}{\varepsilon_1} d + l_0} \tag{7.1}$$

where ε_1 and ε_0 are the dielectric constant of enamel and air, respectively; V is the half of applied voltage; d and l_0 are the enamel insulation and half air gap thickness, respectively.

Since $\varepsilon_1 > \varepsilon_0$ and $E_0 = \frac{\varepsilon_1}{\varepsilon_0} E_1$, where E_1 is the electric field inside insulation bulk, then $E_0 > E_1$ as shown in Fig. 7.2 where the grey thick line represents the electric field behaviour.

It is well known in literature, and it has been proved also in the previous chapter, that space charge accumulation can occur on insulation interfaces, both inside the material and on air gap surface, thus distorting the electric field calculated by eq. (7.1) [100-102].

Indicating with ρ and σ_S the charge per volume unit in insulation bulk and the charge per surface unit on the interface, respectively, electric field E becomes E^* : see Fig. 7.3.

Electric field in insulation bulk follows the relation $divE^* = \frac{\rho}{\varepsilon}$, in regions where charge is present, while $divE^* = 0$ where there is no charge.

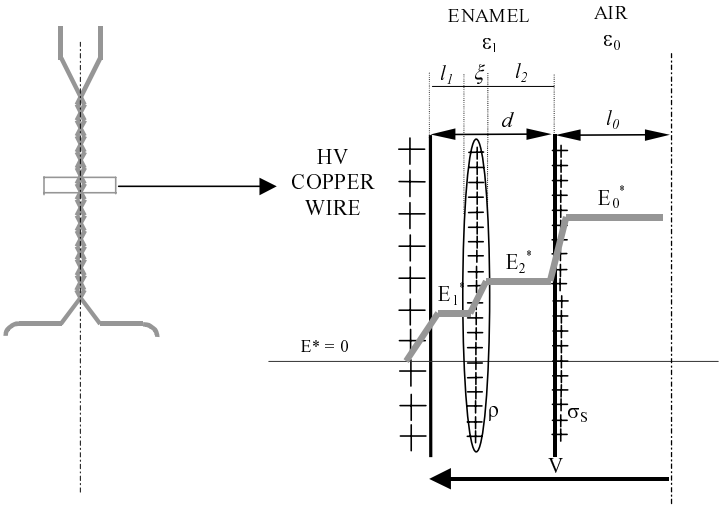

Fig. 7.3: Model of the insulation system reported in Fig. 7.1 with accumulated space charge in insulation bulk and on enamel-air interface. For symmetry reason only the left-half part is considered.

Considering the thickness of the charge distribution, ξ, negligible with respect to insulation thickness, d, a relationship between electric field on the left side and on the right side of the charge distribution E_1^* and E_2^*, respectively, can be obtained as:

$$E_2^* = E_1^* + \frac{\rho\xi}{\varepsilon_1} \tag{7.2}$$

The electric field in the air gap, E_0^*, is related to the charge accumulated on the interface by the following equation:

$$E_0^* = \frac{\varepsilon_1}{\varepsilon_0} E_2^* + \frac{\sigma_S}{\varepsilon_0} \tag{7.3}$$

Considering the system symmetrical with respect to an axis located in the middle of the air gap, it derives that:

$$E_1^* l_1 + E_2^* l_2 + E_0^* l_0 = V \tag{7.4}$$

from which (and from eq. (7.1)) it comes out that:

$$E_0^* = E_0 + \frac{\rho\xi l_1 + \sigma_S d}{\varepsilon_0 d + \varepsilon_1 l_0} \tag{7.5}$$

where E_0 is the electric field previously calculated by eq. (7.1), in the absence of space charge accumulated (ρ and σ_S = 0). The derivation of eq. (7.5) from eq. (7.3) is explained in detail in the Appendix.

It can be argued that if ρ and σ_S have the same polarity of the electrode near which they accumulate, e.g. if E_0>0, ρ and σ_S > 0 near the positive electrode, the resulting electric field E_0^* is magnified with respect to the field without accumulated charge, E_0.

7.3.2 Analysis of trap depth for space charge accumulation

The amount of space charge accumulated by electrode injection in the insulation bulk and/or by PD activity on insulation surface of the air gap between two wires, depends, for a given applied field, on insulating material properties, as the density of charge traps and their depth. This latter is defined as the energy which is needed by an elemental charge to be detrapped up to the conduction band level. Trap depth can be calculated once charge mobility, μ, has been evaluated. As an example, the following simplified expression, can be used [103]:

$$\mu = \frac{2\varepsilon}{q(t)^2}\frac{dq(t)}{dt} \tag{7.6}$$

where $q(t)$ is the total absolute stored charge density measured at time t during depolarisation phase. It can be provided by depolarisation characteristics obtained from space charge measurements, reported in the previous chapter.

Figure 7.4 shows, roughly, an array of trap levels which are identified by their potential energy U_i (i=1,..., m) and are spaced by kT (k = Boltzmann constant, T = temperature); m is total number of levels, with potential energy decreasing from level 1 to level m, N_i represents the maximum number density of charge available at that level.

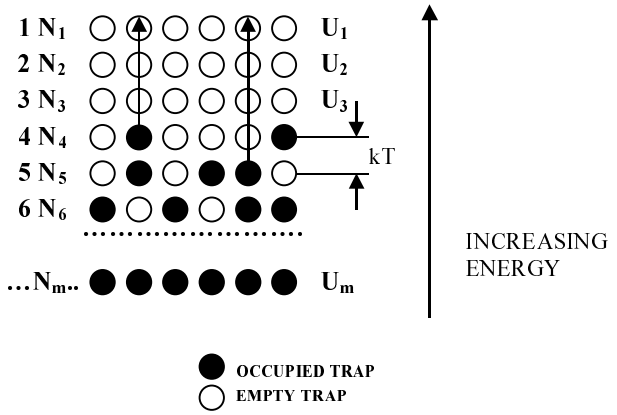

Fig. 7.4: Trap model of insulating materials.

If the specimen is uncharged, at equilibrium, the rate at which charge is promoted to the top level is equal to the rate at which it falls back into lower levels, thus at steady-state the charge distribution results in a Fermi-Dirac distribution [104]. If the specimen is charged, on the contrary, short-circuiting the electrodes trapped charges are forced to escape from their localised states, starting from shallower traps, then going on with deeper and deeper traps.

The number of charges trapped in the specimens at time t can be calculated by [103]:

$$n_{TOT}(t) = \sum_{i=2}^{m} n_i(t) = \sum_{i=2}^{m} a_i \exp(-b_i t) \qquad (7.7)$$

where:

$n_i(t)$ is the charge present in the ith trap level at time t:

$$a_i = n_i(0);$$

$$b_i = \nu \exp\left(\frac{\Delta U_i}{kT}\right);$$

$$\Delta U_i = U_i - U_1;$$

$\nu = kT/h$, is the escape frequency (that can be assumed, for example equal to $6.108 \cdot 10^{12}$ Hz according with [105];

$h = 6.62 \cdot 10^{-34}$ J·s, is the Planck constant.

It is noteworthy that the rate equation governing the discharge from the i^{th} level has of identical form to that for a discharging series capacitor and resistor, with relaxation time given by [105]

$$\tau_i = \frac{1}{\nu \exp\left(\frac{\Delta U_i}{kT}\right)} \tag{7.8}$$

The evaluation of trap depth ΔU_i from eq. (7.7) can be very difficult, thus a simplified expression can be preferable for this purpose. The trap depth of i^{th} level, ΔU_i (in Joule), can be calculated, for example, by means of the following relation which involves charge mobility (evaluated through eq. (7.6)) [106]:

$$\Delta U_i = kT \ln\left(\mu \frac{kT}{\nu e R^2}\right) \tag{7.9}$$

where: $R = 5\text{x}10^{-7}$ m, is the mean distance between localised states; $k = 1.38 \cdot 10^{-23}$ J/K the Boltzman constant; $e = 1.6 \cdot 10^{-19}$ C, the electron charge, $T = 293$ K, the room temperature.

Equation (7.6) can be applied to DC depolarisation characteristics of Fig. 6.11, in order to evaluate the mobility of charge injected by the electrodes and accumulated in insulation bulk, which can be significant only under poling field with a DC component (DC or AC-unipolar voltage). The results are plotted in Fig. 7.5 (with reference to depolarisation characteristics starting 2 s after volt-off). Trap depth, calculated through eq. (7.9) and reported in Fig. 7.6, shows the same behaviour of mobility. As a function of depolarisation time, trap depth increases significantly, in absolute value, for each material, since first shallower traps becomes empty (contributing to conduction) and then deeper traps eject charges. Among the four materials, #A shows the largest mobility, i.e. shallower traps contributing to charge accumulation, while #B and #C have trap depth values quite close to #A (about -0.82 eV for #A, -0.83 eV for #B and #C at depolarisation time of 2 s). Material #D, on the contrary, exhibits the smallest mobility and the largest trap depth (about -0.87 eV at 2 s). Note that large variations of mobility produce only small variations of trap depth energy, since the relation between these two quantities is logarithmic (see eq. (7.9)).

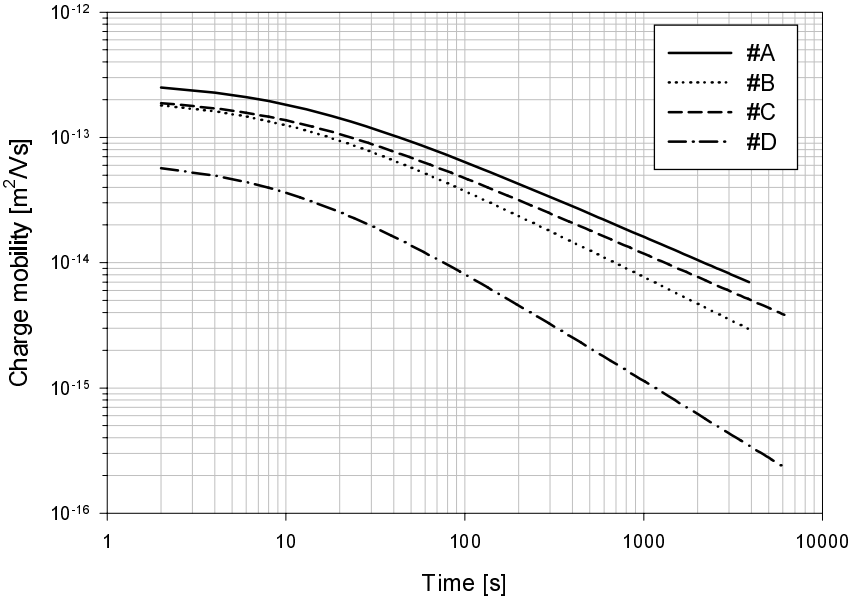

Fig. 7.5: Charge mobility for the four tested materials. DC poling field = 35 kV/mm.

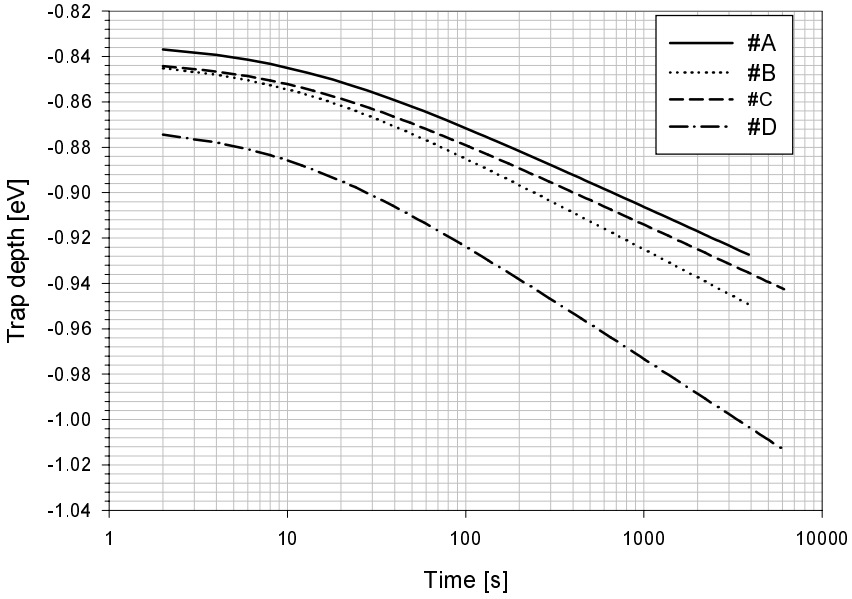

Fig. 7.6: Trap depth relevant obtained from charge mobility reported in Fig. 7.5

We can apply equations (7.6) and (7.9) also to AC depolarisation characteristics, e.g. those of Fig. 6.35 relevant to 50 Hz bipolar

squarewave poling field, obtaining values of mobility and trap depth different from those reported above. In this case, however, charge injected at one half period is then recombined with charge of opposite sign injected at the following half period, so that accumulated charge, if any, remains mainly localised near the electrodes. Hence, injection and extraction times predominate with respect to trapping-detrapping from deep traps, charges populate shallow traps and equations (7.6)-(7.9) (based on the assumption that transport times are larger than injection-extraction times) may be significantly inaccurate. However, at a first, rough evaluation based on (7.6) and (7.9) material #D presents again the lowest mobility, see Table 7.1.

Tab.7.1: Approximate evaluation of mean values of mobility and trap depth relevant to 50 Hz bipolar squarewave tests.

Material	#A	#B	#C	#D
Mobility [m^2/Vs]	$3.4 \cdot 10^{-10}$	$7.7 \cdot 10^{-10}$	$6.0 \cdot 10^{-10}$	$2.9 \cdot 10^{-10}$
Trap depth [eV]	0.66	0.64	0.64	0.67

These results show that trap depth values which can be evaluated by the space charge measurements here performed are mainly relevant to chemical traps, with energy ranging from 0.7 to 1 eV, which are quite deep, while physical ones (like, e.g., those due to imperfections or dishomogeneity on the material surface) show values of about 0.1-0.5 eV [107]. These traps can be hardly revealed by the PEA space charge technique described above, but can be evaluated, for example, through conductivity measurements. Materials which exhibit a larger conduction current have larger density of shallow traps with smaller trap depth contributing to conduction. These observation will be better discussed in next section which deals with partial discharge behaviour of insulating materials used for enamelled wires.

7.4 Partial Discharge behaviour

We saw in previous chapters that partial discharges represent the main factor accelerating insulation degradation. The electric field in the air gap between two wires which promotes PD activity is largely affected by charge which accumulate in insulation (bulk and interfaces), see eq. (7.5). Therefore the investigation of space charge effect on PD features (PDIV, PD amplitude, repetition rate, etc.) should explain some

of the items raised.

7.4.1 Effect of space charge accumulation on PDIV

Considering ρ = 0, i.e. no space charge accumulated in insulation bulk, (e.g. perfectly homogeneous dielectrics), if charge is present only on insulation surface, eq. (7.5) simplifies to:

$$E_0^* = E_0 + \frac{\sigma_S d}{\varepsilon_0 d + \varepsilon\, l_0} \tag{7.10}$$

In particular, the nature of σ_S can be related to charge trapping at interface (or interfacial polarisation), if supply voltage has a DC component or for bipolar waveforms at very low frequency (<1 Hz). Interfacial polarisation can occur, in fact, if two dielectrics with different conductivity, γ_1 and γ_2, and dielectric constant, ε_1 and ε_2, are put in contact. In our case let γ_1, ε_1 be the electrical conductivity and the dielectric constant relevant to enamel insulation, while γ_0, ε_0 are those relevant to air, D_0 and J_0 the normal components of dielectric induction and current density vectors in air, respectively, D_1 and J_1 are relevant to enamel insulation. From Maxwell equations it can be written, in the presence of a discontinuity surface:

$$D_0^* - D_1^* = \sigma_S \tag{7.11}$$

$$J_0^* - J_1^* = -\frac{\partial \sigma_S}{\partial t} \tag{7.12}$$

Since $D = \varepsilon E$ and $J = \gamma E$, then

$$\varepsilon_0 E_0^* - \varepsilon_1 E_1^* = \sigma_S \tag{7.13}$$

$$\gamma_0 E_0^* - \gamma_1 E_1^* = -\frac{\partial \sigma_S}{\partial t} \tag{7.14}$$

Substituting (7.10) in (7.9) we obtain:

$$\frac{\partial \sigma_S}{\partial t} + \frac{\gamma_1}{\varepsilon_1}\sigma_S = \left(\frac{\varepsilon_0 \gamma_1}{\varepsilon_1} - \gamma_0\right) E_0^* \tag{7.15}$$

Finally, the extent of interfacial charge density can be obtained by eq. (7.11) at steady state:

$$\sigma_S = E_0^*(\varepsilon_0 - \varepsilon_1 \frac{\gamma_0}{\gamma_1}) \tag{7.16}$$

Substituting (7.16) in (7.10) we obtain the electric field expression in the presence of interfacial charge:

$$E_0^* = \frac{E_0}{1 - \dfrac{\varepsilon_0 - \varepsilon_1 \dfrac{\gamma_0}{\gamma_1}}{\varepsilon_0 + \varepsilon_1 \dfrac{l_0}{d}}} \tag{7.17}$$

Usually, being $\varepsilon > \varepsilon_0$ and $\gamma_0 >> \gamma$, then $(\varepsilon_0 - \varepsilon \frac{\gamma_0}{\gamma}) < 0$, and so that σ_S has opposite sign with respect to E_0^*. Therefore, interfacial charge tends to reduce the electric field in the air gap, increasing, consequently, partial discharge inception voltage.

On the other hand, space charge measurements showed that charge accumulates in insulation bulk, when supply waveforms have a DC component, as it occurs for unipolar waves or for alternate waveforms at low frequency. In some materials (as those here investigated, see Chapter 6) charge is mainly injected by the electrodes, so that accumulated charge has the same polarity of the injecting electrode (homocharge), e.g. $\rho > 0$ near the positive electrode, (cfr. §§ 7.6.2-7.6.6). According to eq. (7.5), this leads to an increase of electric field in the air gap between the two wires and, thus, to a PDIV decrease.

Interfacial polarisation and charge accumulation in the insulation bulk may play, hence, an opposite role on PDIV (the former increasing, the latter decreasing PDIV) showing their effect, with different time constant, when poling voltage is applied.

These deductions were experimentally verified performing PDIV measurements, at different times, on twisted pairs stressed with 50 Hz unipolar square waves having amplitude of 0.5 PDIV. The results relevant to material #C are collected in Fig. 7.7. It can be seen that PDIV shows an increase in the first half an hour of poling, due to the contrasting contribution of interfacial polarisation and homocharge accumulation (see Chapter 6). At longer times a small decrease, then a stabilisation of PDIV, is observed, likely due to the prevailing effect of space charge accumulation in insulation bulk. Electric field reduction

due to interfacial charge was observed previously by Takada et. al. in composite insulation systems [102].

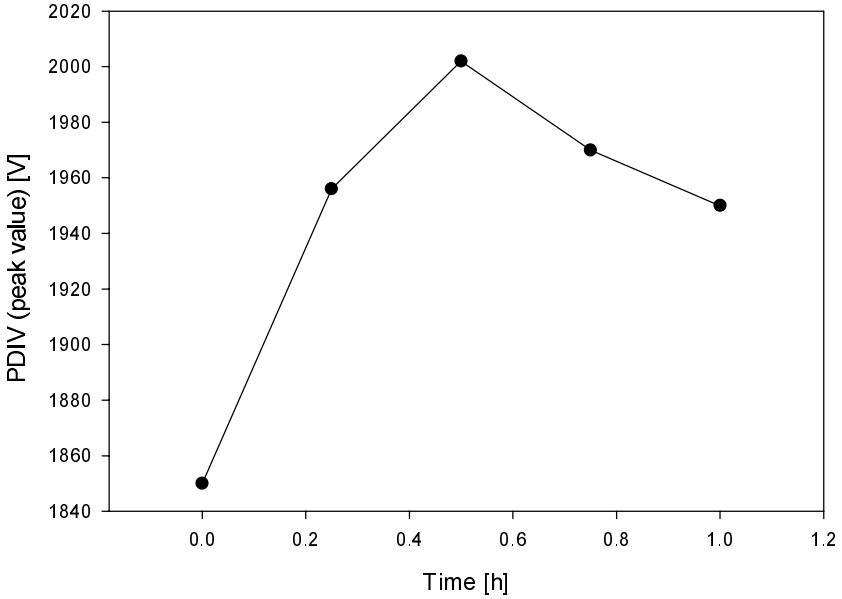

Fig. 7.7: Behaviour of PDIV with poling time with unipolar square wave at 50 Hz.

On the contrary, if specimens are poled with bipolar waveforms PDIV is quite independent of poling time, since very small charge accumulation can be observed in insulation bulk and on the surface, in short times.

The behaviour of PDIV with waveform type and frequency is reported in Fig. 7.8, which summarises the PDIV measured at 50 Hz under sinusoidal and square waves (unipolar and bipolar), as well as with 1 kHz and 10 kHz squarewaves (unipolar and bipolar). It is interesting to observe that PDIV measured under bipolar waveforms (sinusoidal or squarewave) is almost the same for a given material independently of the frequency, i.e. about 800 V, 850 V, 900 V and 800 V (peak value) for #A, #B, #C and #D, respectively (this may be due to the quite low rate of voltage increase used for PDIV estimation, as well as to the relatively low dV/dt of the square waveforms).

It is noteworthy that PDIV is more than doubled under unipolar squarewaves, about 1900 V and 2000 V for #B and #C, respectively, 1700V for #A and #D, which leads to argue that PDIV depends mainly on peak-to-peak value of the applied voltage.

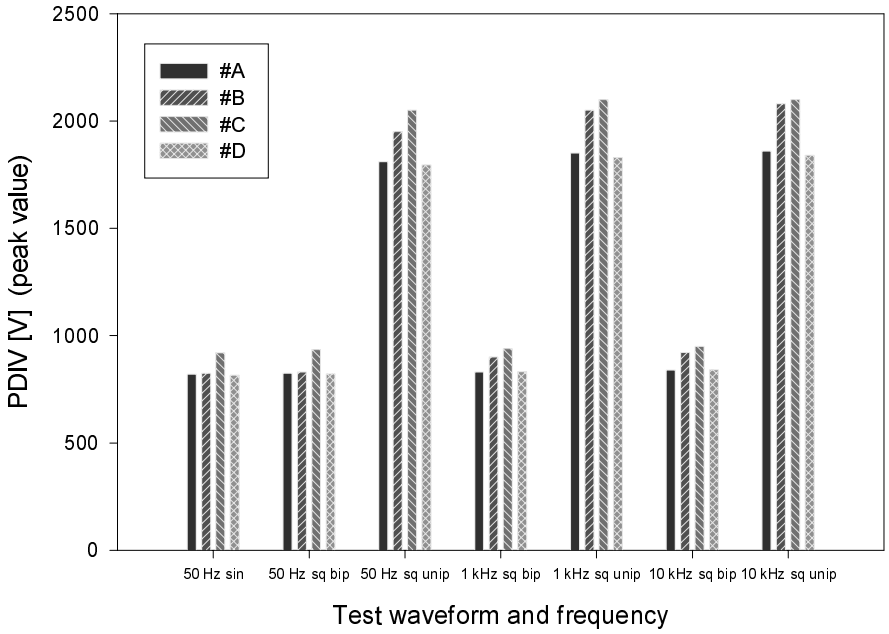

Fig. 7.8: Behaviour of PDIV (peak value) with test waveform and frequency for the four tested materials.

This fact can be explained resorting to the following considerations. Figure 7.9 shows the air gap before and after a PD occurrence. Before PD activity the electric field in the air gap is equal to the external field $E_0(t)$. When a PD occurs an ethero-space-charge is accumulated on the enamel surface (in light grey) generating field E_{SC} in opposition to $E_0(t)$,which reduces the electric field in the air gap to the value $E_0^*(t) = E_{res}$ (in dark grey), according to equation (7.10) with $\sigma_S < 0$.

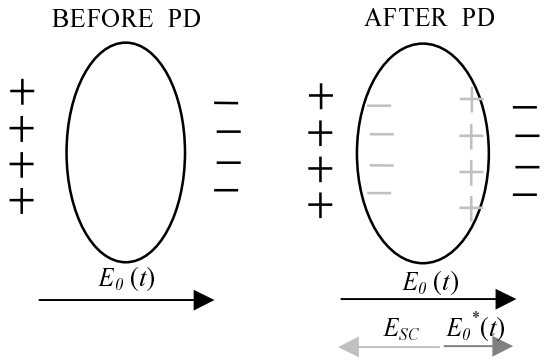

Fig. 7.9: Electric field before and after PD and electric field modifications due to the deposited charge.

If charge coming from a PD does not recombine, the opposite electric filed E_{SC} would prevent another discharge to occur, until external electric field variation could change the field in the air gap, giving rise to the conditions for any other discharge.

Under bipolar and unipolar waveforms the discharge sequence is different. Figure 7.10 reports the behaviour of the field in the air gap between the two wires $E_0^*(t)$, before and after PD for bipolar (A) and unipolar square voltage (B). For bipolar waves (with peak voltage E_P), before PD occurrence electric field E_0^* (in grey) is equal to applied field E_0 (in black). If the PDIV is reached, after a certain statistical time delay needed to get starting electrons, a discharge occurs, dropping the electric field E_0^* to the value E_{res}, as previously explained in Fig. 7.9. If ignited charge is not drained away fast, i.e. E_{SC} remains quite constant, when the external field changes its polarity the field in the air gap E_0^* increases negatively with an excursion given by the peak-to-peak field ($=2E_p$). The peak value reached in this way, equal to ($2E_p$ - E_{res}), is larger than PD inception field, thus promoting another discharge which drops the field E_0^* to the value $-E_{res}$ and then, at next field inversion, the same phenomenon occurs. The electric field E_{SC} which decreases the field in the air gap after each discharge takes the same direction of the external field, reinforcing it, at each voltage inversion. Note that the passage from positive to negative peak (peak-to-peak electric field) is the premise for a PD occurrence, as observed also by Busch, Pohlmann and Muller [100].

Under unipolar voltage, on the contrary, in order to have a permanent state of PD activity above PD inception level, the peak value of the external field must be, at least, doubled (i.e. $2E_P$), since the same variation from negative to positive peak is needed for next PD occurrence. When a PD has occurred the field E_0^* is reduced to the value E_{res} until external field decreases to zero. In such a way, E_0^* follows the external field behaviour and when the excursion has reached the value $2E_P$ another discharge is possible even if the applied external voltage is zero (in this case, the electric field in the air gap is given by the space charge field E_{SC}). Therefore, it is quite clear that peak-to-peak voltage is the factor governing PD activity, so that PDIV for unipolar waveforms must be at least doubled with respect to bipolar waveforms.

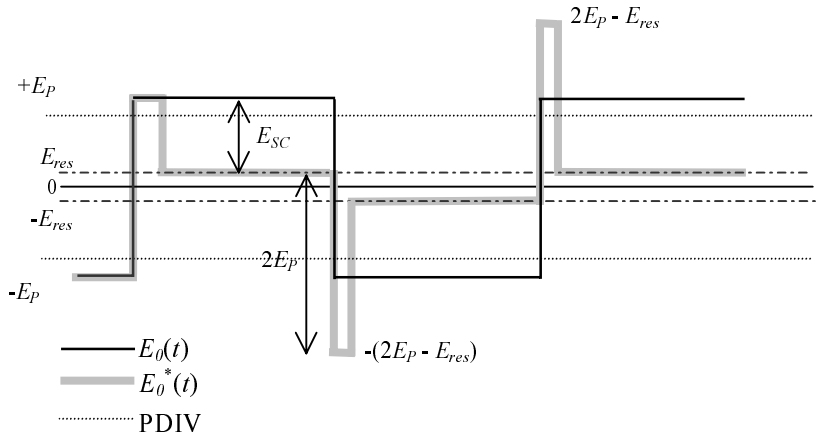

A: BIPOLAR

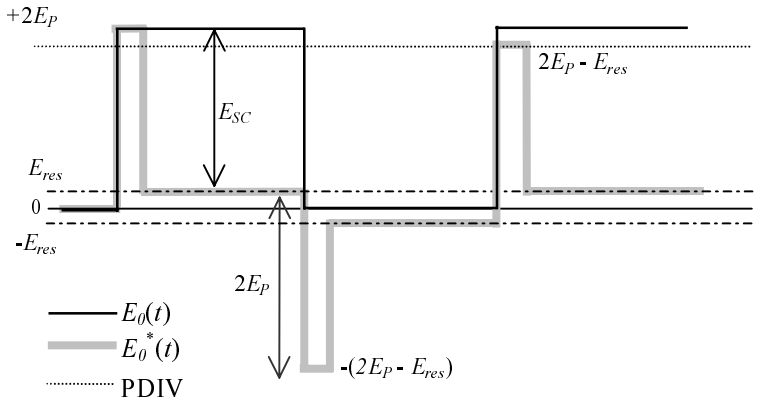

B: UNIPOLAR

Fig. 7.10: Behaviour of electric field in the air gap E_0^* with bipolar (A) and unipolar square waves.

The effect of voltage waveform on PD activity is pointed out clearly in Fig. 7.11 which reports the patterns and the PD pulse shape for material #C at 50 Hz, 1.8 kV (peak-to-ground), i.e. about two times the PDIV, relevant to sinusoidal wave (7.11A), bipolar (7.11B) and unipolar (7.11C) squarewaves. Looking at Fig. 7.11A, it can be observed that the PD activity is concentrated along the rise front of the sinusoidal waveform. With bipolar squarewave (Fig. 7.11B) a large amount of discharges are located in correspondence of the fast rise fronts, but several other small discharges are spanned along the waveform flat. With unipolar waveform (Fig. 7.11C) only few discharges can be

observed, but they are characterised by large amplitude. An example of PD pulses for each test waveform is also reported in Fig. 7.11. These pulses do not differ significantly, meaning that the discharge phenomenon is the same under each test condition. It is noteworthy that, in the case of unipolar square waveform, PD are distributed in the positive voltage half-wave, due to scatter in the availability of ignition electrons (the same holds for bipolar square and sinusoidal waveforms, even if each commutation creates the most likely conditions for PD injection: see Fig. 7.10).

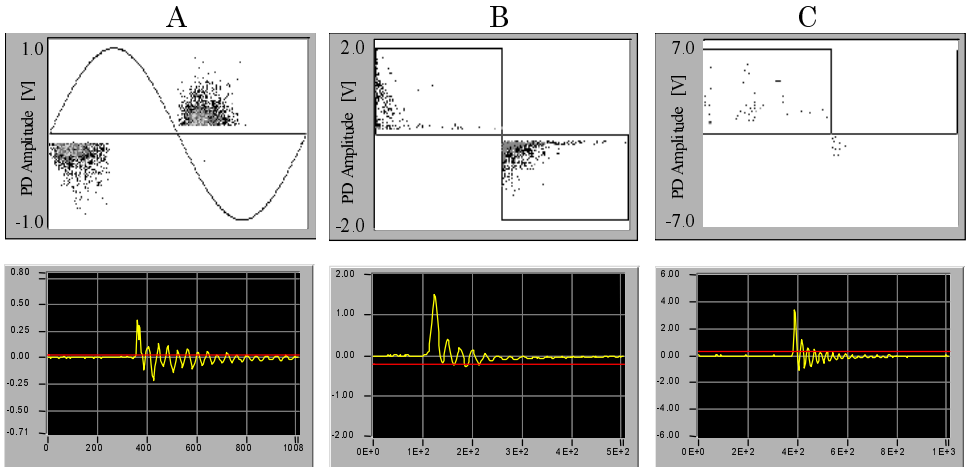

Fig. 7.11: PD patterns and pulse shape recorded at 50 Hz, 1.8 kV (peak value) with sinusoidal (A), bipolar (B) and unipolar (C) square waveforms. Material #C.

As long as E_{SC} is constant, at each voltage polarity inversion the field in the air gap shows the same direction of the applied field amplifying it, thus promoting very large discharges. If a material has the capability to deplete charge rapidly, E_{SC} decreases with time and so does PD amplitude at each voltage inversion, even if the number of discharge per period, may increase. If $E_{SC} = 0$ before a polarity change, in fact, there is the condition for another PD occurrence.

Some PD measurements just around PDIV were carried out on three of the tested materials, i.e. #A, #C and #D. Measurements were performed with the twisted pair immersed in silicon oil, leaving outside only the upper section (about 1 turn), in order to have only one source of PD (when the specimen is left completely in air, several sources on the whole length can produce PD activity, and this could be misleading for our investigations). The results of PD measurements carried out with

square waveforms in the frequency range 1Hz - 10kHz at PDIV are reported in Fig. 7.12. Figure 7.12A shows PD mean amplitude as a function of frequency for materials #A, #C and #D, while Fig. 7.12B reports PD inception delay time, i.e. the time elapsed from a polarity inversion to the PD inception.

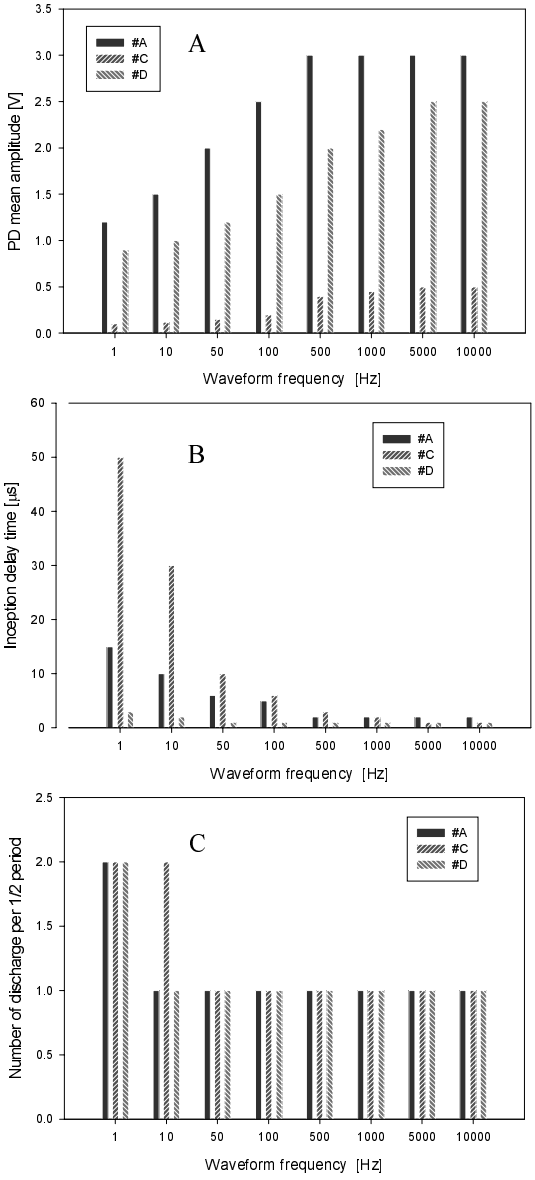

Fig. 7.12 – PD mean amplitude, in V (A), inception delay time (B), number of discharges per half-period as a function of frequency (test waveform: bipolar square, voltage amplitude =PDIV). Materials #A, #C and #D.

The following observations can be drawn:

1) PD amplitude rises for each material increasing supply frequency (with saturation effect above 500 Hz).
2) PD inception delay time increases, especially for #C decreasing supply frequency.
3) Only one discharge per half-period is observable, generally in correspondence of voltage polarity change, at frequencies above 50 Hz. At very low frequencies, multiple discharge per period can occur (in this case E_{SC} may have time to decrease): at 10 Hz two discharges for each half-period are observable for material #C while for #A and #D frequency has to be further on decreased down to 1 Hz to observe at least two discharges.

The observations reported above confirm that space charge accumulated after each PD can affect PD amplitude, delay time and repetition rate. Increasing frequency, field E_{SC} has not enough time to decrease before polarity reversal, thus magnifying the overall field after inversion and, consequently, the amplitude of PD, which occurs immediately after voltage polarity change (PD occur, hence, only after inversions, at times depending on ignition electron delay, but very close to inversions). This happens especially for materials which have less capability to drain out charge, such as #D. Materials faster in charge decay, as #C, on the contrary, can experience repetitive PD per half-period (e.g. two discharges for material #C). Moreover, internal field after inversion is lower than in the previous case, which favours PD delay.

Another important observation that can be done is that PD amplitude for material #C is about one order of magnitude less than those relevant to #A and #D, also at high frequency. This fact cannot be explained resorting to the different mobility showed by the three materials, because the investigation made resorting to space charge measurements is able to reveal trap depth distribution only for deep traps, which cannot be filled and emptied efficiently at those frequencies.

Hence, considering that the differences among these materials might be related to shallow trap depths, some surface conductivity measurements were performed. Conductivity results were about $3.6 \cdot 10^{-10}$ S/m for #A, $7.2 \cdot 10^{-10}$ S/m for #C e $4.2 \cdot 10^{-10}$ S/m for #D.

Increasing surface conductivity, the amount of charge available for each discharge is reduced. Figure 7.13 shows an equivalent circuit,

where traps with different depths are represented by R-C series, according to eq. (7.8) and the conductance G accounts for surface conductivity of enamel insulation (for which the time constant τ is close to zero, thus, is neglected). If G is large, the surface discharging current on wire enamel rises, decreasing the charge on capacitance C (which represents the air gap), the electric field in the air gap and, thus, PD amplitude.

Materials with larger conductivity should show, therefore, smaller PD magnitude, as shown, indeed, by #C (Fig. 7.12) . In order to have a further confirmation, the conductivity of material #D, which is slightly larger than that of #A but significantly smaller than that of #C, was varied moistening slightly the surface with salt water.

The conductivity was about triplicated and the amplitude of the discharges decreased of one order of magnitude.

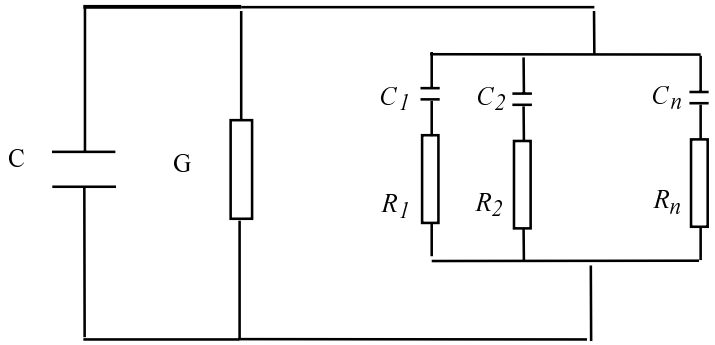

Fig. 7.13: equivalent circuit for trap distribution of enamel material at the surface of the magnet wire.

The behaviour of PD activity as a function of test voltage is shown in Figure 7.14, where PD patterns are reported for #C at 10 kHz bipolar squarewaves and three different voltage levels, i.e. at PD inception (PDIV), 1.5 PDIV and 2 PDIV (note that the tests relevant to the figure were performed on twisted pairs entirely in air, so that multiple PD sources can occur more and more likely increasing voltage). As can be seen, PD are concentrated only at the voltage rise front if voltage amplitude is close to PDIV (Fig. 7.14A). This is confirmed by the large value of the Weibull shape parameter β (5.7 and 6.5 for the positive and the negative discharges, respectively). When the voltage amplitude increases (Fig. 7.14B), partial discharges raise their number significantly, covering the whole phase interval. If voltage is further on increased (Fig. 7.14C), very large PD appear, broadly distributed in

each half period. The Weibull shape parameter β decreases significantly when the amplitude of the applied voltage increases, meaning that discharges are not concentrated in a narrow phase interval, but they are scattered along the voltage period. Visual inspection of the specimen under test shows that discharges are present on the whole specimen surface at voltages exceeding considerably PDIV. Partial discharges seem to change their nature increasing voltage, starting as localised corona in some weak points (at PDIV) and then acquiring a significant surface component at increased voltage.

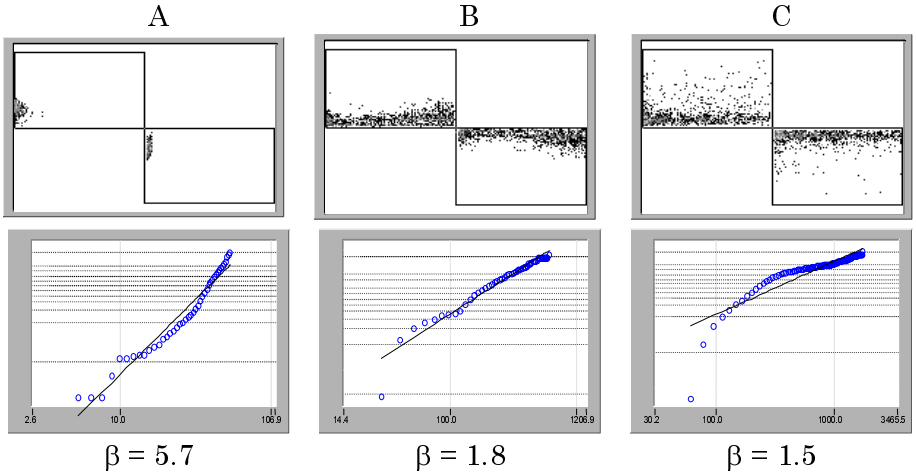

Fig. 7.14 - PD patterns and Weibull distributions of PD heights recorded at 10 kHz bipolar squarewave, increasing the voltage amplitude from PDIV (A) to 1.5 PDIV (B) and 2 PDIV (C). The values of the Weibull parameter β are also indicated for positive discharges. Material #C.

7.5 Life behaviour

We saw in the chapter 5 that factors affecting insulation degradation under high frequency waveforms (sinusoidal, unipolar and bipolar square) are repetition frequency and peak to peak voltage. In particular, different waveforms with the same peak to peak voltage (at a given frequency) seem to have the same effect on ageing, at least for waveforms with rise front < 5 kV/μs. In effect, it was pointed out in the previous section that PDIV and PD activity, in general, depend on voltage variations from negative to positive peak. Since PD activity is the main factor accelerating degradation of enamelled wire, peak-to-

peak voltage assumes a very important role as ageing mechanism. Repetition frequency is important as well, since the number of PD, for a given time interval, rises as frequency increases, thus giving rise to a dramatic life reduction of insulation systems.

Material #C exhibits the best performance among the materials evaluated during life tests, both at low and at high frequency, because it belongs to the family of corona resistant materials, but, particularly, since it is affected by PD having amplitude which is the lowest among the tested materials.

On the contrary, #D, also corona resistant, does not show significant life improvement with respect to #A, and this may be due to the high PD magnitude, as shown previously. Finally, material #A, which is not corona resistant, can be affected largely from PD, which have the largest amplitude, and thus the worst life behaviour. Moreover, the fact that #A has conventional insulation (i.e. not reinforced by fillers) will increase degradation rate due to PD activity with respect to corona resistant materials.

Concluding, a very rough model is proposed to evaluate numerically the extent of life reduction of an insulating system subjected to a PWM waveform with spikes and/or ringings superimposed, as that reported in Fig. 2.1 of chapter 2.

Let us consider that the resultant ageing rate, $1/L$, could be obtained through superposition of effects [66]. Ageing rates relevant to high-amplitude pulses $1/L_P$ and that relevant to service ordinary stress $1/L_0$ can be composed as [108]:

$$\frac{1}{L} = \frac{1}{L_0} + \frac{1}{L_P} \tag{7.18}$$

so that

$$L = \frac{L_0}{1 + \frac{L_0}{L_P}} \tag{7.19}$$

If we assume that (according to inverse power model [66]):

$$L_P = L_T \left(\frac{V_P}{V_T} \right)^{-n_{PD}} \frac{T/2}{\tau} \tag{7.20}$$

L_T is the life at a voltage = PD inception voltage V_T, with bipolar squarewave;

n_{PD} = voltage endurance coefficient relevant to tests with bipolar squarewave in the presence of PD;L

V_P = voltage spike amplitude;

τ = voltage spike width;

$T/2$ = half-period of the PWM carrying

Substituting eq. (7.20) in (7.19) it is possible to obtain the following equation:

$$L = \frac{L_0}{1 + \frac{L_0}{L_T} \frac{\tau}{T/2} \left(\frac{V_P}{V_T} \right)^{n_{PD}}} \tag{7.21}$$

As an example, the life of a standard insulation system (built with material #A) supplied by a 400 V (rms) inverter with a switching (carrying) frequency of 10 kHz, i.e. $T/2$ = 50 μs, can be evaluated in the case that spikes, about 1μs wide, have an amplitude of two times the voltage amplitude available from inverter. Life in the absence of spikes can be easily derived from life models reported in chapter 5 (e.g. from Fig. 5.20), providing $L_0 \approx 1 \cdot 10^9$ h. Life at PDIV and VEC relevant to life line in the presence of PD can be obtained from Fig. 5.20, i.e. $L_T \approx 10$ h and $n_{PD} = 4.5$. From eq. 7.21 we obtain, finally, a life estimate of about 160 h. These results, which must be experimentally verified, can constitute a quantitatively rough evaluation of the dramatic effect that voltage spikes, due to high-frequency-pulsed supply, produce on ageing acceleration.

7.6 Conclusions

Partial discharge activity is the main factor which promote insulation degradation. It is regulated by peak-to-peak voltage and increases with supply frequency.

Organic materials, as #A, are dramatically affected by partial discharges, so that their reliability could be significantly reduced, especially at high frequencies. Corona resistant materials, built to withstand better PD activity show a different behaviour: some display an improved performance (e.g. #B and #C) others worse (#D).

The experimental tests here discussed try to single out the material phenomena which mainly affect insulation reliability, in order to provide some parameters useful to design new materials more resistant to stresses caused by power converters. Among these, PD amplitude and PDIV have prevailing importance. They seems to be significantly influenced by space charge trapping features of insulating materials. Corona resistant materials with increased conductivity or smaller trap depth (increased mobility) can present smaller partial discharges and, thus, longer life, as seen for #C.

Conductivity or space charge measurements can, thus, provide in short times fundamental information about the extent of PD that will affect the material, helping in the choice of the most appropriate insulation for power electronic applications.

Appendix

Referring to §7.3.1 the derivation of eq. (7.5) from eq. (7.2) is explained in the following.

$$E_1^* l_1 + E_2^* l_2 + E_0^* l_0 = V \tag{A.1}$$

From expression (7.2) and (7.3):

$$E_1^* = E_2^* - \frac{\rho\xi}{\varepsilon_1} \tag{A.2}$$

$$E_2^* = \frac{\varepsilon_0}{\varepsilon_1}(E_0^* - \frac{\sigma_S}{\varepsilon_0}) \tag{A.3}$$

E_1^* can be expressed as a function of E_0^*, that is:

$$E_1^* = \frac{\varepsilon_0}{\varepsilon_1}(E_0^* - \frac{\sigma_S}{\varepsilon_0}) - \frac{\rho\xi}{\varepsilon_1} \tag{A.4}$$

Substituting (A.2) and (A.4) in eq. (A.1), we obtain:

$$\left(\frac{\varepsilon_0}{\varepsilon_1}(E_0^* - \frac{\sigma_S}{\varepsilon_0}) - \frac{\rho\xi}{\varepsilon_1}\right) l_1 + \frac{\varepsilon_0}{\varepsilon_1}\left(E_0^* - \frac{\sigma_S}{\varepsilon_0}\right) l_2 + E_0^* l_0 = V \tag{A.5}$$

$$\frac{\varepsilon_0}{\varepsilon_1} E_0^* l_1 - \frac{\sigma_S}{\varepsilon_1} l_1 - \frac{\rho\xi}{\varepsilon_1} l_1 + \frac{\varepsilon_0}{\varepsilon_1} E_0^* l_2 - \frac{\sigma_S}{\varepsilon 1} l_2 + E_0^* l_0 = V$$

Collecting common factors, we come to:

$$E_0^* = \frac{V}{\frac{\varepsilon_0}{\varepsilon_1} l_1 + \frac{\varepsilon_0}{\varepsilon_1} l_2 + l_0} + \frac{\frac{\sigma_S}{\varepsilon_1} l_1 + \frac{\sigma_S}{\varepsilon_1} l_2 + \frac{\rho\xi}{\varepsilon_1} l_1}{\frac{\varepsilon_0}{\varepsilon_1} l_1 + \frac{\varepsilon_0}{\varepsilon_1} l_2 + l_0} \tag{A.6}$$

Since $d \cong l_1 + l_2$ (if $\xi << l_1$ and $\xi << l_2$):

$$E_0^* = \frac{V}{\frac{\varepsilon_0}{\varepsilon_1} d + l_0} + \frac{\frac{\sigma_S}{\varepsilon_1} d + \frac{\rho\xi}{\varepsilon_1} l_1}{\frac{\varepsilon_0}{\varepsilon_1} d + l_0} \tag{A.7}$$

The electric field in the absence of space charge E_0 has the expression reported in (7.1), that is:

$$E_0 = \frac{V}{\frac{\varepsilon_0}{\varepsilon_1} d + l_0} \tag{A.8}$$

and, finally we arrive at expression (7.5), that is:

$$E_0^* = E_0 + \frac{\rho\xi l_1 + \sigma_S d}{\varepsilon_0 d + \varepsilon_1 l_0} \tag{A.8}$$

References

[1] IEEE 519, *Recommended Practices and Requirements for Harmonic Control in Electric Power Systems*, December 1992.

[2] IEC 1000-3-2, *Electromagnetic compatibility (EMC) – Part 3: Limits – Section 2: Limits for Harmonic Current Emission*, First Edition, March 1995.

[3] IEC 61 642, *Industrial AC Networks Affected by Harmonics - Application of Filters and Shunt Capacitors*, 1997.

[4] IEEE Task Forces, "The Effect of Power System Harmonics on Power System Equipment and Loads", IEEE Trans. on Power App. Sist., Vol. 104, n. 9, pp. 2555-2563, September 1985.

[5] IEEE Task Force on the Effects of Harmonics on Equipments, "Effects of Harmonics on Equipment", IEEE Trans. on Power Del., Vol. 8, n. 2, pp. 672-680, April 1993.

[6] A. Cavallini, M. Loggini and G. C. Montanari, "Comparison of Approximate Methods for Estimate Harmonic Currents Injected by AC/DC Converters", IEEE Trans. on Ind. Electronics, Vol. 41, n. 2, pp. 256-262, April 1994.

[7] A. Mansoor, W. M. Grady, R. S. Thallam, M. T. Doyle, S. D. Krein and M. J. Samotyj, "Effect of Supply Voltage Harmonics on the Input Current of Single-phase Diode Bridge Rectifier Loads", IEEE Trans. on Power Del., Vol. 10, n. 3, pp. 1416-1422, July 1995.

[8] E. W. Kimbark, *Direct Current Transmission*, Wiley, New York, NY (USA),1971.

[9] T. S. Key and J.-S. Lai, "Costs and Benefits of Harmonic Current Reduction for Switch-mode Power Supplies in a Commercial Office Building", IEEE Trans. on Ind. Appl., Vol. 32, n. 5, pp. 1017-1024, October 1996.

[10] E. F. Fuchs, D. J. Roesler and K. P. Kovacs, "Aging of Electrical Appliances due to Harmonics of the Power System's Voltage", IEEE Trans. on Power Del., Vol. 1, n. 3, pp. 301-307, July 1986.

[11] G. Carpinelli, P. Caramia, E. Di Vito, A. Losi and P. Verde, "Probabilistic Evaluation of the Economical Damage due to Harmonic Losses in Industrial Energy System", IEEE Trans. on Power Del., pp. 1021-1031, April 1996.

[12] P. Caramia, G. Carpinelli, P. Verde, G. Mazzanti, A. Cavallini, G. C. Montanari, "An Approach to Life Estimation of Electrical Plant Components in the Presence of Harmonic Distortion", IEEE ICHQP, Orlando, FL (USA), October 2000, pp. 254-256.

[13] D. Fabiani, I. Ghinello, G. Mazzanti, G. C. Montanari and A. Cavallini, "An Investigation of the Endurance of Capacitors Supplied by Nonsinusoidal Voltage", IEEE CEIDP, Atlanta, GA (USA), October 1998, pp. 723-727.

[14] D. Fabiani, I. Ghinello and G. C. Montanari, "Accelerated Degradation of Capacitor PP Films under Voltage Distortion", IEEE CEIDP, Atlanta, GA (USA), October 1998, pp. 686-689.

[15] A. Cavallini, I. Ghinello, G. Mazzanti and G. C. Montanari, "Considerations on the Life Performances and Installation Practice of Shunt Capacitors in the Presence of Harmonics Generated by AC/DC Converters", IEEE Trans. on Power Del., Vol. 14, n. 1, pp. 227-234, January 1999.

[16] G. C. Montanari and D. Fabiani, "Searching for the Factors which Affect Self-healing Capacitor Degradation under Non-sinusoidal Voltage", IEEE Trans. on Dielectrics Electr. Insul., Vol. 6, n. 3, pp. 319-325, June 1999.

[17] G. C. Montanari and D. Fabiani, "The Effect of Non-sinusoidal Voltage on Intrinsic Aging of Cable and Capacitor Insulating Materials", IEEE Trans. on Dielectrics Electr. Insul., Vol. 6, n. 6, pp. 798-802, December 1999.

[18] A. Cavallini, D. Fabiani, G. Mazzanti, G. C. Montanari and A. Contin "Voltage Endurance of Electrical Components Supplied by Distorted Voltage Waveforms", IEEE ISEI, pp.73-76, Anaheim, CA (USA), April 2000.

[19] A. Cavallini, D. Fabiani, G. Mazzanti, and G. C. Montanari "Models for Degradation of Self-healing Capacitors Operating under Voltage Distortion and Temperature", IEEE ICPADM, Xian, China, June 2000, pp. 108-111.

[20] A. Cavallini, D. Fabiani, G. Mazzanti and G. C. Montanari "The Effect of Power System Harmonics on Cable Endurance: a Critical Review to IEEE Std. 519 Voltage Distortion Limits", IEEE IAS 35th Annual Meeting, Rome, Italy, October 2000, pp.3172-3179.

[21] D. Fabiani and G. C. Montanari, "The Effect of Voltage Distortion on Aging Acceleration of Insulation Systems under Partial Discharge Activity", IEEE Electr. Insul. Mag., Vol. 17, n. 3, pp. 24-33, May 2001.

[22] D. Fabiani, G. C. Montanari and A. Contin, "Aging Acceleration of Insulating Materials for Electrical Machine Windings Supplied by PWM in the Presence and in the Absence of Partial Discharges" IEEE ICSD, Eindhoven, The Netherlands, June 2001, pp. 283-286.

[23] J. A. Oliver and G. C. Stone, "Implications for the Application of Adjustable Speed Drive Electronics to Motor Stator Winding Insulation", IEEE Electr. Insul. Mag., Vol. 11, n. 4, pp. 32-36, July 1995.

[24] C. Newton and M. Sumner, "Multi-Level Converters: a Real Solution to Medium/High Voltage Drives?, IEE Power Engineering Journal, pp. 21-26, February 1998.

[25] R. J. Kerkman, D. Leggate and G. L. Skibinski, "Interaction of Drive Modulation and Cable Parameters on AC Motor Transients" IEEE Trans. on Ind. Appl., Vol. 33, n. 2, pp. 722-731, June 1997.

[26] M. Melfi, A. M. J. Sung, S. Bell, and G. L. Skibinski, "Effect of Surge Voltage Risetime on the Insulation of Low-voltage Machines Fed by PWM Converters" IEEE Trans. on Ind. Appl., Vol. 34, n. 4, pp. 766-775, August 1998.

[27] E. Persson, "Transient Effects in Application of PWM Inverters to Induction Motors", IEEE Trans. on Ind. Appl., Vol. 28, n. 5, pp.1095-1101, September 1992.

[28] S. B. Warder, F. Friedlander and A. N. Arman, "The Influence of Rectifier Harmonics in a System on the Dielectric Stability of 33-kV Cables", CIGRE, paper no.1025, 1950

[29] Specification for electric motor insulation, NEMA Motor and Generator Standards, MG-1, Part 30, 1991

[30] Specification for definite purpose inverter fed motors, NEMA Motor and Generator Standards, MG-1, Part 31, Rev. 3, 1993

[31] L. Manz, "Motor Insulation System Quality for IGBT Drives", IEEE Ind. Appl. Mag., pp. 51-55, February 1997.

[32] J. P. Bellomo, T. Lebey, J. M. Oraison and F. Peltier, "Characterization of Voltage Shapes Acting on the Insulation of Rotating Machines Supplied by Inverters", IEEE ICPADM, Brisbane, Australia, July 1994, pp.792-795.

[33] J. P. Bellomo, *Etude des Consequences des Nouvelles Formes de Commande sur les Materiaux de l'Isolation Statorique*, Ph.D Thesis, Universitè Paul Sabatier, Toulouse, France, 1996.

[34] W. Yin, "Failure Mechanism of Winding Insulation in Inverter-Fed Motors", IEEE Electr. Insul. Mag., Vol. 13, n. 6, pp.18-23, November 1997.

[35] G. C. Stone, R. G. van Heeswijk and R. Bartnikas, "Investigation of the Effect of Repetitive Voltage Surges on Epoxy Insulation", IEEE Trans. on Energy Conv., Vol. 7, n. 4, pp. 754-759, December 1992.

[36] N. Foulon, J. P. Lucas, G. Barré, R. Mailfert and J. Enon, "Investigation of the Failure Mechanism of Insulation Subjected to Repetitive Fast Voltage Surges", IEEE EIC and EMCW, Rosemont, IL (USA), September 1997, pp. 401-406.

[37] G. C. Montanari, D. Fabiani and A. Contin, "Aging Investigation of Turn Insulation under Fast Repetitive Pulse Voltage with or without Partial Discharges", CWIEME'99, Berlin, Germany, June 1999, pp. 88-96.

[38] D. Fabiani and G. C. Montanari, "On the Degradation of Winding Insulation of Ac-motors Supplied by Adjustable Speed Drives – an Overview", ELECTROMOTION, Vol. 8, n. 2, pp. 89-95, June 2001.

[39] K. Bauer, M. Kaufhold and H. Wang, "High Voltage Motor Winding Insulation for High Power Adjustable Speed Drives Fed by IGBT-Converter", 8th BEAMA '98, pp.257-263, Harrogate, UK, May 1998.

[40] R. Busch, private communication, March 2000.

[41] G. Grandi, D. Casadei, U. Reggiani, "Equivalent Circuit of Mush Wound AC Windings for High Frequency Analysis", IEEE ISIE, Guimarães, Portugal, July 1997, pp. 201-206.

[42] V. Divljankovic, J. Kline, J. Akers and K. Theis, "Multifactor Aging of Electrical Machines Energized by Standard PWM Drives", IEEE CEIDP, San Francisco, CA (USA), October 1996, pp. 808-812.

[43] M. Kaufhold, G. Borner, M. Eberhardt and J. Speck, "Failure Mechanism of Low Voltage Electric Machines Fed by Pulse-Controlled Inverters", IEEE Electr. Insul. Mag., Vol. 12, n. 5, pp.9-15, September 1996.

[44] L. Centurioni, G. Coletti and F. Guastavino, "A Study about the Influence of the Rise Time of Quasi-Square Voltages on the Aging by Partial Discharges of a Polymeric Film", IEEE ISEI, Anaheim, CA (USA), April 2000, pp. 21-23.

[45] M. Kaufhold, "Failure Mechanisms of the Interturn Insulation of Low Voltage Electric Machines Fed by Pulse Controlled Inverters", IEEE CEIDP, Virginia Beach, Virginia (USA), October 1995, pp. 254-257.

[46] T. Lebey, P. Castelan, G. C. Montanari and I. Ghinello, "Influence of PWM Type Voltage Waveforms on Reliability of Machine Insulation Systems", IEEE ICHQP Athens, Greece, September 1998, pp. 994-998

[47] J. P. Bellomo, T. Lebey, J. M. Oraison and F. Peltier, "Influence of Rise Time on the Dielectric Behavior of Stator Insulation Materials", IEEE CEIDP, San Francisco, CA (USA), October 1996, pp. 842-845.

[48] W. Yin, "Dielectric Properties of an Improved Magnet Wire for Inverter-fed Motors", IEEE Electr. Insul. Mag., Vol. 13, n. 4, pp. 17-23, August 1997.

[49] D. Fabiani, G. C. Montanari and A. Contin, "The Effect of Fast Repetitive Pulses on the Degradation of Turn Insulation of Induction Motors", IEEE SDEMPED, Grado (GO), Italy, September 2001, pp. 413-418.

[50] A. Mbaye, F. Grigorescu, T. Lebey and Bui Ai, "Existence of Partial Discharges in Low-Voltage Induction Machines Supplied by PWM Drives", IEEE Trans on Dielectrics and Electr. Insul., Vol. 3, n. 4, pp. 554-560, August 1996.

[51] M. Fenger, S. R. Campbell and G. Gao, "The Impact of Surge Voltage Rise-Time on PD Inception Voltage in Random Wound Motors of Different Designs", IEEE CEIDP, Kitchener, Canada, October 2001, pp. 352-355.

[52] W. Pfeiffer and M. Paede, "About the Influence of the Frequency on the Partial Discharge Characteristics of Enamelled Wires", IEEE EIC and EMCW, Cincinnati, OH (USA), October 1999, pp. 485-488.

[53] G. C. Stone, S. Campbell and S. Tetreault, "Inverter-Fed Drives: Which Motor Stators are at Risk?", IEEE Ind. Appl. Magazine, Vol. 6, n. 5, pp. 17-22, October 2000.

[54] C. Hudon, N. Amyot and D. Jean, "Long Term Behavior of Corona Resistant Insulation Compared to Standard Insulation of Magnet Wire", IEEE ISEI, Anaheim, CA (USA), April 2000, pp. 13-16.

[55] A. H. Bonnett and G.C. Soukup, "Cause and Analysis of Stator Rotor Failures in Three-Phase Squirrel-Cage Induction Motors", IEEE Trans. on Ind. Appl., Vol. 28, n. 4, pp. 921-937, July 1992.

[56] W. Yin, K. Bultemeier, D. Barta and D. Floryan, "Critical Factors for Early Failure of magnet Wires in Inverted-Fed Motors", IEEE CEIDP, Virginia Beach, VA (USA), October 1995, pp.258-261.

[57] G. Gao, M. Steinhauser and R. Kavanaugh, "Studies on the Insulation Life of ASD-Fed motors under Accelerated Aging Conditions", IEEE CEIDP, Austin, TX (USA), October 1999, pp. 581-584.

[58] J. P. Bellomo, P. Castelan and T. Lebey, "The Effect of Pulsed Voltages on Dielectric Material Properties", IEEE Trans on Dielectrics and Electr. Insul., Vol. 6, n. 1, pp. 20-26, February 1999.

[59] IEC Std. 62068: *Evaluation of Electrical Stresses Produced by Repetitive Impulses. Part 1: General Methods of Evaluation of Electrical Endurance* (IEC 98-160 CDV*). Part 2: State of the Art Report* (62068-2 (2001-08)).

[60] J. P. Bellomo, H. Olivier and T. Lebey, "Lifetime Determination of Polyamide under Square Voltage", IEEE EIC/EMCW, Chicago, IL (USA) September 1997, pp. 419-423.

[61] J. P. Bellomo, A. Mbaye and T. Lebey, "Ageing Properties of Polyimide and Polyester Films: Experimental Results and Discussion", IEEE ISEI, Arlington, VA (USA), June 1998, pp. 177-180.

[62] S. Grzybowsky, E. A. Feilat and P. Knight, "Accelerated Aging Tests on Magnet Wires under High Frequency Pulsating Voltage and High Temperature", IEEE CEIDP, Austin, Texas (USA), October 1999, pp. 555-558.

[63] ASTM Std. D1676, *Standard Methods for Testing Film-Insulated Magnet Wire*, Annual Book of ASTM Standards, Vol. 01.03, 1983.

[64] ANSI/IEEE Std. 930-1987, *IEEE Guide for the Statistical Analysis of Electrical Insulation Voltage Endurance Data.*

[65] W. Nelson, *Applied Life Data Analysis*, Wiley, 1982, ISBN 0-471-09458-7.

[66] L. Simoni, *Fundamentals of Endurance of Electrical Insulating Materials*, CLUEB, Bologna, Italy, 1983.

[67] T. Takada and T. Sakai, "Measurement of Electric Field at a Dielectric/Electrode Interface using an Acoustic Transducer Technique", IEEE Trans. on Electr. Insul., Vol. 18, n. 5, pp. 619-628, October 1983.

[68] T. Maeno, T. Futami, K. Kushibe, T. Takada and C. M. Cooke, "Measurement of Spatial Charge Distribution in Thick Dielectric using the Pulsed Electroacoustic Method", IEEE Trans. on Electr. Insul., Vol. 23, n. 3, pp. 433-439, June 1988.

[69] J. M. Alison, "A high Field Pulsed Electro-Acoustic Apparatus for Space Charge and External Circuit Current Measurement within Solid Insulators", Meas. Sci. Technol., Vol. 9, pp. 1737-1750, 1998.

[70] G. C. Montanari, G. Mazzanti, L. A. Dissado and D. K. Das Gupta, "Space Charges as a Trigger for Electrical Ageing of Polymeric Insulation", in Charges in Solid Dielectrics, The Dielectrics Society, UK, 1998, pp. 259-272.

[71] P. Notingher, A. Toureille, J. Santana, L. Martinotto and M. Albertini, "Study of Space Charge Accumulation in Polyolefins Submitted to Ac Stress", IEEE Trans. on Dielectrics and Electr. Insul., Vol. 8, n. 6 pp. 972-984, December 2001.

[72] M. Abou-Dakka, S. Bamji and A. Bulinski, "Space Charge Distribution Measurements in XLPE and EPR", IEEE CEIDP, Minneapolis, MN, October 1997, pp. 23-27.

[73] T. Maeno and K. Fukunaga, "High-Resolution PEA Charge Distribution Measurement System", IEEE Trans. on Dielectrics and Electr. Insul., Vol. 3, n. 6, pp. 754-757, December 1996.

[74] N. Hozumi, "Space Charge Behavior in Electrical Insulation under High Fields", Int. Symposium on Electrets, Shanghai, September 1996, pp. 3-8.

[75] D. K Das Gupta and G. C Montanari "Polarization and Space Charge Behavior of Unaged and Electrically Aged Crosslinked Polyethylene" IEEE Trans. on Dielectrics and Electr. Insul., Vol. 7, n. 4 pp. 474-479, August 2000.

[76] T. Tanaka, T. Ito, Y. Tanaka and T. Takada, "Frequency Dependence of Interfacial Space Charge Formed in Laminated Dielectrics under AC Voltage Application Conditions", IEEE CEIDP, Victoria, Canada, October 2000, pp. 796-799.

[77] C. Laurent, G. Tardieu, G. Teyssedre, G. C. Montanari and L. Raffaelli, "Combined Space Charge and Electroluminescence Detection in Polyethylene under AC Stress", IEEE CEIDP, Kitchener, Canada, October 2001, pp. 32-35.

[78] D. Muto, S. Kondo, K. Kaneko, Y. Suzuoki, T. Mizutani and T. Itaya, "Space-Charge Characteristics of Modified High-Density Polyethylene for DC Cables", IEEE ISEIM, Toyohashi, Japan, September 1998, pp. 545-548.

[79] G. C. Montanari, G. Mazzanti, F. Palmieri, A. Motori, G. Perego and S. Serra, "Space Charge Trapping and Conduction in LDPE, HDPE and XLPE", Journal of Phys. D: Appl. Physics, Vol. 34, pp. 2902-2911, October 2001.

[80] L. A. Dissado, G. Mazzanti and G. C. Montanari, "The Role of Trapped Space Charges in the Electrical Aging of Insulating Materials", IEEE Trans. on Dielectrics and Electr. Insul., Vol. 4, n. 5, pp. 496-506, August 1997.

[81] T. Takada, "Acoustic and Optical Methods for Measuring Electric Charge Distribution in Dielectrics", IEEE Trans. on Dielectrics and Electr. Insul., Vol. 6, N. 5, pp. 519-547, October 1999.

[82] Y. Zhang, J. Lewiner, C. Alquié and N. Hampton, "Evidence of Strong Correlation between Space Charge Build Up and Breakdown in Cable Insulation", IEEE Trans. on Dielectrics and Electr. Insul., Vol. 3, n. 6, pp. 778-783, December 1996.

[83] G.C. Montanari and D. Fabiani, "Evaluation of DC Insulation Performance Based on Space-Charge Measurements and Accelerated Life Tests", IEEE Trans. on Dielectrics and Electr. Insul., Vol. 7, n. 3, pp. 322-328, June 2000.

[84] C. Hudon, N. Amyot T. Lebey, P.Castelan and N. Kandev, "Testing of Low-voltage Motor Turn Insulation Intended for Pulse-width Modulated Application", IEEE Trans. on Dielectrics and Electr. Insul., Vol. 7, n. 6, pp.783-789, December 2000.

[85] N. Hozumi, T. Takeda, H. Suzuki and T. Okamoto, "Space Charge Behavior in XLPE Cable Insulation under 0.2-1.2 MV/cm dc Fields", IEEE Trans. on Dielectrics and Electr. Insul., Vol. 5, n. 1, pp. 82-90, February 1998.

[86] D. Fabiani, G. C. Montanari and F. Palmieri, "Space Charge Measurements on Enameled Wires for Electrical Machine Windings", CWIEME'01, Berlin, Germany, June 2001, pp. 110-115.

[87] F. H. Kreuger, *Discharge Detection in High Voltage Equipment*, Ed. Temple Press Books LTD, London, 1964.

[88] D. Allan, W. Ariastina, T. R. Blackburn, P. Boss, A. Contin, E. Gockenbah, E. Lemke, G. C. Montanari, M. Muhr, T. Mizutani, T. Okamoto, B. T. Phung, H. Sedding, D. Udhe and F. J. Wester, "Knowledge based Rules for PD Diagnosis of HV Components in Service", CIGRE TF 15.11/33.03.02.

[89] P. H. F. Morshuis, *Partial Discharge Mechanism*, Ph.D Thesis, Ed. Delft University Press, Delft, The Netherlands, 1993.

[90] IEC Std. 60270, *High Voltage Testing Partial Discharge Measurements*, Third Edition, 1997-06.

[91] L. Niemeyer "A Generalized Approach to Partial Discharge Modeling", IEEE Trans. on Dielectrics and Electr. Insul., Vol. 2, n. 4, pp. 685-697, August 1995.

[92] F. Gutfleish and L. Niemeyer "Measurement and Simulation of PD in Epoxy Voids", IEEE Trans. on Dielectrics and Electr. Insul., Vol. 2, n. 5, pp. 729-743, October 1995.

[93] A. Contin, P. Morshuis, G. C. Montanari, A. Cavallini and F. Puletti, "Theoretical and Experimental Derivation of Partial Discharge Height Distribution Models", IEEE CEIDP, Austin, TX (USA), October 1999, pp. 222-226.

[94] A. Contin, A. Cavallini, G. C. Montanari, G. Pasini and F. Puletti, "Artificial Intelligence Methodology for Separation and Classification of Partial Discharge Signals", IEEE CEIDP, Victoria, Canada, October 2000 pp. 522-526.

[95] A. Contin, G. C. Montanari and C. Ferraro, "Partial Discharge Source Recognition by Weibull Processing of the Pulse Height Distribution", IEEE Trans. on Dielectrics and Electr. Insul., Vol. 7, n. 1, pp. 48-58, Feb.2000.

[96] A. Contin, G. C. Montanari, A. Cavallini, G. Pasini and M. Conti, "An Integrated Diagnostic Tool Based on PD Measurements", IEEE EIC/EMCW, Cincinnati (USA), October 2001, pp. 219-224.

[97] D.C. Montgomery, *Design and Analysis of Experiments*, Wiley, New York, NY (USA),1997.

[98] STATGRAPHICS R.3.0 for Windows 95, Manugistics Inc. 1997.

[99] G.C. Montanari, L. Raffaelli, F. Palmieri, L. Martinotto and S. Serra, "Techniques for the Estimation of Ac Space Charge Accumulation Threshold for Insulating Materials", IEEE CEIDP, Kitchener, Canada, October 2001, pp. 460-464.

[100] R. Busch, F. Pohlmann and K. Muller, "The Influence of Several Environmental Conditions on the Partial Discharge Characteristics and on the Lifetime of Magnet Wires under Inverter Pulse Operation", IEEE ISEIM, Himeji, Japan, November 2001, pp. 645-648.

[101] T. Jing, *Surface Charge Accumulation in SF_6*, Ph.D Thesis, Delft University Press, Delft, The Netherlands, 1993.

[102] M. Takashima, K. Soda and T. Takada, "Measurement of Electric Charges at the Interface between Two Dielectric Layers Using an Electro-Acoustic Transducer Technique", IEEE Trans. on Electr. Insul., Vol. 23, n. 2, pp. 287-295, April 1988.

[103] G. Mazzanti, G. C. Montanari and J. M. Alison, "Evaluation of Trap Depth and Mobility of Polymeric Materials through Space Charge Measurements Performed by the Pulsed Electroacoustic Technique", submitted to IEEE Trans. on Dielectrics and Electr. Insul.

[104] K. Seeger, *Semiconductor physics. An introduction*, Springer-Verlag publ., 7th edition, Berlin, 1999.

[105] P. K. Watson, "The Transport and Trapping of Electrons in Polymers", IEEE Trans. on Dielectrics and Electr. Insul., Vol. 2, n. 5, pp. 915-924, October 1995.

[106] D. A. Seanor, *Electrical properties of polymers*, Academic Press, London, 1982.

[107] M. Meunier, N. Quirke and A. Aslanides, "Characterisation of Charge Carrier Traps in Polymeric Insulators", IEEE CEIDP, Victoria, Canada, October 2000, pp. 21-24.

[108] A. Cavallini, D. Fabiani, G. Mazzanti and G.C. Montanari, "A General Model for Life Estimation of Cables under DC Stress with Voltage-Polarity Inversions Accounting for Space Charge Effects", IEEE ISEIM, Himeji, Japan, November 2001, pp. 449-452.